UNIVERSITÉ DU QUÉBEC À MONTRÉAL

ELECTRODEPOSITION OF LEAD HALIDE PEROVSKITES

THESIS

PRESENTED

AS PARTIAL FULFILLMENT OF

THE DOCTORATE IN CHEMISTRY

BY

TAO LIU

NOVEMBER 2024

UNIVERSITÉ DU QUÉBEC À MONTRÉAL

ÉLECTRODEPOSITION DE PEROVSKITES AUX HALOGENURES DE PLOMB

THÈSE

PRÉSENTÉ

COMME EXIGENCE PARTIELLE

DU DOCTORAT EN CHIMIE

PAR

TAO LIU

NOVEMBRE 2024

UNIVERSITÉ DU QUÉBEC À MONTRÉAL

Service des bibliothèques

Avertissement

ACKNOWLEDGEMENTS

I am sincerely thankful to my supervisor, Prof. Joshua Byers, for accepting me in his group and bringing me into the world of electrochemistry. His support and guidance make sure the success of this thesis, and I am also appreciating his patience, encouragement, and resources throughout my PhD journey. Thank you very much for sharing your knowledge and skills with me.

I am grateful to Prof. Sylvain G. Cloutier, Prof. Mohamed Siaj, and Prof. Guillaume Goubert for being committee members during my PhD defense, thank you very much for their valuable comments and advice about my thesis as well as career development.

I would like to thank all members of our group, Alec Dorval, Samaneh Salek Esfahani, Romaric Charles Beugré, for their assistance. I would also like to thank Nanoqam, especially Gwénaël Chamoulaud and Galyna Shul, for their support. I also thank to the Chemistry Department, especially Jacqueline Hue Tieu and Marie-Claude Giguère, for their help.

I would like to thank all my colleagues at UQAM for their support, and friends in Montreal for the pleasure we enjoyed together through all the highs and lows of my PhD journey. Finally, I would like to express my sincere gratitude to my family for their constant love. I would never make it so far without their support.

DEDICATED

To my beloved family.

TABLE OF CONTENT

LIST OF FIGURES

LIST OF TABLES

ABBREVIATIONS

MA: methylammonium

FA: formamidinium

MAI: methylammonium iodide

MABr: methylammonium bromide

MACl: methylammonium chloride

FAI: formamidinium iodide

FABr: formamidinium bromide

FACl: formamidinium chloride

$MAPbX_3$: methylammonium lead halide

$MAPbI_3$: methylammonium lead iodide

$MAPbBr_3$: methylammonium lead bromide

$MAPbCl_3$: methylammonium lead chloride

$CsPbX_3$: cesium lead halide

$CsPb(XY)_3$: cesium lead mixed-halide perovskites

$FAPbI_3$: formamidinium lead iodide

$FAPbBr_3$: formamidinium lead bromide

$FAPbCl_3$: formamidinium lead chloride

DMSO: dimethyl sulfoxide

H_2O: water

FTO: fluorine-doped tin oxide

ITO: indium tin oxide

OAI: octylammonium iodide

$HCOO^-$: formate

PEAI: phenylethylammonium iodide

DCM: Dichloromethane

BQ: benzoquinone

Fc: ferrocene

$TBAPF_6$: tetrabutylammonium hexafluorophosphate

TBA^+: tetrabutylammonium

LHP: lead halide perovskites

PCE: power conversion efficiency

ETL: electron transfer layer

HTL: hole transport layer

ETM: electron transport materials

HTM: hole transport materials

OER: oxygen evolution reaction

HER: hydrogen evolution reaction

ED: Electrodeposition

CV: cyclic voltammetry

LSV: linear sweep voltammetry

EIS: electrochemical impedance spectroscopy

VB: valence band

CB: conduction band

VBM: valence band maximum

CBM: conduction band minimum

$E_{(CB)}$: conduction band energy level

$E_{(VB)}$: valence band energy level

I_{ph}: photocurrent

XRD: X-ray diffraction

SEM: scanning electron microscopy

PL: photoluminescence

UV: ultraviolet

e^-: electron

h^+: hole

LED: light-emitting diode

E_g: band gap

LIST OF SYMBOLS AND UNITS

eV : electron volt

V: voltage (volt)

A: ampere

μA: microampere

t: time

min: minute

s: second

cm: centimetre

cm^2: square centimetre

m^2: square metre

μm: micrometer

nm: nanometer

pm: picometre

M: molar concentration

mM: millimolar concentration

A: absorbance

a.u.: absorbance unit

°C: degree Celsius

i: current density (A/m^2)

E: potential (volt)

C: concentration

E_c: conduction band energy (eV)

E_v: valence band energy (eV)

Ω: ohm

RÉSUMÉ

L'essor des pérovskites aux halogénures de plomb (LHP) a suscité de nombreux intérêts dans les applications photovoltaïques et optoélectroniques en raison de leurs propriétés importantes, telles que la mobilité élevée des porteurs de charge et la longue longueur de diffusion des porteurs. Le rendement de conversion d'énergie (PCE) des cellules solaires à pérovskites a été grandement améliorée à 25%, ce qui est compétitif par rapport aux records commerciaux du silicium. Un autre avantage des LHP est leur synthèse facile, et diverses techniques peuvent être utilisées pour synthétiser des matériaux pérovskites, notamment le dépôt par centrifugation, le dépôt sous vide/assisté par vapeur, etc. Même si la synthèse des LHP a fait des progrès au cours des 20 dernières années, les inconvénients des techniques ci-dessus limitent encore leur mise à l'échelle pour des applications commerciales. Ici, nous avons développé une méthode générale pour synthétiser les LHP de manière simple et susceptible d'être étendue à faible coût. Tout d'abord, dioxyde de plomb (PbO_2) a été électrodéposé et converti en films d'halogénure de plomb (PbX_2, X = Cl, Br, I) sur un substrat FTO/verre. Deuxièmement, PbX_2 a été plongé dans une solution d'halogénure de méthylammonium (MAX ou CH_3NH_3X) et d'halogénure de césium (CsX) pour être converti en $MAPbX_3$ ($CH_3NH_3PbX_3$) et $CsPbX_3$, respectivement. Pendant ce temps, PbX_2 a également été plongé dans une solution de CsY (Y = Cl, Br, I) pour former une pérovskite inorganique à halogénures mixtes, $CsPb(XY)_3$. La diffraction des rayons X (XRD), la microscopie électronique à balayage (MEB) et la spectroscopie d'absorbance ont utilisées pour confirmer la conversion chimique en deux étapes de PbO_2 en PbX_2 suivie de leur conversion en $MAPbX_3$, $CsPbX_3$ et $CsPb(XY)_3$, respectivement. Il a été constaté que $MAPbBr_3$, $MAPbCl_3$, $CsPbCl_3$ et $CsPb(ICl)_3$ et $CsPb(ClBr)_3$ étaient formés en phase cubique, $MAPbI_3$ en phase tétragonale, $CsPbBr_3$ $CsPbI_3$, $CsPb(IBr)_3$ en phase orthorhombique. Parallèlement, la réponse au photocourant de $MAPbX_3$ et $CsPb(XY)_3$ a été déterminée dans une cellule photoélectrochimique à jonction liquide (PEC), et la stabilité électrochimique de $CsPbX_3$ a également été étudiée et a montré une grande fenêtre de stabilité. En plus de la conversion en deux étapes vers les LHP, une conversion en une étape directement du PbO_2 en $MAPbX_3$ a été réalisée en utilisant les mêmes conditions de conversion, et les films $MAPbX_3$ obtenus avaient une grande taille de grain. Pendant ce temps, le film $MAPbI_3$ a montré un photocourant amélioré par rapport à celui synthétisé par conversion en deux étapes, ce qui a fourni une voie plus efficace vers des pérovskites $MAPbX_3$ de haute qualité.

Ce travail étudie la conversion en deux étapes et en une étape du PbO_2 électrodéposé en $MAPbX_3$ hybride, et présente le premier exemple de transformation chimique du PbO_2 électrodéposé en PbX_2 pour former des pérovskites inorganiques $CsPbX_3$ et $CsPb(XY)_3$ à large bande interdite. Les résultats révèlent leur structure cristalline, leur morphologie de film et leurs propriétés optoélectroniques pour le développement de LHP efficaces et à plus grande échelle.

Mots clés : Électrodéposition, conversion chimique, pérovskites aux halogénures de plomb, pérovskites à halogénures mixtes, cellule photoélectrochimique liquide.

ABSTRACT

The rise of lead halide perovskites (LHPs) has ignited numerous interests in photovoltaic and optoelectronic applications due to their prominent properties, such as high charge carrier mobility and long carrier diffusion length. The power conversion efficiency (PCE) of perovskite solar cells has passed 25%, competitive with silicon commercial records. Another advantage of LHPs is their easy synthesis, and various techniques can be used to synthesize perovskite materials, including spin-coating, vacuum/vapor-assisted deposition, etc. Even though the synthesis of LHPs has made progress in the last 20 years, the drawbacks of the above techniques still limit their scale-up for commercial applications. Herein, we developed a general method to synthesize LHPs in a facile way that can be able to scale up at a low cost. First, lead dioxide (PbO_2) was electrodeposited on an FTO/glass substrate and converted to lead halide (PbX_2, X = Cl, Br, I) films in situ. Second, PbX_2 films were dipped in methylammonium halide (MAX or CH_3NH_3X) and cesium halide (CsX) solutions to convert to $MAPbX_3$ ($CH_3NH_3PbX_3$) and $CsPbX_3$, respectively. Meanwhile, PbX_2 was also dipped in CsY (Y = Cl, Br, I) solution to form inorganic mixed-halide perovskite, $CsPb(XY)_3$. X-ray diffraction (XRD), scanning electron microscopy (SEM) and absorbance spectroscopy were used to confirm the two-step chemical conversion of PbO_2 to PbX_2 then to $MAPbX_3$, $CsPbX_3$ and $CsPb(XY)_3$, respectively. It was found that $MAPBr_3$, $MAPbCl_3$, $CsPbCl_3$, $CsPb(ICl)_3$ and $CsPb(ClBr)_3$ adopted a cubic phase, $MAPbI_3$ in tetragonal phase, $CsPbBr_3$, $CsPbI_3$, and $CsPb(IBr)_3$ in orthorhombic phase. Meanwhile, the photocurrent response of $MAPbI_3$ and $CsPb(XY)_3$ films were determined in a liquid junction photoelectrochemical (PEC) cell, and the electrochemical stability of $CsPbX_3$ was also studied to show a wide stability window. In addition to the two-step conversion toward LHPs, one-step conversion directly from PbO_2 to $MAPbX_3$ in situ was achieved using the same conversion condition, and the obtained $MAPbX_3$ films had a large grain size. Meanwhile, $MAPbI_3$ film showed an improved photocurrent compared with that synthesized by two-step conversion, which provide a more effective route toward high-quality $MAPbX_3$ perovskites.

This work studies the two-step and one-step conversion of electrodeposited PbO_2 to hybrid $MAPbX_3$, as well as presents the first example of the chemical transformation of electrodeposited PbO_2 to PbX_2 to form wide bandgap $CsPbX_3$ and $CsPb(XY)_3$ inorganic perovskites. The results reveal their crystal structure, film morphology and optoelectronic properties for the development of efficient and scaling-up LHPs.

Keywords: Electrodeposition, Chemical conversion, Lead halide perovskites, mixed-halide perovskites, liquid photoelectrochemical cell.

CHAPTER 1

Lead halide perovskites

As a light absorbing semiconductor, lead halide perovskites (LHPs) were first used in a liquid-solid junction solar cell in 2009 with a power conversion efficiency (PCE) of 3.8%, and the efficiency has jumped to 25.2% recently in a solid-state solar cell as shown in Figure 1.1, which is close to that of the champion silicon solar cells (26.7%) [1, 2]. LHPs have outstanding optoelectronic properties, such as high charge carrier mobility, long carrier diffusion length, high photoluminescence quantum yields as well as simple process for the device fabrication, making it one of the most attracting semiconductors in photovoltaics and optoelectronics in the last decade[3, 4].

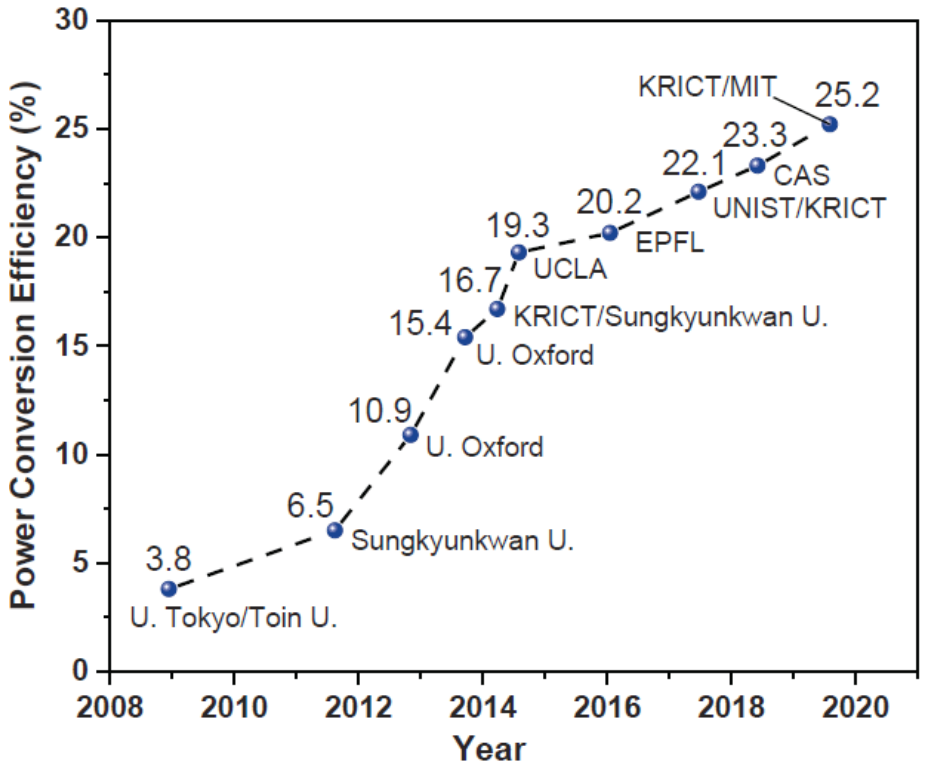

Figure 1.1 The progress of efficiency in perovskite solar cells (adapted from ref. [2]).

1.1 Composition and structure of LHP

LHP structure has a general chemical formula of ABX_3, where A is an organic or inorganic cation such as methylammonium ($CH_3NH_3^+$, MA^+), formamidinium ($CH(NH_2)^+$, FA^+) and cesium (Cs^+), B is a metallic cation such as lead (Pb^{2+}) and tin (Sn^{2+}), X is a halide anion from chloride (Cl^-) to

bromide (Br^-) and iodide (I^-). The ideal 3D crystal structure of LHP consists of $[BX_6]^{4-}$ octahedron and A at the center of the cube formed by eight $[BX_6]^{4-}$ octahedrons, as shown in Figure 1.2. In addition to the 3D structure, LHP also extends to other different dimensions, such as 0D nanoparticles[5], 1D nanowires[6], 2D nanosheets[7], single crystals[8], and thin films[9].

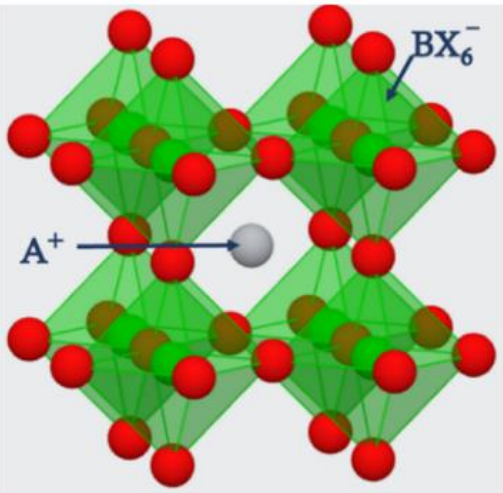

Figure 1.2 3D crystal structure of LHP (adapted from Ref. [10]).

Goldschmidt's tolerance factor and octahedral factor are usually used to predict the stability of a perovskite structure, as shown in equation 1.1 and 1.2.

$$t = \frac{R_A + R_X}{\sqrt{2}(R_B + R_X)} \quad (1.1)$$

$$\mu = \frac{R_B}{R_X} \quad (1.2)$$

where t is Goldschmidt's tolerance factor, μ is octahedral factor, R_A, R_B and R_X are the effective radii of the ions A, B and X, respectively. For LHP, t ranges from 0.81 to 1.11 while μ from 0.44 to 0.90 for a stable perovskite structure, as shown in Figure 1.3[11]. If the size of A (e.g. MA^+ with a radius of 217 pm) is small, it would make t between 0.89 and 1.0 to form a cubic structure, while the less symmetric tetragonal or orthorhombic structure will be formed with t less than 0.89[12]. On the other hand, if the size of A is large (e.g. tetrabutylammonium (TBA^+) with a radius of 494 pm), t would be greater than 1 to form a 1D or 2D structure[13, 14]. Meanwhile, μ with a value between 0.44 and 0.90 determines the stability of the $[BX_6]^{4-}$ octahedron and thus the perovskite structure[15]. The size of B (e.g., Pb^{2+} with a radius of 119 pm) usually does not have a significant effect on t compared with that of A, while the size of X can effectively affect the crystal structure of perovskites. For example, the crystal structure of $MAPbX_3$ changes from tetragonal for $MAPbI_3$ (I^- with a radius of 220 pm) to cubic for $MAPbBr_3$ and $MAPbCl_3$ (Br^-, Cl^-

with a radius of 196 pm, 181 pm, respectively)[8]. Due to the high tunability in composition and structure, LHPs show versatile applications beyond photovoltaics, including LEDs, photodetectors and lasers[16-18].

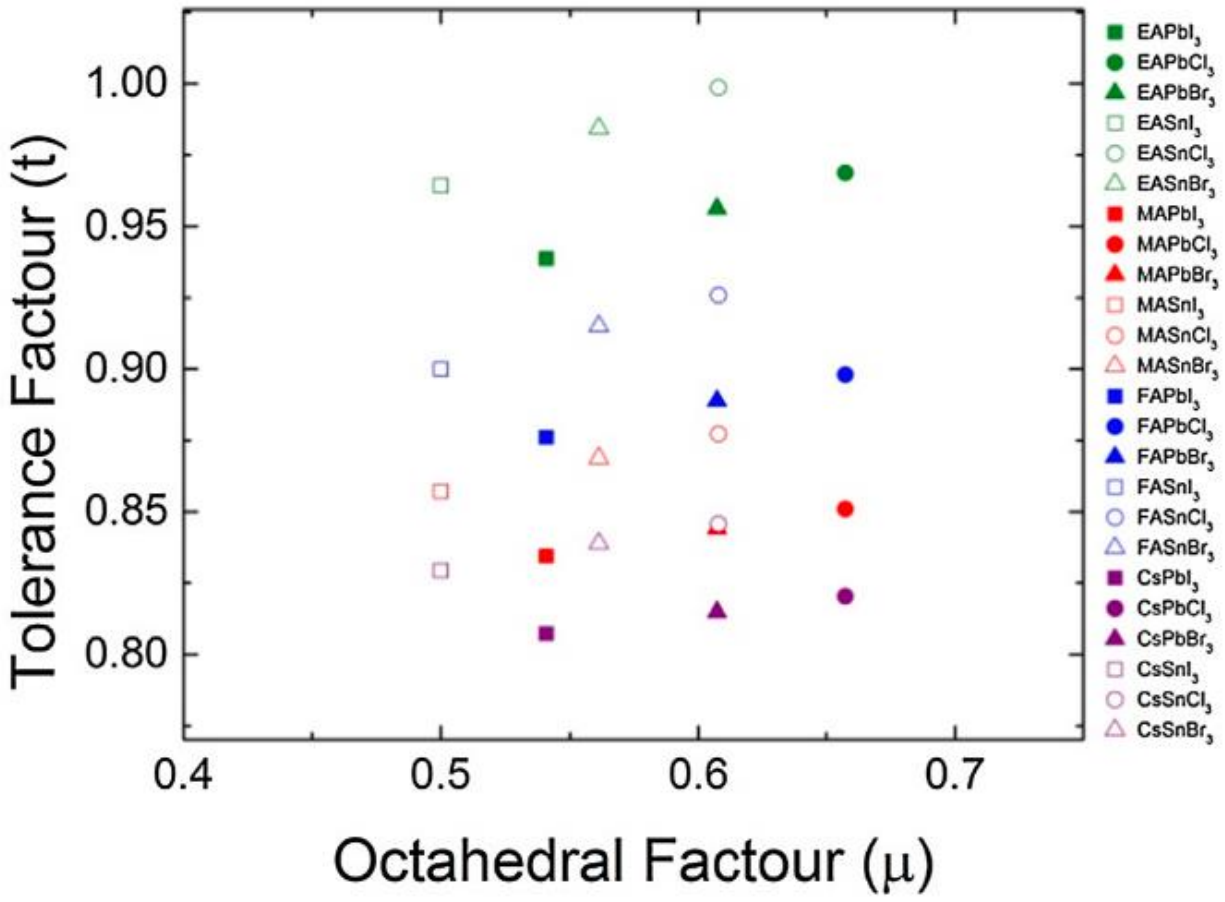

Figure 1.3 Calculated tolerance and octahedral factors for hybrid and inorganic perovskites (adapted from Ref. [11]).

In addition to the ionic radius, temperature is another key factor that affects the perovskite crystal structure. Table 1.1 summarizes the structural transitions of LHPs as a function of temperature. As we can see, LHP crystals adopt a cubic phase at high temperature, which distorts to a tetragonal phase followed by a further change to an orthorhombic phase with decreasing temperature[19-21]. The crystal structure of hybrid perovskites is far more complicated than inorganic perovskite or other conventional semiconductors such as Si, CdTe and GaAs, due to the asymmetric organic cation (MA^+, FA^+) with a permanent dipole located in the corner-shared linkage of the $[BX_6]^{4-}$ octahedron cage. The vibration of this linkage as well as the vibration, orientation and rotation of the organic cation render the structure sensitive to

temperature, showing a lower temperature for structural transition[22]. Unlike hybrid perovskite, metallic cation (Cs^+) doesn't have rotational molecular disorder in the A site, and the structural transition of inorganic perovskite is caused by the flexibility associated with the $[BX_6]^{4-}$ octahedra network[23].

Table 1.1 Structural transition of LHP as a function of temperature

Material	**$MAPbCl_3$**	**$MAPbBr_3$**	**$MAPbI_3$**	**$CsPbCl_3$**	**$CsPbBr_3$**	**$CsPbI_3$**
Crystal system	Cubic	Cubic	Cubic	Cubic	Cubic	Cubic
Transition temperature (K)	177	236	330	320	403	645
Crystal system	Tetragonal	Tetragonal	Tetragonal	Tetragonal	Tetragonal	Tetragonal
Transition temperature (K)	172	149~154	161	315	361	510
Crystal system	Orthorhombic	Orthorhombic	Orthorhombic	Orthorhombic	Orthorhombic	Orthorhombic

1.2 Bandgap energy (E_g) of LHP

LHPs are, in most case, direct-bandgap semiconductors with an E_g spanning across the visible spectrum, and a high photoluminescence quantum yield, e.g. over 90% for surface-modified $MAPbI_3$ thin films. It has been reported that E_g decreases with increasing crystal symmetry for the same ABX_3 composition, namely orthorhombic > tetragonal > cubic. Meanwhile, E_g increases with an increase in the electronegativity of B and X, and there is no obvious trend regarding to the effect of A, as shown in Figure 1.4[24, 25].

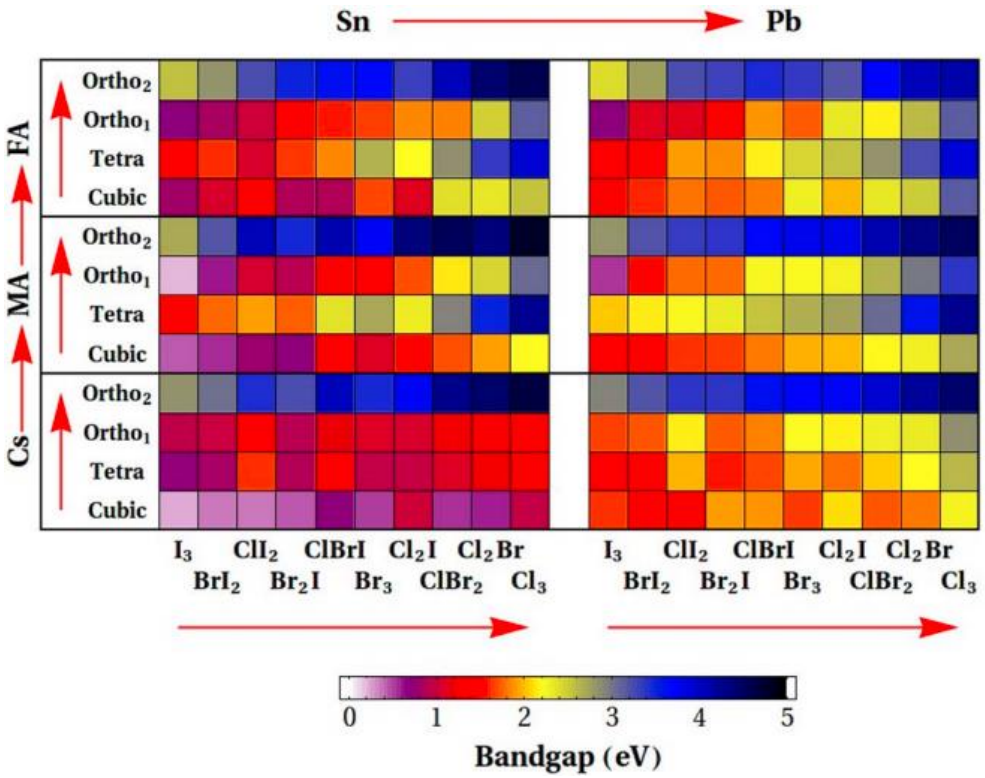

Figure 1.4 The calculated E_g of LHP (adapted from Ref. [25]).

For LHPs, the valence band maximum (VBM) consists of the antibonding combination of B's *s* orbitals and X's *p* orbitals, while the conduction band minimum (CBM) is constituted of B's *p* orbitals plus a residual contribution of X's *s* orbitals[26]. A cation can only indirectly affect the frontier orbitals as its molecular orbitals are far away from the VBM. Substituting MA^+ in cubic $MAPbI_3$ with larger FA^+ results in structural distortions to narrow E_g by ~0.1 eV for $FAPbI_3$, or with smaller Cs^+ to increase E_g by ~0.2 eV for $CsPbI_3$[23, 26]. Substitution of the B site can directly affect the conduction band. For example, the replacement of Pb^{2+} with Sn^{2+} in cubic ABI_3 (A = MA^+) reduces the band gap by ~0.3 eV due to a slight downward shift of the CBM due to the *5p* orbital of Sn compared with the *6p* orbital of Pb. Since the X anion dominates the valence bands position, its substitution can drastically affect VBM. With X going from I to Br to Cl, the valence band composition changes from *5p* to *4p* to *3p*, resulting in an increase in E_g, e.g. 1.5 eV, 2.1 eV, and 2.7 eV for cubic $MAPbI_3$, $MAPbBr_3$, and $MAPbCl_3$, respectively[23, 27].

1.3 Stability and degradation of LHP

Based on the ionic composition, LHPs are generally classified as hybrid and all-inorganic perovskites. In hybrid LHPs, the framework structure leads to an intrinsic softness and dynamic

disorder. The A-site organic cation (MA^+ and FA^+) is larger than the B-site cation and has the ability to rearrange the crystal structure via van der Waals interactions and hydrogen bonding[5, 6, 28]. As a result, the structural symmetry of the perovskite increases compared with its inorganic counterpart. However, due the volatile nature of the organic cation, the weak linkage between the organic cation and the $[PbX_6]^{4-}$ octahedron can induce the decomposition of the perovskite and promote the transition to a non-perovskite structure[29]. Additionally, the relatively weak Pb-X bond forms the perovskite lattice, which can lead structural or compositional changes even due to modest environmental stress. By dissociating the interaction between the organic cation and lead halide framework, moisture and oxygen in air are believed to be the major case of the degradation of hybrid LHPs. Both moisture and oxygen can penetrate through grain boundaries to decompose the entire perovskite crystal in several days under ambient conditions. In addition, heat can also case the self-decomposition of perovskites, and the volatilized organic cation can escape through the grain boundaries. Take the most popular perovskite, $MAPbI_3$ as an example, which can decompose into PbI_2, CH_3NH_2 and other accompanying products following exposure to moisture, oxygen, heat and light, as shown in Figure 1.5[30]. The intrinsic instability of hybrid perovskites is a major challenge during perovskite fabrication and device operation[31, 32]. Although significant stability improvements have been realized through several strategies such as optimization of film morphology, substitution of the A-site with long-chain organic cations, surface modification and encapsulation, thermal stability still remains a major issue for hybrid perovskite due to the highly volatile nature of organic species at elevated temperature, e.g. 85 ^oC for $MAPbI_3$[33]. Thermal stability is critical for perovskite photovoltaics, especially those with intense illumination causing the localized heating of the photoactive film. On the other hand, inorganic perovskites such as $CsPbX_3$ have superior chemical and thermal stability compared to hybrid perovskites due to strong ionic bonding[34]. For example, thermal decomposition of $CsPbI_3$ occurs at a much higher temperature of 450 ^oC[35].

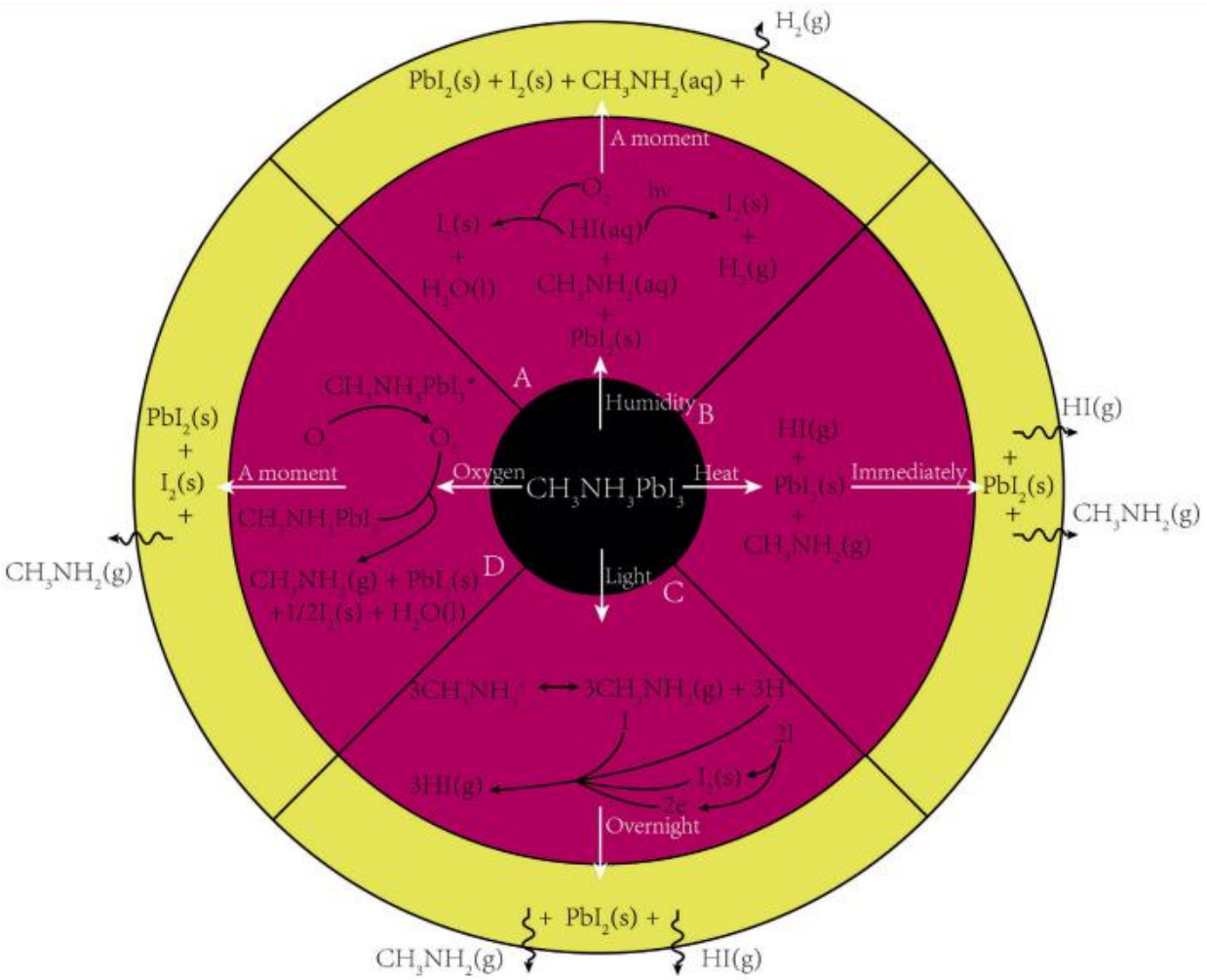

Figure 1.5 The decomposition route of $MAPbI_3$ perovskite (adapted from Ref. [30]).

Compared to the degradation by other environmental stresses, light-induced degradation under solar irradiation is more severe during perovskite device operation[36]. Photodissociation is closely related with heat induced by solar irradiation. The heat causes expansion and distortion of the lattice to promote ion migration away from their original sites. Ions such as I^- in LHP can migrate via structural defects, grain boundaries and interfaces. In addition, heat and light illumination can reduce the ion migration activation energy of the bound ions (e.g., MA^+ and I^-) and drive ion migration. Ion migration can also be driven by the built-in electric field due to the accumulated charges (e.g., electrons in the electron transport layer (ETL) and holes in the hole transport layer (HTL)) in the perovskite device[37]. The result of ion migration leads to compositional segregation and decomposition, which reduces the long-term stability of perovskites[8].

1.4 Preparation of LHPs

LHPs have been found to be defect tolerant as shown in Figure 1.6, which enables perovskite to grow by simple solution and vapor-based processes at low temperature (typically 100 - 150 °C) while achieving high efficiency. This tolerance can be attributed to the presence of Pb^{2+} (or Sn^{2+}), because of 1) the strong spin-orbital coupling of Pb^{2+} leads to a smaller E_g for shallow trap formation, and 2) the hybridization of the *s/p* orbitals of Pb^{2+}'s with the *p* orbital of I forms a conductive electronic structure for shallow traps. In addition, the high dielectric constants of LHPs leads to lower capture cross-sections of charged defects. All of these effects together cause low non-radiative recombination rates despite the presence of high densities of defects during perovskite preparation[38].

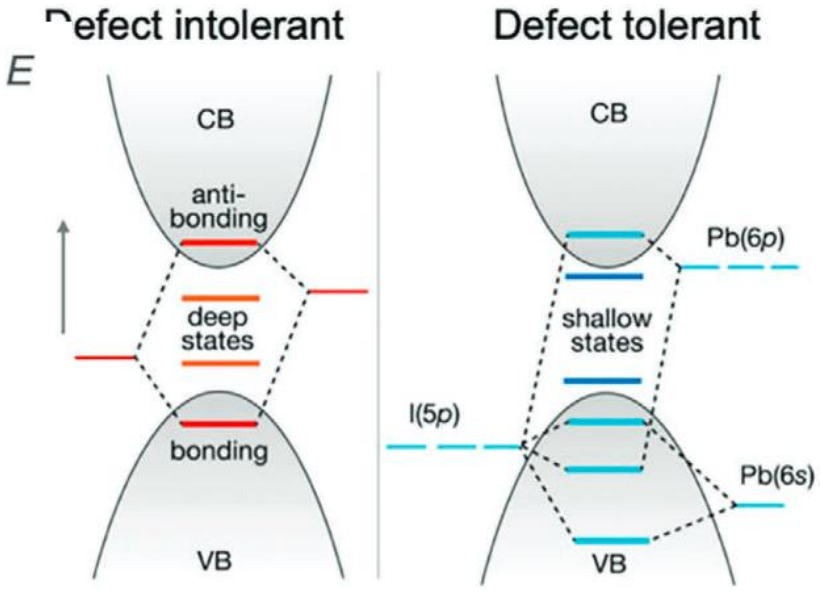

Figure 1.6 Illustration of the electronic structure of defect sensitive (left) and defect tolerant (right) for LHP (adapted from Ref. [38]).

The two main methods for the preparation of perovskite films are solution processing and vapor-assisted processing, as shown in Figure 1.7. Solution processing is categorized into one-step and two-step deposition, which is a relatively facile approach with a low manufacturing cost. However, the film quality obtained from this approach is typically not satisfactory due to the presence of pinholes across the whole film[39]. Vapor-assisted processes include thermal vapor deposition and vapor-assisted solution deposition. Especially the latter technique slows nucleation and enables vigorous reorganization during film growth, leading to a full-coverage of the perovskite film that contains large grain sizes up to microscale[40, 41]. A brief description of

each deposition method will be discussed in the following subsection.

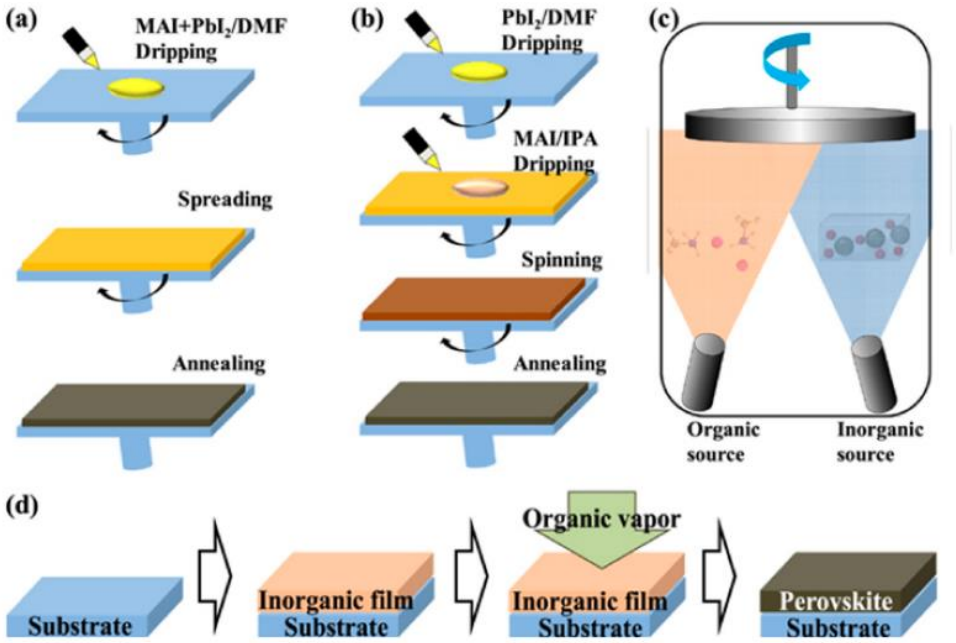

Figure 1.7 Illustration of perovskite film preparation (a) one-step deposition, (b) two-step deposition, (c) thermal vapor deposition and (d) vapor-assisted solution deposition (adapted from Ref. [42]).

1.4.1 One-step deposition

One-step deposition is commonly used to prepare perovskite films because of the facile and cheap nature, which includes the supersaturation of the precursor solution in polar solvents, the formation of nuclei and crystal growth. The one-step method usually uses a mixture of two precursor components such as MAI and PbI_2 as shown in Fig. 1.7a and equation 1.3, followed by thermal annealing (e.g. 100 ^oC for $MAPbI_3$) to passivate defects or eliminate surface impurities. This can also be accompanied with the unexpected creation of disconnected grains that impact the efficiency. To address this issue, Qi et al. found that post-annealing with methylamine greatly reduces impurities and promotes continuity between adjacent grains[43-45]. On the other hand, a rapid evaporation of the solvent can be achieved with the assistance of anti-solvents or vacuum, but the fast nucleation rate results in uncontrolled crystallization or small grain size which reduce the efficiency and stability of the perovskite. Though the one-step deposition serves as a feasible fabrication technique, it is difficult to control film properties such as film morphology and uniformity using this method.

$$MAI + PbI_2 \rightarrow MAPbI_3 \quad (1.3)$$

1.4.2 Two-step deposition

To further control perovskite film morphology, a two-step deposition process was developed. In two-step deposition, PbX_2 solution is deposited via spin-coating, and then the coated substrate is spin-coated with or immersed in another precursor (e.g. MAI) solution followed by an annealing process, as shown in Fig. 1.7b. Though the two-step method can achieve high-quality perovskite film with full coverage and large grain size, the incomplete conversion to perovskite may be an issue because the converted compact perovskite in the top layer hinders the movement of MAI to bottom PbI_2 layer. Several additives like DMSO or H_2O can lead to an amorphous PbI_2 film due to their coordination effect with Pb^{2+} to slow the crystallization of PbI_2, which accelerates the complete conversion of perovskites.

The one-step and two-step deposition processes usually involve spin-coating, which is not suitable for the large-scale preparation of perovskites. Thus, the above-mentioned methods are used for fundamental investigation of perovskites in the laboratory. Other methods such as electrodeposition and ink-jet printing could be useful for large-scale perovskite fabrication[46, 47].

1.4.3 Thermal vapor deposition

Vapor deposition is generally carried out by a vacuum process. For example, MAX and PbX_2 are deposited simultaneously or sequentially through thermal evaporation. Liu et al. used a dual-source simultaneous evaporation system to deposit $MAPbI_3$ film in a nitrogen glove box as shown in Fig. 1.7c, which led to a uniform perovskite film with total coverage of the substrate surface. However, it is difficulty to control the deposition rate using the simultaneous process, and annealing in nitrogen was reported to be a less efficient method to form high quality perovskites than in air[48]. Sequential evaporation of PbI_2 followed by MAI to avoid cross-contamination can lead to a high-quality perovskite film[49].

Compared with solution deposition, perovskite films prepared by thermal vapor deposition show enhanced photocurrent and open circuit voltage due to fewer impurities that can be introduced by solvents. Overall, thermal evaporation enables control over the film thickness and provides better film uniformity.

1.4.4 Vapor-assisted solution deposition

This method deposits PbI_2 from solution to form a PbI_2 film which is then annealed in a chamber

filled with MAI vapor at 150 ^{o}C to form a perovskite, as shown in Fig. 1.7d. The obtained perovskite film showed large grain size, negligible surface roughness and complete conversion to perovskite, along with reduced grain boundaries and traps, which led to an enhanced device performance[50].

Vapor-assisted solution deposition using MAI vapor removes the disadvantages of the two-step solution deposition. It is noted that this method could also serve as a post-treatment process to reduce the trap density and improve the perovskite film quality.

The solution-based methods require less instrumental support, which can produce high quality LHPs in a one- or two-step process. Conversely, the vapor-assisted methods require more instrumental support and critical conditions to deliver higher quality LHPs with fewer impurities originating from the solvents. Newly developed methods such as pulsed laser deposition, inkjet printing, doctor-blade coating, slot-die coating, spray-coating and so forth can be roughly categorized into the above two routes[51]. However, in terms of production cost and large-scale compatibility, solution based sequential deposition is preferable[42].

1.5 Composition engineering and surface passivation

LHPs are generally used in optoelectronic devices, where its crystal quality and stability play a crucial role in device performance. Among these, $MAPbI_3$ with a small E_g of 1.57eV is the most widely investigated perovskite due to its strong light absorption and high efficiency[52]. However, MA-based perovskites are susceptible to degradation under environmental stresses as discussed previously. Its intrinsic thermal instability due to the release of the relatively volatile MA cation during heating is another issue. In order to improve stability and efficiency of perovskites, FA and Cs cations can be used to substitute the MA cation. $FAPbI_3$ was found to have a smaller E_g of 1.48 eV and better heat resistance than $MAPbI_3$. But the cubic structure of $FAPbI_3$ is thermodynamically stable only above 160 °C, and it turns into non perovskite yellow phase at room temperature[53, 54]. Inorganic LHPs like $CsPbI_3$ have a larger E_g of 1.73eV and higher thermal-decomposition temperature, and its photoactive black phase is usually obtained above 300 °C. Similar to $FAbI_3$, $CsPbI_3$ adopts a non-photoactive yellow phase at room temperature.

As discussed above, the structural transitions of LHPs are a key factor affecting their optoelectronic properties. To decrease the transition temperature, solid-state alloying has been widely studied to stabilize the black perovskite phase. The mixed-cation and mixed-halide perovskites have shown dramatic improvements in efficiency as well as stability. Jeong et al reported that the addition of $MAPbBr_3$, MACl and PbI_2 could stabilize the black phase of $FAPbI_3$ with high crystallinity to achieve the highest efficiency record of 25.2% for a perovskite solar cell[55]. Meanwhile, the incorporation of MA and Br ions improved the long-term stability of

$FAPbI_3$, especially the thermal stability. It should be noted that the anion-vacancy defects at $FAPbI_3$ grain boundaries were passivated using the anion formate ($HCOO^-$) to increase film crystallinity[56, 57]. In this case, both composition engineering and surface passivation were able to achieve superior performance in a LHP.

Considering the importance of MABr and MACl to obtain high efficiency perovskites, Simenas et al. investigated the role of $MAPbBr_3$ in the phase transition of $FAPbBr_3$. The transition temperature of the cubic phase of $FAPbBr_3$ decreased with an increase in $MAPbBr_3$ content, which reached the lowest temperature at roughly equivalent amounts of MA^+ and FA^+, as shown in Fig. 1.8 (left)[58]. This indicates the ability of $MAPbBr_3$ to lower the transition temperature of the perovskite phase. Meanwhile, Seok et al. dripped MACl on $CsPbI_3$ followed by a second surface passivation with octylammonium iodide (OAI) to prepare a uniform and pinhole-free $CsPbI_3$ film, and the resulting solar cell gave a high efficiency of 20.4%[59]. It was found that MACl facilitated the removal of solvent to allow a fast crystallization of the $CsPbI_3$ perovskite and enhanced the stability of the film. OAI, on the other hand, improved the moisture resistance of the perovskite as well as the electron-blocking ability for hole extraction from the perovskite[59]. Different from two-step passivation using MACl and OAI, Meng et al. reported one-step defect passivation using in-situ grown low-dimensional phenyltrimethylammonium iodide-based perovskite ($PTAIPbI_3$) located at the $CsPbI_3$ grain boundaries and film surface, to stabilize the black phase of $CsPbI_3$ and prevent moisture intrusion, as shown in Figure 1.8 (right). As a result, the $CsPbI_3$ solar cells showed a high efficiency of 21.0% for the inorganic LHP with high stability[60, 61].

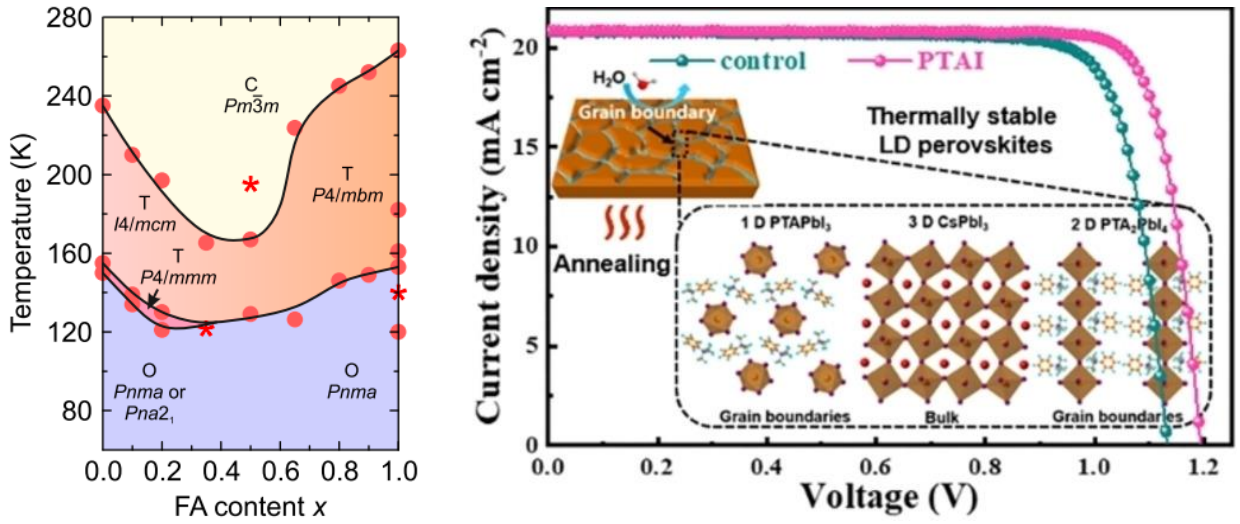

Figure 1.8 (left) Temperature−composition phase diagram of mixed $MA_{1-x}FA_xPbBr_3$ perovskite showing cubic (C), tetragonal (T), and orthorhombic (O) phases. (right) the surface passivation of $CsPbI_3$ grain boundary by low-dimensional $PTAIPbI_3$ perovskite (adapted from Ref. [58-61]).

Another strategy to lower the transition temperature is doping with HI and its derivatives. Snaith and co-workers introduced a small amount of HI into the precursor solution to decrease the transition temperature of black phase of $CsPbI_3$ from 310 ^oC to 100 ^oC as shown in Figure 1.9a, and the resulting $CsPbI_3$ film showed small grains which yielded a PCE of 2.9% in a $CsPbI_3$ solar cell[62]. Since then, HI has served as an additive in perovskite precursor solutions. Wang et al. added HI and phenylethylammonium iodide (PEAI) additives to a precursor solution to stabilize the black phase of $CsPbI_3$ as shown in Figure 1.9b. Here, HI induced the formation of a $HPbI_{3+x}$ intermediate, and PEAI regulated the crystallization and blocked the phase transition through steric effects[63, 64]. Soon after, Wang and co-workers used choline iodide (CHI) to fill the pinholes and cracks in $CsPbI_3$ film as shown in Figure 1.9c. CHI treatment improved the interfacial energy-level alignment to achieve a PCE of 18.4% under ambient conditions[65].

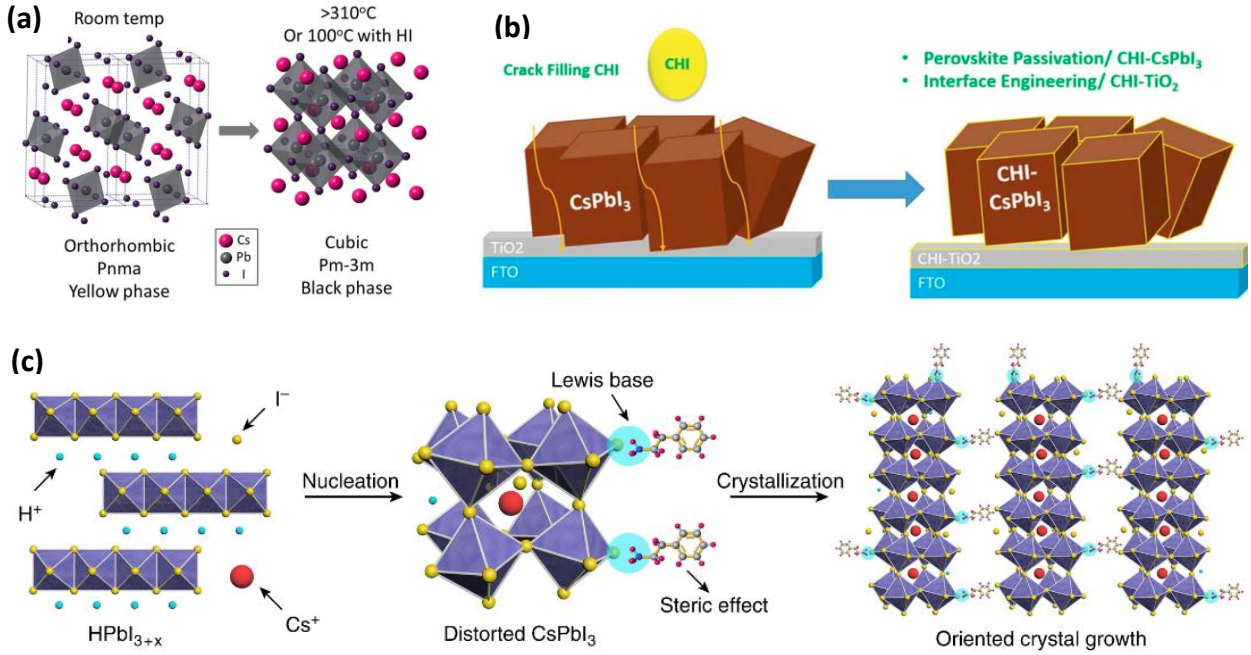

Figure 1.9 (a) diagrammatic structural transition of $CsPbI_3$ phases; (b) Schematic illustration of crack-filling $CsPbI_3$ surface; (c) Schematic for HI/PEAI additive-induced $CsPbI_3$ crystal growth (adapted from Ref. [63-65]).

CHAPTER 2

Electrodeposition of LHP

2.1 Electrodeposition basics

Electrodeposition (ED) refers to a film growth process though a redox reaction driven electrochemically on a conductive substrate. ED is conducted from a precursor solution, which allows a direct control over nucleation and growth of the deposited film. Figure 2.1 shows the setup for conducting an ED in a three-electrode cell. The potentiostat maintains the potential difference between the working and reference electrodes, and the current flows between working and counter electrodes through the external circuit.

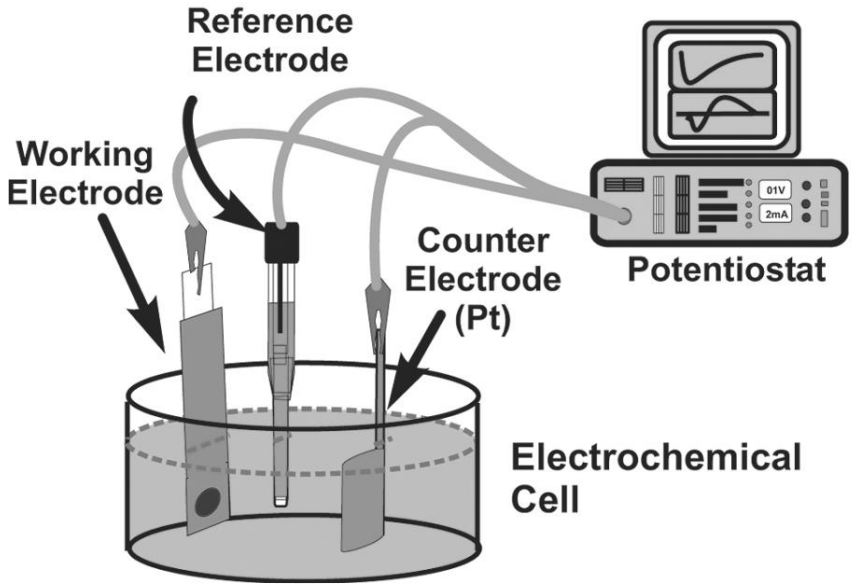

Figure 2.1 Electrochemical cell with three electrodes connected to a potentiostat (adapted from ML Munford, 2006).

ED can be conducted by either voltammetry, chronopotentiometry or chronoamperometry, and the mechanism of ED is generally described as shown in Figure 2.2. First, the solvated ions go through the diffusion layer, transfers electrons with the electrode, adsorbs to form an adatom, and finally incorporates in an energetically favourable site (e.g., surface defect) known as nucleation sites. The nucleation sites allow the formation of nuclei (clusters or islands) which evolve to grains that form deposits that grow on the surface of the electrode.

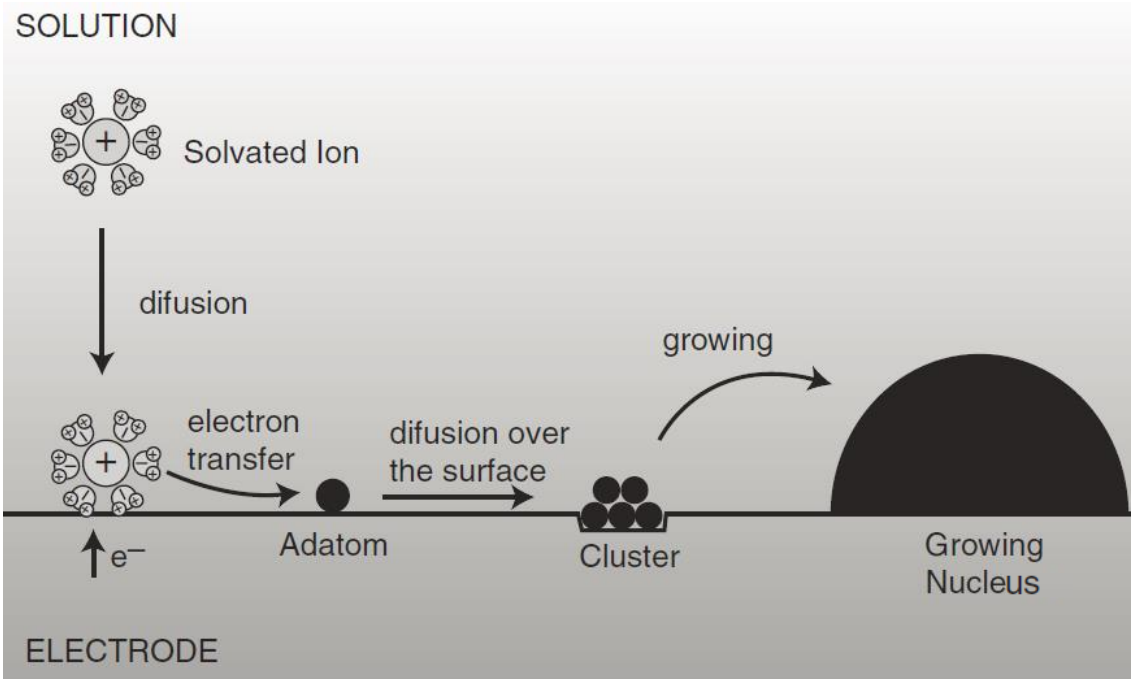

Figure 2.2 Mechanism of electrodeposition on the surface of electrode (adapted from ML Munford, 2006).

ED is a complicated multistep process involving the diffusion and mass transfer of ions in solution, the removal of the solvation sheath, electron transfer, the formation of surface adsorbed atoms, the clustering of adsorbed atoms, the formation of a crystal nucleus or incorporating into an existing lattice. Figure 2.3 shows the voltammogram and chronoamperogram for the electrodeposition of NiOOH on indium tin oxide (ITO). A nucleation loop in the voltammogram indicates the succession of the oxidative electrodeposition of NiOOH and oxygen evolution reaction (OER)， as shown in Figure 2.3a. The loop originates by the increasing electrochemical activity of ITO after NiOOH is deposited, which is reduced to $Ni(OH)_2$ with potential going in the cathodic region. Cyclic voltammetry (CV) identifies the potential window within which ED takes place to conduct chronoamperometry as shown in Figure 2.3b. The chronoamperogram starts with a small current due to the nucleation of NiOOH deposit, then increases as the growth of the deposit until a steady state is reached, as shown in the inset of Figure 2.3b[66, 67].

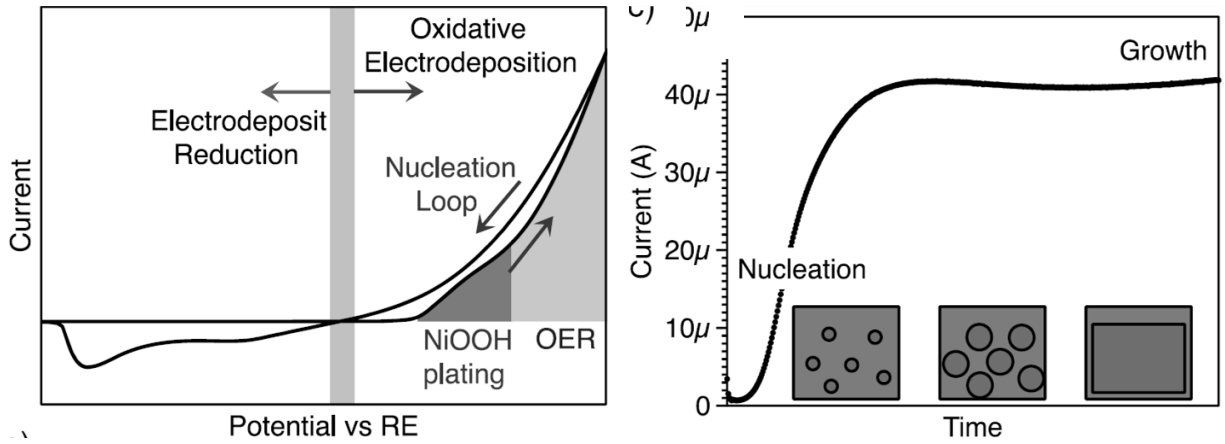

Figure 2.3 (left) Cyclic voltammetry with the nucleation loop at high potential, and (right) current transient recorded during the potentiostatic deposition of NiOOH on ITO (adapted from Ref. [66-67]).

2.2 ED of PbO_2: thermodynamic and kinetics

Like NiOOH, PbO_2 can be electrodeposited using voltammetry and chronoamperometry onto conductive substrates (e.g., FTO, TiO_2) from acidic and basic media where Pb(II) is soluble. In acidic and basic media, the overall electrode reaction can be written as:

$$Pb^{2+} + 2H_2O \rightarrow PbO_2 + 4H^+ + 2e^- \quad (2.1)$$

$$HPbO_2^- + OH^- \rightarrow PbO_2 + H2O + 2e^- \quad (2.2)$$

The equilibrium potential for the PbO_2/Pb(II) couple for equation 2.1 at 298K is given by equation 2.3[68]:

$$E_e = 1.455 - 0.029 \log a_{Pb}^{2+} - 0.118\ pH \quad (2.3)$$

Where a_{Pb}^{2+} is the chemical activity of Pb^{2+}.

Figure 2.4 shows the equilibrium potential plotted as a function of pH for [Pb^{2+}][68]. In acidic and neutral solutions under open circuit, PbO_2 is metastable because it can be dissolved by reacting with water to yield oxygen and Pb^{2+}. On the other hand, in basic solutions PbO_2 is thermodynamically stable. If a potential positive to the equilibrium potential is applied, the PbO_2 coating will be formed or protected from corrosion. However, if a significant negative potential is applied relative to the equilibrium potential, it will induce a cathodic reduction and dissolution of the PbO_2 coating. It was reported that there are two phases of PbO_2, α-PbO_2 and β-PbO_2, and the phase has little effect on the thermodynamics of PbO_2 since their equilibrium potentials differ by ~10 mV.

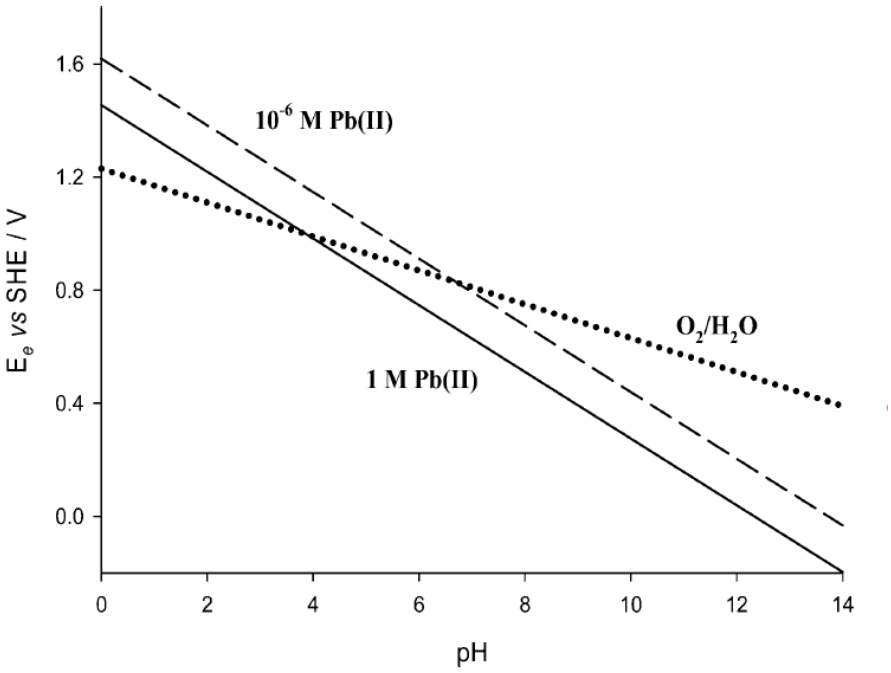

Figure 2.4 The equilibrium potential plotted as a function of pH for 10^{-6} M and 1M of [Pb^{2+}] (adapted from Ref. [68]).

Figure 2.5 shows a CV for PbO_2 deposition and dissolution in an acidic solution[69]. On the first scan (Scan 1) the deposition doesn't begin until the positive limit of 1.90 V and the anodic current density increases to a maximum at 1.80 V upon reversing the sweep derection. On the fifth scan (Scan 5) the deposition starts at a lower potential of 1.63 V, and the anodic current density is much higher and tending toward a mass transport-controlled plateau beyond 1.70 V. The reduction of PbO_2 to Pb^{2+} shows a sharp cathodic current peak below 1.20 V. With potential cycling, the deposition reaction involving nucleation and growth of PbO_2 on a working electrode leads to a thick PbO_2 coating.

Even though the deposition and reduction of PbO_2 on most electrodes and in many media are similar to that shown in Figure 2.5, their mechanisms are complex and multistep (see later), which requires further work to be able to discuss their quantitative kinetics. Importantly, figure 2.5 provides a useful guide to understand the behavior of PbO_2 electrodeposition in practice.

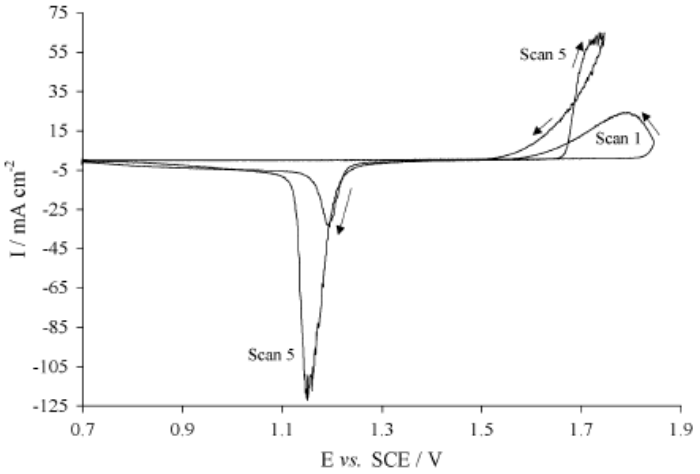

Figure 2.5 CV recorded in a solution of Pb^{2+} (300 mM) in aqueous methanesulfonic acid (2 M) (adapted from Ref. [69]).

2.3 ED of LHP

As discussed in the previous chapter, deposition techniques to grow perovskite films have been studied over the years to improve their surface quality. Film surfaces with low roughness, free from pinholes and large grain sizes dramatically improve the interfacial charge transfer to improve the efficiency of perovskite devices[70-73]. Meanwhile, the scalability of LHP is another challenge towards its commercial realization. The most used solution deposition technique is spin-coating, either one-step or two step, is limited by the formation of uncontrolled film morphology. Vacuum deposition has restrictions on high temperature and is not suitable for flexible materials. In 2015, Chen and co-workers first reported the electrodeposition of PbO_2 on TiO_2 followed by its conversion to $MAPbI_3$ as shown in Figure 2.6. A 4 cm^2 perovskite solar cell was fabricated to render a PCE improvement of 36.3% over the spin-coated counterpart[47]. Since then, electrodeposition has emerged as a scalable, cost-effective and environmentally friendly technique for perovskite synthesis.

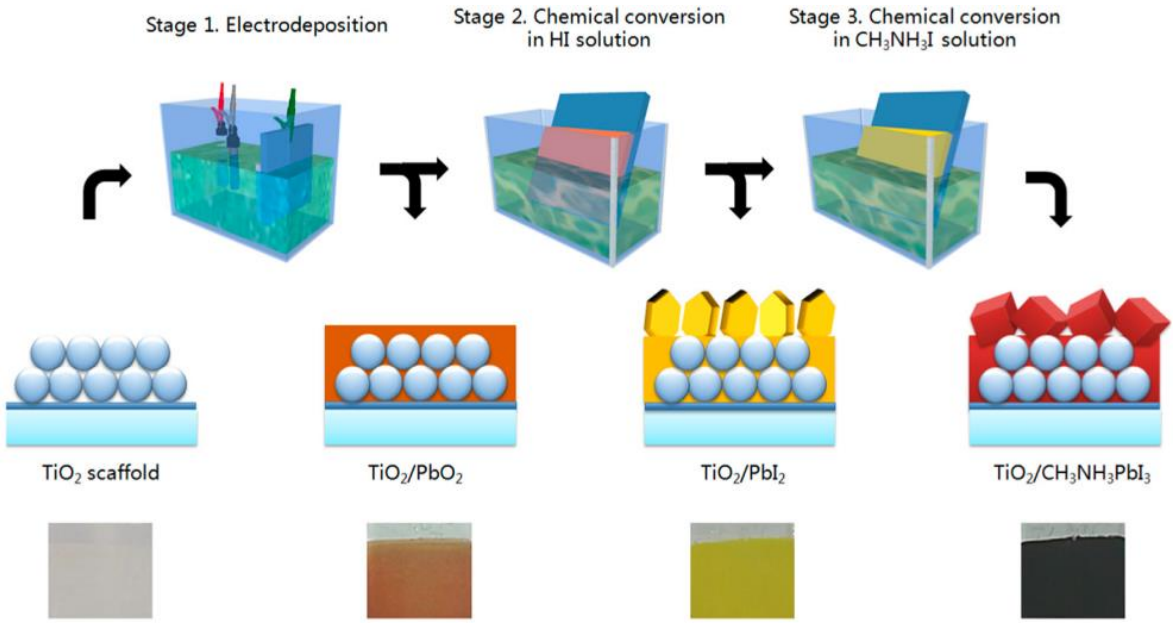

Figure 2.6 Schematic illustrating the fabrication processes of $MAPbI_3$ on TiO_2 scaffold (adapted from Ref. [47]).

The main challenge in ED of LHP is its solubility in water and polar solvents commonly used in electrochemistry. Dichloromethane (DCM) is the only solvent that has been identified to be suitable for electrochemical measurements on LHP[74, 75], which limits the direct ED of LHP due to the poor solubility of inorganic perovskite precursors in organic solvents. Alternatively, several methods to conduct part of LHP synthesis using ED have been developed, which may be combined with other scalable techniques such as chemical conversion, as shown in Figure 2.7[76].

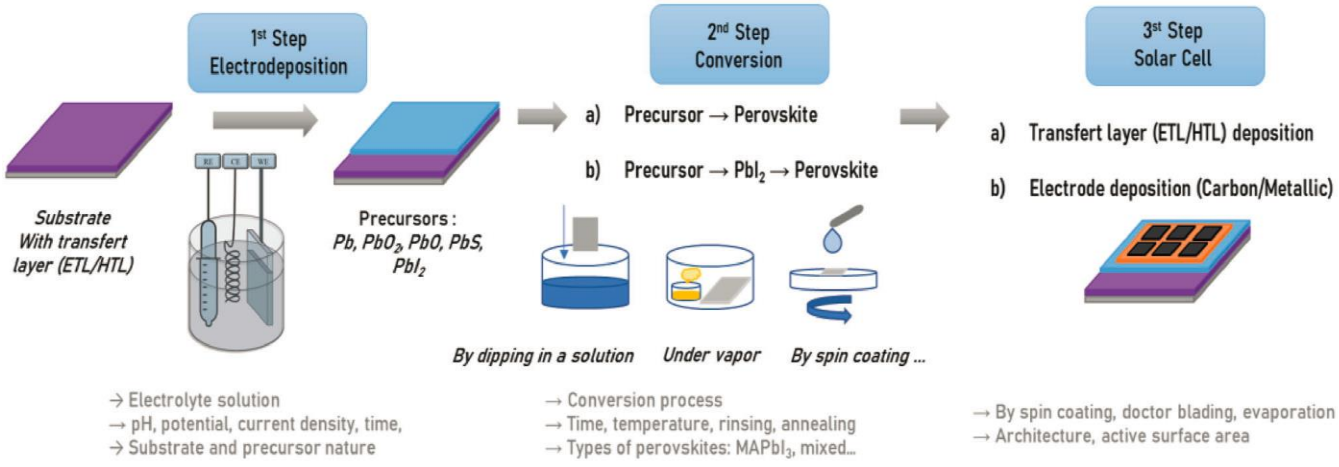

Figure 2.7 Electrodeposition for synthesis of LHP solar cells (adapted from Ref. [76]).

The ED process of LHP films typically consists of three steps. The first step is the ED of a precursor, in which PbO_2 is the most extensively studied due to its favorable LHP formation characteristics. The second step involves converting the precursor into a LHP film through a one or two-step chemical conversion using different methods like solution or vapor-based process. For large-scale applications, solution-based conversion is favorable as it enables the reuse of the conversion solutions and is easier to implement, providing both economic and environmental advantages. Three routes have been reported based on electrodeposited intermediates: lead chalcogen, lead halide, and metallic lead. For the lead chalcogen route, the first attempt used Pb^{2+} as the electroactive species to deposit a PbO_2 film, which is converted to $MAPbI_3$ by successively dipping in a HI and a MAI solution, as shown in Figure 2.6 and equation 2.4 to 2.6. The process involves the iodination of the deposited PbO_2 followed by an inter-diffusion reaction with MAI. The size of the PbI_2 crystal increased with decreasing HI concentration, and the larger PbI_2 crystals gave larger $MAPbI_3$ crystals. This established a versatile method to fabricate LHP films on large-scale, which readily control the morphology and quality of the perovskite and thus improve the PCE of perovskite devices[47].

$$Pb^{2+}\,(aq) + 2H_2O\,(l) \rightarrow PbO_2\,(s) + 4H^+\,(aq) + 2e^- \quad (2.4)$$

$$PbO_2\,(s) + 4HI\,(aq) \rightarrow PbI_2\,(s) + 2H_2O\,(l) + I_2\,(s) \quad (2.5)$$

$$PbI_2\,(s) + MAI\,(aq) \rightarrow MAPbI_3\,(s) \quad (2.6)$$

Popov et al. electrodeposited a PbO_2 film and then sequentially exposed it to HI and MAI vapors for the conversion to $MAPbI_3$ (equation 2.7 to 2.13)[77]. The vapor exposure allows grain growth and mitigates void formations to improve the quality of the final $MAPbI_3$ film. Furthermore, the crystal phase of the $MAPbI_3$ and grain size can be adjusted by controlling the duration of the exposure to MAI vapor.

$$OH^- - e^- \rightarrow OH_{ads} \quad (2.7)$$

$$Pb^{2+} + OH_{ads} + OH^- - e^- \rightarrow Pb(OH)_2^{2+} \quad (2.8)$$

$$Pb(OH)_2^{2+} \rightarrow PbO_2 + 2H^+ \quad (2.9)$$

$$PbO_2\,(s) + 4HI(g) \rightarrow PbI_2\,(s) + I_2\,(g) + H_2O\,(g) \quad (2.10)$$

$$PbO_2\,(s) + 3HI\,(g) \rightarrow PbI(OH)\,(s) + I_2\,(g) + H_2O\,(g) \quad (2.11)$$

$$PbI(OH)\,(s) + HI(g) \rightarrow PbI_2\,(s) + H_2O\,(g) \quad (2.12)$$

$$PbI_2\,(s) + MAI\,(g) \rightarrow MAPbI_3\,(s) \quad (2.13)$$

Pan et al. electrodeposited PbO_2 in a concentrated basic solution on ITO using cyclic voltammetry, and directly converted PbO_2 to $MAPbI_3$ by dipping it in a MAI solution in a one-

step conversion process (equation 2.14 to 2.15)[78]. The density gradient of $MAPbI_3$ crystal particle was observed as a function of the electrochemical potential, where a high-potential led to high number of nucleation sites to form a high-density $MAPbI_3$ film.

$$Pb^{4+} + 2I^- \rightarrow Pb^{2+} + I_2 \quad (2.14)$$

$$PbI_2 + MAI \rightarrow MAPbI_3 \quad (2.15)$$

Another approach is to electrodeposit PbO followed by converting it to $MAPbI_3$ through solid-solid interdiffusion reaction with MAI at 150 ^oC, as shown in Figure 2.8 and equation 2.16 to 2.20. The mechanism of formation of PbO originates from the interaction of Pb^{2+} in solution with OH^- generated at the cathode, and eventually the generation of $Pb(OH)_2$ that is dehydrated to form PbO with thermal annealing at 200 ^oC[79].

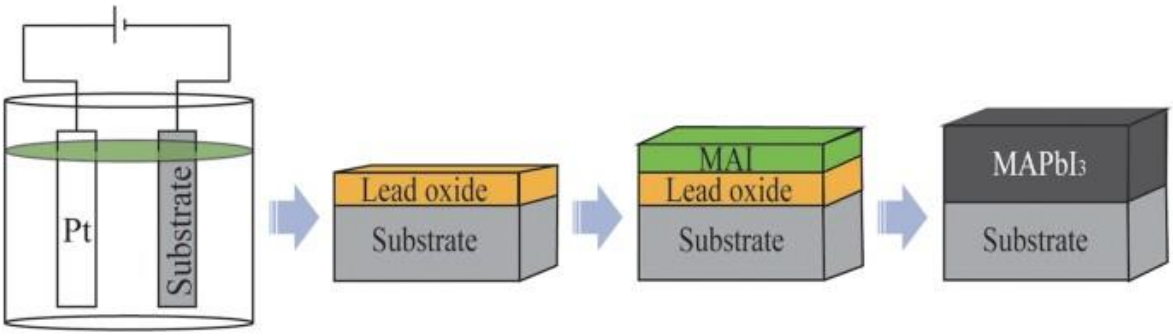

Figure 2.8 Schematic illustration of PbO electrodeposition and subsequent reaction with MAI (adapted from Ref. [79]).

$$Pb^{2+} + 2OH^- \rightarrow Pb(OH)_2 \quad (2.16)$$

$$Pb(OH)_2 \rightarrow PbO + H_2O \quad (2.17)$$

$$MAI \rightarrow CH_3NH_2 + HI \quad (2.18)$$

$$PbO + 2HI \rightarrow PbI_2 + H_2O \quad (2.19)$$

$$PbI_2 + MAI \rightarrow MAPbI_3 \quad (2.20)$$

In another report, lead sulfide (PbS) was electrodeposited by cyclic voltammetry in aa acidic (pH 2) solution, which was then used as a seeding layer for subsequent solution conversion to PbI_2 and $MAPbI_3$, as shown in equation 2.21 to 2.23[80].

$$S_2O_3^{2-} + 2H^+ \rightarrow S + SO_2 + H_2O \quad (2.21)$$

$$S_{adsorbed} + 2H^+ + 2e^- \rightarrow H_2S \quad (2.22)$$

$$Pb^{2+} + S + 2e^- \rightarrow PbS \quad (2.23)$$

The lead halide route was reported in 2018, Li et al. directly electrodeposited PbI_2 on TiO_2 layer using cyclic voltammetry, followed by converting to $MAPbI_3$ in a MAI solution[81]. The possible reaction mechanism was described as shown in equation 2.21 to 2.23. However, the electrochemical solution contained Pb^{2+} and I_2 with the pH adjusted by nitric acid, which makes the electrolyte composition complicated.

$$Pb^{2+} + 2e^- \rightarrow Pb \quad (2.21)$$

$$I_2 + 2e^- \rightarrow 2I^- \quad (2.22)$$

$$2Pb^{2+} + 2I^- \rightarrow 2PbI_2 \quad (2.23)$$

The metallic lead route was developed in 2020, Wang et al. carried out the ED of Pb onto TiO_2/FTO with 0.02M PbI_2 isopropanol solution, followed by converting Pb into $CsPbBr_3$ under a positive bias in a CsBr methanol solution, as shown in Figure 2.9[82]. The film coverage of $CsPbBr_3$ was almost 100% after conversion due to the volume expansion of Pb to $CsPbBr_3$. The thickness and grain size of $CsPbBr_3$ can be controlled by simply tuning the parameters such as current, voltage and time. Furthermore, the as-fabricated perovskite cell still maintained ~99.7% of its original PCE even after 150 days of exposure to air, showing a robust stability against environmental conditions.

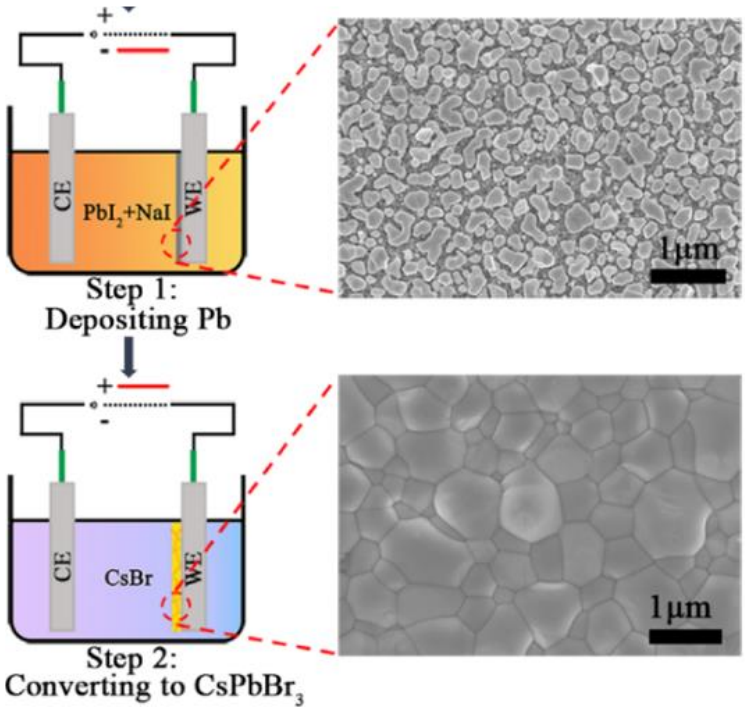

Figure 2.9 Schematic illustration of electrodeposition of $CsPbBr_3$ film (adapted from Ref. [82]).

In addition to the one-step ED of Pb, a two-step ED has been reported to synthesize $MAPbI_3$[83].

The two-step ED process involves the deposition of Pb, followed by ED of MAI on Pb film to convert it to $MAPbI_3$. The best PCE of the prepared PSC was 16.7%.

Recently, mixed-halide perovskites prepared by ED have been explored. Heydari et al. synthesized $MAPbI_xBr_{(3-x)}$ through exposure of the electrodeposited PbO_2 to HI/HBr and MAI/MABr vapors subsequently[84]. Later, they showed that the direct conversion of PbO_2 to $MAPbI_xBr_{(3-x)}$ led to a uniform layer with superior performance[85]. Li et al, sequentially spin-coated FAI/MACl or FAI/MABr solutions on the electrodeposited PbO_2 film to prepare a $FAPbI_3$ film. Compared with MACl, the addition of MABr suppressed the formation of the non-perovskite δ-$FAPbI_3$ phase and improved the film coverage of the α-$FAPbI_3$ perovskite phase. The MABr-doped $FAPbI_3$ film exhibited about 20 times higher PCE than that of PbI_2-based LHP under the same conditions[86].

ED is a bottom-up scalable approach that is used for the deposition of thin films, allowing the formation of various intermediates to form uniform LHP films. This provides a versatile tool to prepare high quality perovskite with controlled film morphology even despite the solubility issues of perovskites in polar solvents[75]. Besides, ED can be also used to prepare inorganic or organic (polymeric) contacts in perovskite devices such as the hole transport layer (HTL) and the electron transfer layer (ETL) in LHP solar cells, which can facilitate the fabrication process.

2.4 X-Ray Diffraction (XRD)

XRD is a non-destructive method for the determination of crystal structure, orientation, size, and phase identification. XRD peaks are produced by constructive interference of a monochromatic beam of X-rays that diffracts at specific angles from each set of lattice planes of a crystal sample. The peak intensity can be determined from the atomic positions within the lattice planes. Herein, the crystallinity and structure of a perovskite film was measured using XRD. By this method, it is also possible to identify the orientation and size of the perovskite grains. XRD provides a method to monitor the perovskite thin films' internal structure changes over time. For example, XRD was used to monitor the change of crystalline phases of $MAPb(ICl)_3$ in real time during its preparation by vacuum-based coevaporation (Figure 2.10), and confirmed a recrystallization process and preferential orientation effects as well as the decomposition temperature during its post deposition annealing[87].

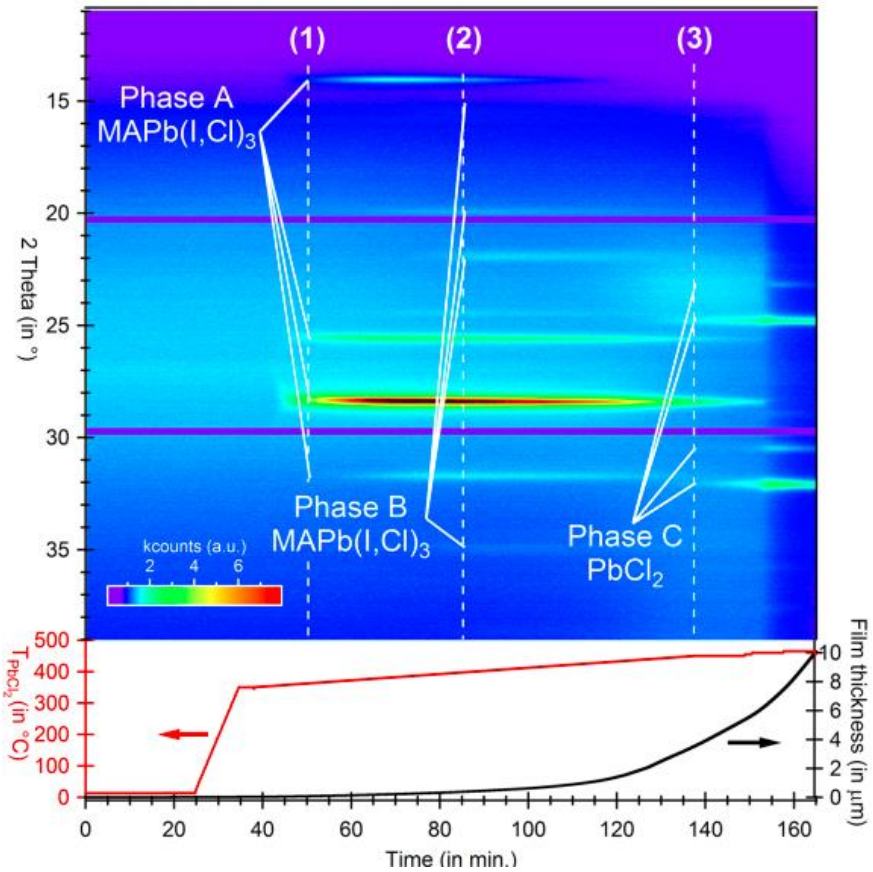

Figure 2.10 Color-coded representation of the diffracted intensity measured during $MAPb(ICl)_3$ formation. Three different crystalline phases A, B, and C can be detected in different growth regimes (adapted from Ref. [87]).

2.5 Scanning Electron Microscope (SEM)

SEM is a powerful technique used for the visualization and characterization of surfaces. In SEM, an electron beam with low energy is radiated onto the material and scans the surface of the sample, which leads to the emission of photons and electrons from the sample surface. In order to generate an image, the receiving signals produced from the electron–sample interactions are detected with a detector and analyzed by the software. SEM has been widely used to image perovskite film surface coverage, grain size and film thickness, which are key characteristics for the performance of perovskite devices. There is no metallization needed for sample preparation as perovskite films are typically deposited on conductive substrates, such as Indium Thin Oxide (ITO) and fluorine-doped tin oxide (FTO). It is difficult to obtain clear cross-section images because a perfect cut is needed to avoid charging issue. Therefore, metallization with gold or platinum is need to address this issue[88].

The first common use for SEM is to improve the surface coverage of perovskite film. Several

solution and vacuum-assisted depositions were optimized by analyzing SEM images to improve the performance of perovskite devices. Huang, et al., reported that the use of a gas flow during the spin-coating process produced a uniform $MAPbI_3$ film fully covered by densely packed single crystalline grains, which led to a high PCE of 15.7% for $MAPbI_3$ solar cell[89]. Another common use for SEM is to identify the perovskite grains. Chen, et al. determined the grain size and film morphology of $MAPbI_3$ for the optimization of photovoltaic properties of PSC[90]. You et al. confirmed the location of 2D flakes at perovskite grain boundaries, which conducted holes from the grain boundaries to the HTL in PSCs, thereby inducing a more pronounced performance enhancement of the devices, as shown in Figure 2.11[91].

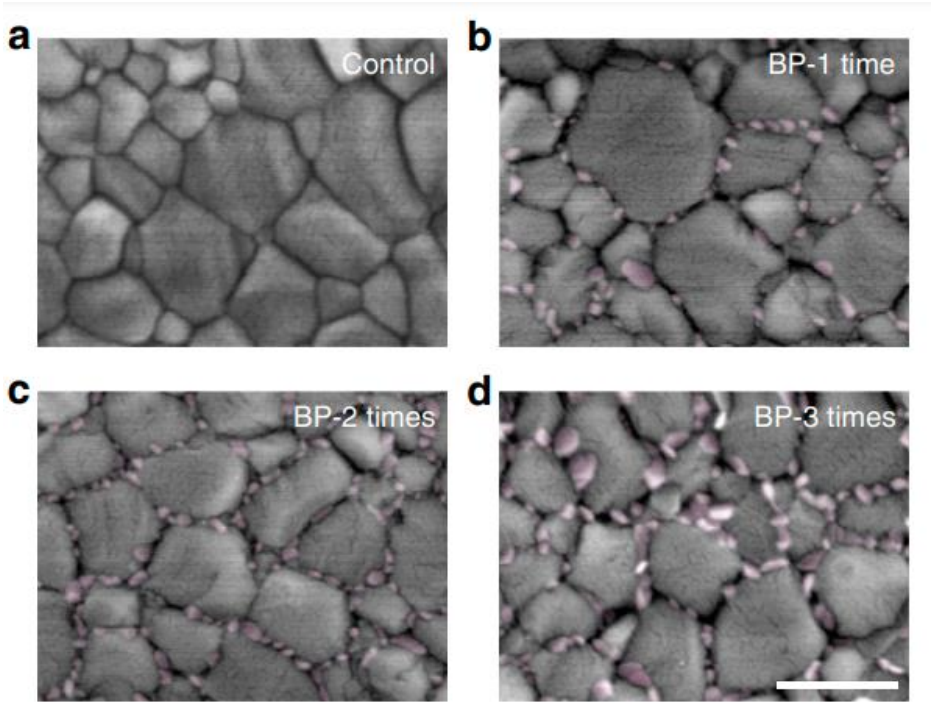

Figure 2.11 Morphology of black phosphorus (BP)-modified $MAPbI_3$ perovskite films. SEM images of the perovskite films without and with 1 - 3 coats of BP flakes. The scale bar is 500 nm (adapted from Ref. [89]).

2.6 Linear sweep voltammetry (LSV) and Cyclic voltammetry (CV)

In LSV a linear potential ramp is applied to the electrode as an excitation signal and the current is recorded in response to the change in potential. As shown in Figure 2.12, the scan begins from V_1 where no current flows. As the potential is swept to V_2, a current starts to flow and then reaches a peak at E_p^c. The Nernst equation (equation 2.24) is used to relate the potential and concentration of the redox species at the electrode surface.

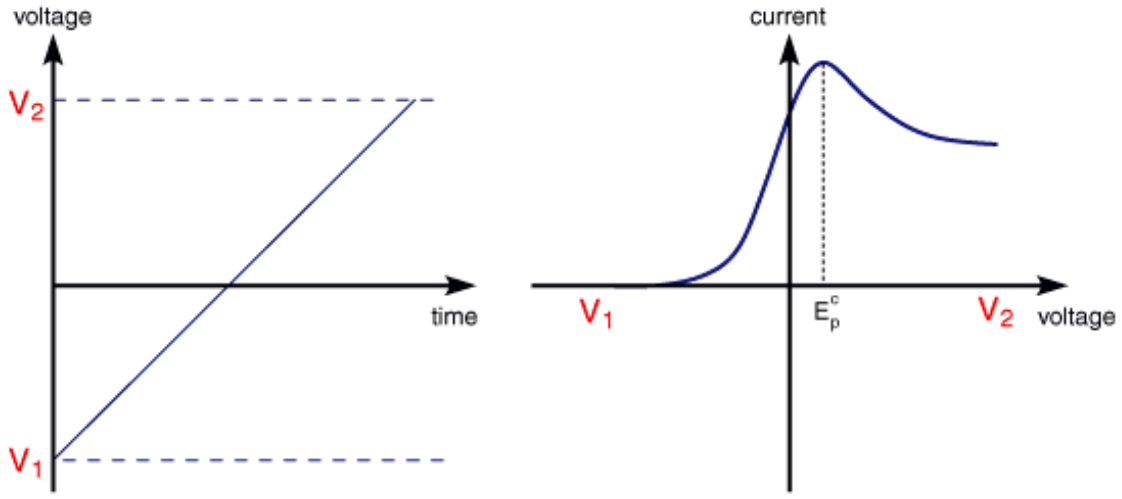

Figure 2.12 linear potential ramp as an excitation signal (left). The resulting voltammogram (right) (adapted from Scholz F., 2015).

$$E = E^0 + \frac{RT}{nF} \ln \frac{(Ox)}{(Red)} \qquad (2.24)$$

where E is the applied potential, E^o is the standard reduction potential of the species, R is the gas constant, T is the temperature, n is the number of electrons exchanged, F is Faraday's constant, (Ox) and (Red) are the relative activities of the oxidized and reduced species. The current rises as the potential is swept from V_1 to V_2. At some point the diffusion layer grows sufficiently large at the electrode surface, and the flux of reactant to the electrode is not fast enough to reach the electrode surface, the current begins to drop.

In LSV, the potential is scanned in one direction, either to positive potentials or to negative potentials. In CV, the potential is scanned in both directions. Figure 2.13a shows a typical potential-excitation signal[92]. In the forward scan from E_1 to E_2, Fc^+ is depleted and reduced to Fc which results in a cathodic current and depletion of Fc^+ at the electrode surface (equation 2.25). The cathodic peak current ($i_{P,C}$) at C is caused by the diffusion of additional Fc^+ from bulk solution, and then the current decreases with the mass transport of Fc^+ to the electrode slowing down due to the increasing diffusion layer containing Fc at the electrode surface. The scan direction is reversed at D to the positive potential, G. Fc at the electrode surface is depleted by oxidizing to Fc^+ as the applicated potential goes more positive (equation 2.26), which leads to an anodic current. B and E indicate the equal concentration of Fc^+ and Fc at the electrode surface, following Nernst equation as $E = E_{1/2} = \frac{E_{p,c} + E_{p,a}}{2}$. This halfway potential between cathodic and anodic peaks is used to estimate the standard potential of a species (E^0).

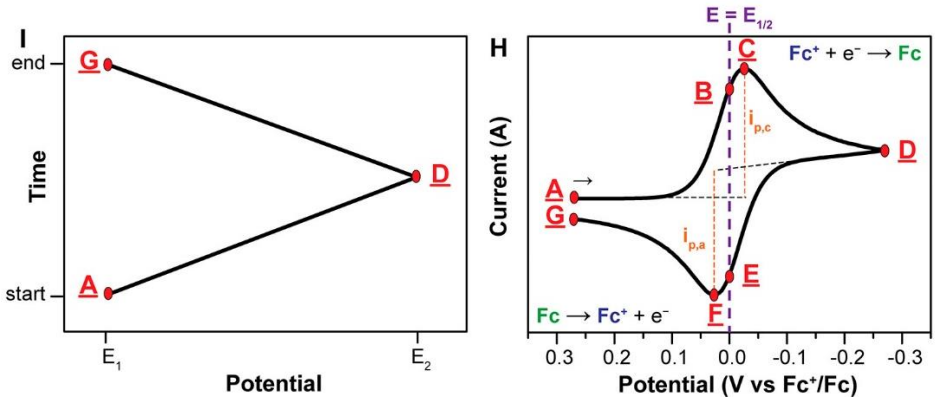

Figure 2.13 (a) Applied potential as a function of time for a CV with the initial, switching, and end potentials represented (A, D, and G, respectively); (b) Voltammogram of the reversible reduction of a 1 mM Fc^+ solution at 100 mV/s (adapted from Ref. [90]).

$$Fc^+ + e \rightarrow Fc \quad (2.25)$$

$$Fc \rightarrow Fc^+ + e \quad (2.26)$$

The cathodic and anodic current peaks are separated because of the diffusion of species to and from the electrode surface, which follows the Randles-Sevcik equation:

$$i_p = \left(2.69 \times 10^5\right) n^{3/2} A D^{1/2} \nu^{1/2} C_A \quad (2.27)$$

where n is the number of electrons in the redox reaction, A is the area of the working electrode, D is the diffusion coefficient for the electroactive species, v is the scan rate, and C_A is the concentration of the electroactive species at the electrode.

2.7 Ultraviolet-Visible (UV-Vis) spectroscopy to determine bandgap (E_g)

In UV-Vis spectroscopy, the light absorption is measured as function of wavelength, which provides the information about electronic transitions occurring in the light absorber. The Beer-Lambert law states that the light absorption through a medium is proportional to the optical properties of the light absorber (ε), the concentration of the light absorber (C), and the light pathlength (l) in the medium, as shown in equation 2.28[93].

$$A_\lambda = \varepsilon_\lambda * C * l \quad (2.28)$$

Where A_λ is the absorbance at a given wavelength λ, and ε_λ is the molar absorptivity of the absorber at λ. Rewriting equation 2.28 to include the light transmitted (I_T) over the incident intensity (I_0) gives equation 2.29:

$$A_\lambda = \varepsilon_\lambda * C * l = -\log_{10}\left(\frac{I_T}{I_0}\right) \quad (2.29)$$

The determination of E_g for a semiconductor can be determined from a UV-Vis absorption spectrum, which refers to the energy difference between the top of valence band (VB) and the bottom of conduction band (CB) of a semiconductor (see Figure 2.14). In order to promote electrons from the VB to the CB, a minimum energy is required for this transition, E_g. Since the absorption spectra are reported in units corresponding to light wavelength rather than energy, the conversion between wavelength (nm) and energy (eV) is given by equation 2.30:

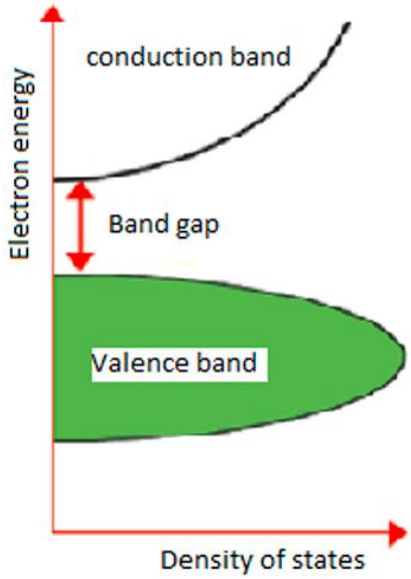

Figure 2.14 Schematic illustration of bandgap (adapted from Seema M., 2023).

$$h\nu\ (\mathrm{eV}) = \frac{hc}{\lambda} = \frac{1239.8\ (\mathrm{eV} \times \mathrm{nm})}{\lambda\ (\mathrm{nm})} \qquad (2.30)$$

E_g in an absorption spectrum corresponds to the point at which the absorption starts to increase, indicating the minimum energy required for a photon to excite electrons from the VB to the CB. A typical E_g analysis involves plotting and fitting the absorption data for direct and indirect bandgap semiconductors, known as a Tauc plot. The absorbance is first normalized to the light pathlength to give the absorption coefficient (α) by equation 2.31:

$$\alpha(\mathrm{cm}^{-1}) = \frac{\ln(10) * A}{l(cm)} = \ln(10) * \varepsilon * C \qquad (2.31)$$

For α values greater than 10000 cm^{-1}, it usually obeys the following relation [94, 95]:

$$\alpha h\nu \propto (h\nu - E_g)^n \qquad (2.32)$$

where n is 1/2, 3/2, 2, or 3, corresponding to direct (allowed), direct (forbidden), indirect

(allowed), or indirect (forbidden) transitions, respectively. A Tauc plot of $(\alpha h\nu)^{1/n}$ vs. hv gives the value of E_g when extrapolating to the baseline. For α less than 10000 cm^{-1}, a Tauc plot is no longer applicable.

For semiconductors, UV-Vis spectroscopy provides a convenient method to estimate their optical bandgap. Duha et al. synthesized $MAPbI_3$ perovskite films using two-step and one-step spin-coating approaches, and determined their E_g by UV-Vis absorption and Tauc plot, as shown in Figure 2.15[96]. Kuan et al. co-doped lead and tin to synthesize inorganic Sn-Pb mixed perovskites, and calculated their E_g using UV-Vis absorption and Tauc plot (see Figure 2.16)[97].

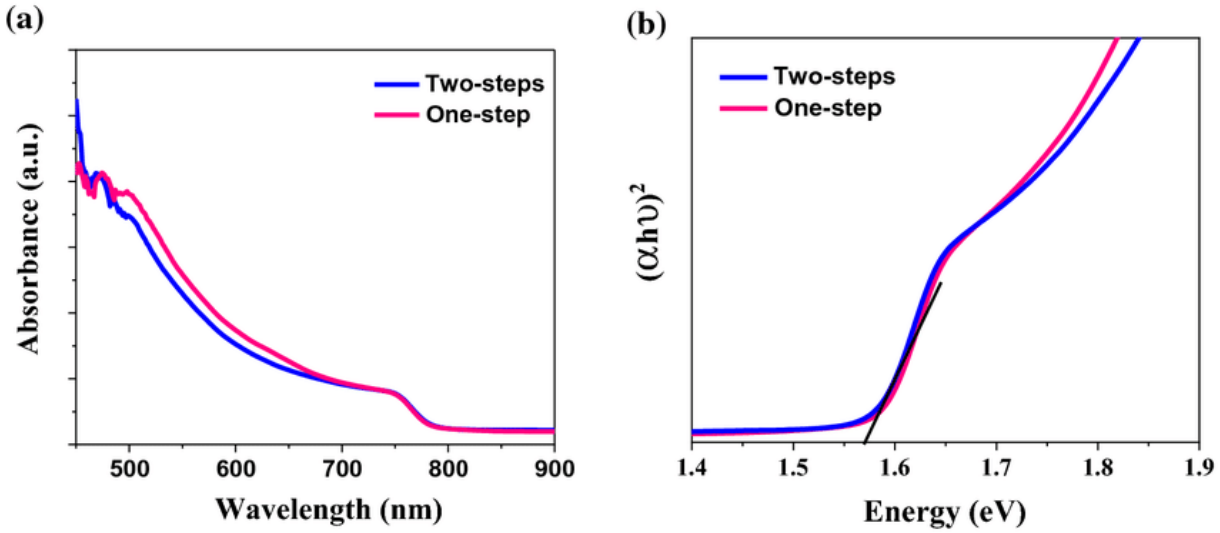

Figure 2.15 $MAPbI_3$ perovskite synthesized by two-step and one-step spin-coating approaches; (a) UV-Vis absorption spectra, (b) Tauc plots (adapted from Ref. [92]).

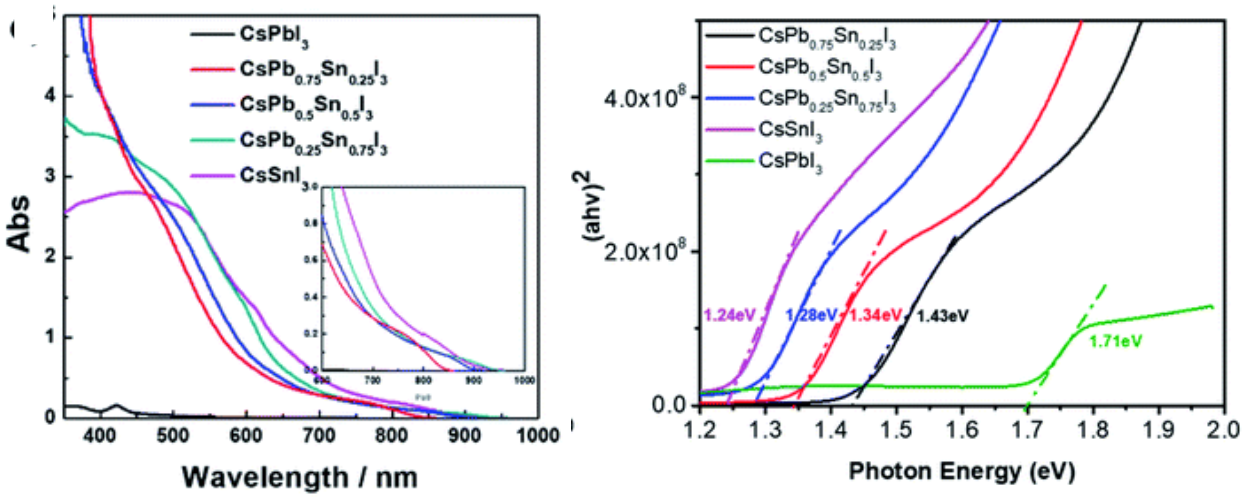

Figure 2.16 (left) The absorption spectra of $CsPb_xSn_{1-x}I_3$ synthesized by the antisolvent washing method. (right) Tauc plot of $CsPb_xSn_{1-x}I_3$ inorganic perovskites (adapted from Ref. [93]).

2.8 Photoluminescence (PL)

PL is a process in which a sample is irradiated with photons of a higher energy than its bandgap, and later this energy is dissipated by the emission of light[98]. Figure 2.17 schematically illustrates the mechanism of PL in semiconductors, which plots the kinetic energy (E) vs. wave vector (or momentum vector, *k*) for direct and indirect bandgap semiconductors. The difference between direct and indirect bandgap semiconductors is the relative position of the VBM and the CBM. In a direct bandgap semiconductor, both VBM and CBM occur at the zone center, $k = 0$. In an indirect bandgap semiconductor, CBM shift from $k = 0$ to other values of *k*. Upon absorption of an ultraviolet or visible photon with an energy ($h\omega$) higher than E_g of semiconductor, an electron-hole (e^--h^+) pair is generated and ab e^- is excited to the CB. In contrast to a direct bandgap semiconductor without the assistance of a phonon during its absorption, the photon absorption process for an indirect semiconductor is assisted by either emitting or absorbing a phonon due to the different k values for the VBM and the CBM. The excited e^- will rapidly relax from its initial excited state to the lowest excited state (CBM) by emitting phonons, following recombining with h^+ radiatively with emission of a photon or transferring its energy to defects or impurities nonradiatively. Since electrons and holes accumulate at the CBM and the VBM respectively prior to recombination, the energy difference between electrons and holes approximately equals E_g. Therefore, PL occurs at an energy close to E_g of the semiconductor.

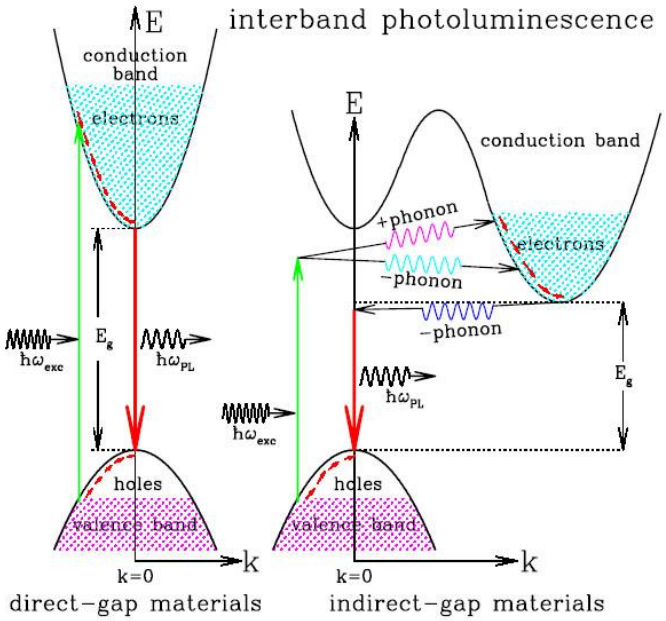

Figure 2.17 Schematic photoluminescence process in direct (left) and indirect (right) bandgap semiconductors. The blue dots at the bottom of the conduction band and the void at the top of the valence band represent the electrons and holes created by the absorption energy > E_g (adapted from Manal A-B., 2006).

PL is widely used to characterize the optoelectronic properties of LHPs, such as bandgap[99-102], charge carrier mobilities and lifetimes[103-108], and phase segregation[109-111]. Meanwhile, PL is an effective approach to pinpoint the defect and impurity states of LHPs which are observed at photon energies below E_g[112]. If these states are radiative, they will generate unique PL peaks. In addition to identifying the radiative states, PL peak position is also useful to evaluate the composition-dependent bandgap for analyzing the phase segregation of LHP[113]. Under light illumination, the I/Br-mixed perovskite decomposed to I-rich and Br-rich regions due to photo-induced phase segregation, as shown in Figure 2.18[114]. Such phase segregation can be investigated by PL mapping in which the PL spectrum from different regions of a perovskite film can be recorded and the fingerprints of I-rich and Br-rich regions can be detected[115]. A further study showed that this type of phase segregation was reversible after keeping the perovskite film in the dark[116, 117]. In addition to mixed-halide perovskites, for pure $MAPbI_3$ it was reported that I^- can diffuse towards the GB under light illumination and then return after storing in the dark[118].

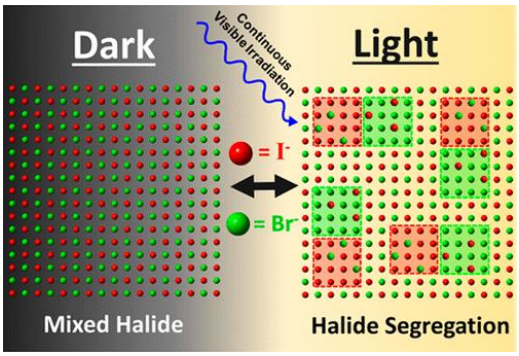

Figure 2.18 Schematic Photo-induced segregation of mixed-halide perovskites (adapted from Ref. [110]).

PL mapping traditionally uses a point-by-point scanning approach, which takes a relatively long time as well as compromise the spatial resolution and measurement repeatability due to mechanical transition. However, by using a hyperspectral imaging approach, the measurement number and mechanical transition can be significantly reduced by simultaneously sampling the whole area of interest, which makes it popular in recent years for the simultaneous imaging of perovskite materials. Stranks et al. studied the fundamental properties of $(Cs_{0.06}MA_{0.15}FA_{0.79})Pb(Br_{0.4}I_{0.6})_3$ film by means of hyperspectral PL imaging, as shown in Figure 2.19 [119]. it was found that Illumination led to the formation of I-rich sites on the surface of perovskite film, revealing the impact of photo-induced phase segregation in mixed-halide perovskites.

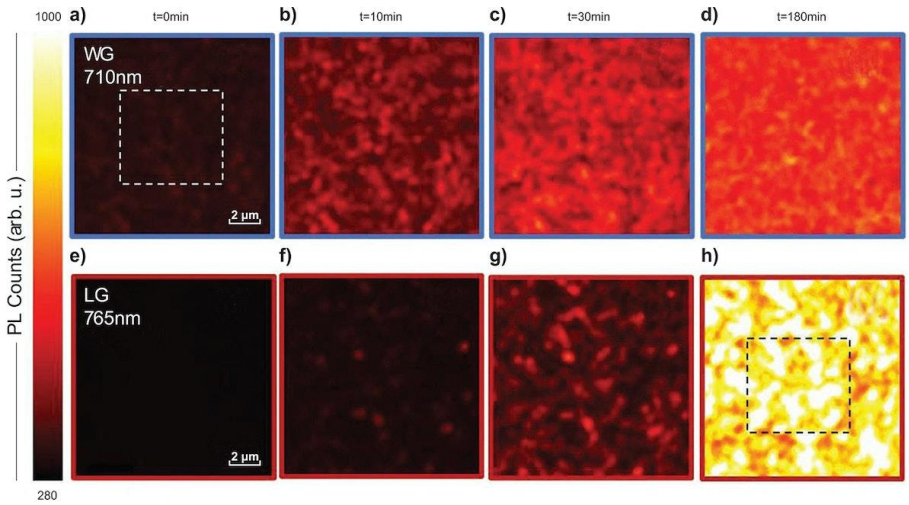

Figure 2.19 In situ hyperspectral PL maps for wide-bandgap (a-d) and low-bandgap peaks (e-h) in $(Cs_{0.06}MA_{0.15}FA_{0.79})Pb(Br_{0.4}I_{0.6})_3$ film over time under white-light illumination with an intensity of 290 mW/cm^2 for the sample before treatment (t = 0), during the treatment (10 and 30 min), and once the emission intensity reaches stabilized emission (180 min) (adapted from Ref. [115]).

CHAPTER 3

Chemical conversion of electrodeposited PbO_2 to the all-inorganic cesium lead halide perovskites $CsPbBr_3$ and $CsPbCl_3$

Abstract**:**

There is increasing interest in the development of stable, wide bandgap lead halide perovskites for application as photoelectrodes, light emitting diodes and photosensors. In this work, lead dioxide was electrodeposited from an aqueous electrochemical bath and transformed by a two-step chemical conversion process to $CsPbI_3$, $CsPbBr_3$ and $CsPbCl_3$. X-ray diffraction and scanning electron microscopy measurements confirmed the two-step chemical conversion of PbO_2 to $PbBr_2$ or $PbCl_2$ followed by their conversion to the all-inorganic lead halide perovskites $CsPbBr_3$ or $CsPbCl_3$. It was found that chemical conversion of PbO_2 to PbI_2 and then $CsPbI_3$ led to the nonperovskite δ-$CsPbI_3$. This work presents the first example of the chemical transformation of electrodeposited PbO_2 to $PbBr_2$ and $PbCl_2$ to form wide bandgap $CsPbBr_3$ and $CsPbCl_3$ perovskites. Absorbance spectroscopy measurements confirmed the optical gap of the wide bandgap $CsPbBr_3$ and $CsPbCl_3$ materials while linear sweep voltammetry measurements demonstrated that $CsPbCl_3$ has a larger electrochemical stability window than $CsPbBr_3$.

Keywords**:** Electrodeposition, Perovskite, Photovoltaic, Corrosion, Stability, Mixed halide.

3.1. Introduction

Lead halide perovskites $APbX_3$, where A is an organic (or inorganic) cation and X is a halide anion, are being rapidly developed following the demonstration of high efficiency photovoltaic devices based on methyl ammonium lead iodide ($MAPbI_3$) [120-122]. These materials can be prepared using mild synthesis conditions and exhibit a long charge carrier diffusion length, high quantum efficiency and a high absorption coefficient [123]. Through substitution at the X-site it is possible to tune the perovskite bandgap enabling a variety of applications such as lasers, light-emitting diodes and photodetectors, which have been further expanded through substitution with the inorganic cation cesium at the A site to form an all-inorganic counterpart [124]. A limitation in the commercialization of lead halide perovskite devices is the development of large area coating methods [125]. Due to the mild conditions required for their preparation, electrodeposition from an aqueous solution stands out as a promising method for the sustainable fabrication of large area thin film perovskites [47, 77].

The use of electrodeposition to prepare lead halide perovskite thin films has focused primarily on the hybrid organic–inorganic perovskite $MAPbI_3$ using electrodeposited PbO_2 for photovoltaic

applications [47]. The electrodeposited PbO_2 layer can be chemically converted to $MAPbI_3$ in a one-step chemical conversion process [126], or by a two-step chemical conversion to PbI_2 and then $MAPbI_3$ [47]. Alternatively, PbI_2 can be electrochemically deposited directly and then chemically converted to $MAPbI_3$ [127, 128]. More recently, a few examples of the electrodeposition of $CsPbI_3$ and $CsPbBr_3$ inorganic lead halide perovskites have appeared without any examples of the electrodeposition of $CsPbCl_3$. In one example, aragonite crystallites ($CaCO_3$) were electrodeposited followed by a two-step chemical conversion process to form surface-confined $CsPbBr_3$ perovskite nanocrystals on a $PbCO_3$ scaffold [129]. In the other examples, a two-step chemical conversion of electrodeposited PbO_2 to PbI_2 was used to form $CsPbBr_3$ or $CsPbI_3$ or the mixed halide $CsPbI_2Br$ [82, 130, 131]. However, the use of iodide during chemical conversion could be problematic for long-term stability as the photoactive perovskite α-$CsPbI_3$ is unstable at room temperature and transforms into the non-functional δ-$CsPbI_3$. In the case of electrodeposited $CsPbI_3$, an innovative approach was used to form the perovskite inside a TiO_2 host matrix to avoid this transformation. However, for thin film devices based on bromide or chloride lead halide perovskites, the uncontrolled presence of unreacted PbI_2 could potentially negatively affect the optoelectronic properties and long-term stability due to the presence of a secondary phase or alternatively through photo-induced phase segregation that can occur when a mixed halide material is formed [132]. Here we show that electrodeposited PbO_2 can be chemically converted directly to either $PbBr_2$ or $PbCl_2$ to form thin films of the all-inorganic cesium lead halide perovskites $CsPbBr_3$ and $CsPbCl_3$, respectively.

3.2. Materials and methods

3.2.1. Chemicals and materials

Methanol (HPLC, ≥ 99.9%), ethanol (anhydrous, ≥ 99.5%), acetone (ACS reagent, ≥ 99.8%), acetic acid (ACS reagent, ≥ 99.7%), hydrochloric acid (ACS reagent, 37%), hydrobromic acid (ACS reagent, 48%), hydroiodic acid (ACS reagent, 55%), sodium acetate trihydrate (ACS reagent, ≥ 99%), lead acetate trihydrate (ACS reagent, ≥ 99%), cesium chloride (99.9%), cesium bromide (99.9%) and cesium iodide (99.9%) were purchased from Sigma-Aldrich. All chemicals were used as received without further purification. Fluorine-doped tin oxide coated glass substrates (FTO, 6–9 Ω/square) were purchased from Delta Technologies, Inc. Water was purified using a Millipore system (18.2 MΩ cm).

3.2.2. Electrodeposition

Fluorine-doped tin oxide glass slides (0.5 cm × 2.5 cm) were cleaned successively for 20 min in

acetone, methanol and water followed by drying with compressed air. The electrodeposition bath was an aqueous solution (pH 5.5) containing 1.0 M sodium acetate and 0.1 M lead (II) acetate. Concentrated acetic acid was used to adjust the pH. Electrodeposition was carried out according to the method of Popov et al. [77] using a current density of 0.25 $mA \cdot cm^{-2}$ for 900 s using a potentiostat (Solartron 1470) under ambient conditions in a three-electrode cell using a FTO slide as working electrode (area 1 cm^2), a platinum gauze counter electrode and an Ag wire quasi-reference electrode. The resulting PbO_2 film on FTO was rinsed with water and annealed at 100 ◦C in air for 10 min.

3.2.3. Two-step chemical conversion of PbO_2 to $CsPbX_3$

Conversion of the as-deposited PbO_2 to PbX_2 was carried out in ethanol containing 50 mM of the corresponding hydrohalic acid, using a conversion time of 6 min for PbI_2, 4 h for $PbBr_2$ and 40 min for $PbCl_2$ at room temperature. The subsequent conversion of PbX_2 to $CsPbX_3$ was achieved by immersing the PbX_2 thin films in methanol containing 20 mM CsX for 60 min at room temperature, followed by thermal annealing at 100 ◦C for 10 min.

3.2.4. Characterization

UV–Vis absorption spectra were obtained with a UV–VIS-NIR spectrophotometer (Lambda 750, Perkin-Elmer). X-ray diffraction patterns were obtained using a Bruker D8 Advance diffractometer with a Cu-Kα radiation source. Images of the surface morphology of the perovskite films were obtained using a scanning electron microscope (SEM) (JEOL JSM7600F).

3.2.5. Electrochemical measurements

Electrochemical measurements were carried out in a sealed electrochemical cell using a potentiostat (Solartron 1470). $CsPbX_3$ films with ~0.2 cm^2 area exposed to the electrolyte functioned as the working electrode, a Pt wire as the counter electrode, and an Ag wire as a quasi-reference electrode. The Ag wire quasi-reference electrode was stored in a supporting electrolyte of 0.1 M tetrabutylammonium hexafluorophosphate ($TBAPF_6$) in dichloromethane and the stability of its potential was verified at the end of each voltammetric measurement using the formal potential for the oxidation/reduction of the ferrocene/ ferrocenium redox couple. The supporting electrolyte used for all electrochemical measurements was 0.1 M $TBAPF_6$ in dichloromethane. The solution was purged by argon bubbling for 10 min before measurement.

3.3. Results and discussion

Lead halide perovskites were prepared by the electrodeposition of PbO_2 followed by a two-step chemical conversion process. In each step of the chemical conversion process, the solvent used was selected based on its ability to dissolve the hydrohalic acid or cesium salt while avoiding the dissolution of the newly formed film, either lead halide or cesium lead halide, respectively. For these reasons, ethanol was used in the first step while methanol was used in the second step. The chemical conversion of the electrodeposited PbO_2 to PbX_2 (X represents the halide) was carried out in ethanol containing 50 mM of the corresponding hydrohalic acid. The hydrohalic acid concentration has a large effect on film morphology during the chemical conversion of PbO_2 to PbI_2, with high HI concentrations (6.25 M) leading to an accelerated PbI_2 dissolution whereas lower concentrations (50 mM) yield larger PbI_2 crystals [47]. In this work, a lower concentration of the hydrohalic acid (50 mM HX) was used at room temperature to avoid dissolution during the first chemical conversion step. A color change of the original PbO_2 film (orange-red) to the corresponding lead halide, PbI_2 (yellow), $PbBr_2$ (white) or $PbCl_2$ (white), was used to determine total conversion time. Porous films with high surface coverage were obtained in 6 min for PbI_2 using 50 mM HI and in 40 min for $PbCl_2$ using 50 mM HCl. The use of 50 mM HBr required a longer time of 4 h for the chemical conversion of PbO_2 to $PbBr_2$. The electrodeposited PbO_2 layer (Fig. 3.1a) is composed of submicron agglomerates of PbO_2 grains that are converted to PbX_2 films with distinctly different morphologies following the first chemical conversion step. For example, PbI_2 (Fig. 3.1b), adopts the crystal habit of its hexagonal crystal structure forming two-dimensional platelets that are oriented perpendicular to the underlying FTO substrate. The $PbBr_2$ film (Fig. 3.1c) presents some preferential growth in one direction, however it is less pronounced and may be affected by the longer conversion time required, which could also lead to its dissolution. On the other hand, $PbCl_2$ (Fig. 3.1d) forms a needle-like structure that is attributed to preferential growth in one direction that can occur in the presence of low concentrations of HCl [133].

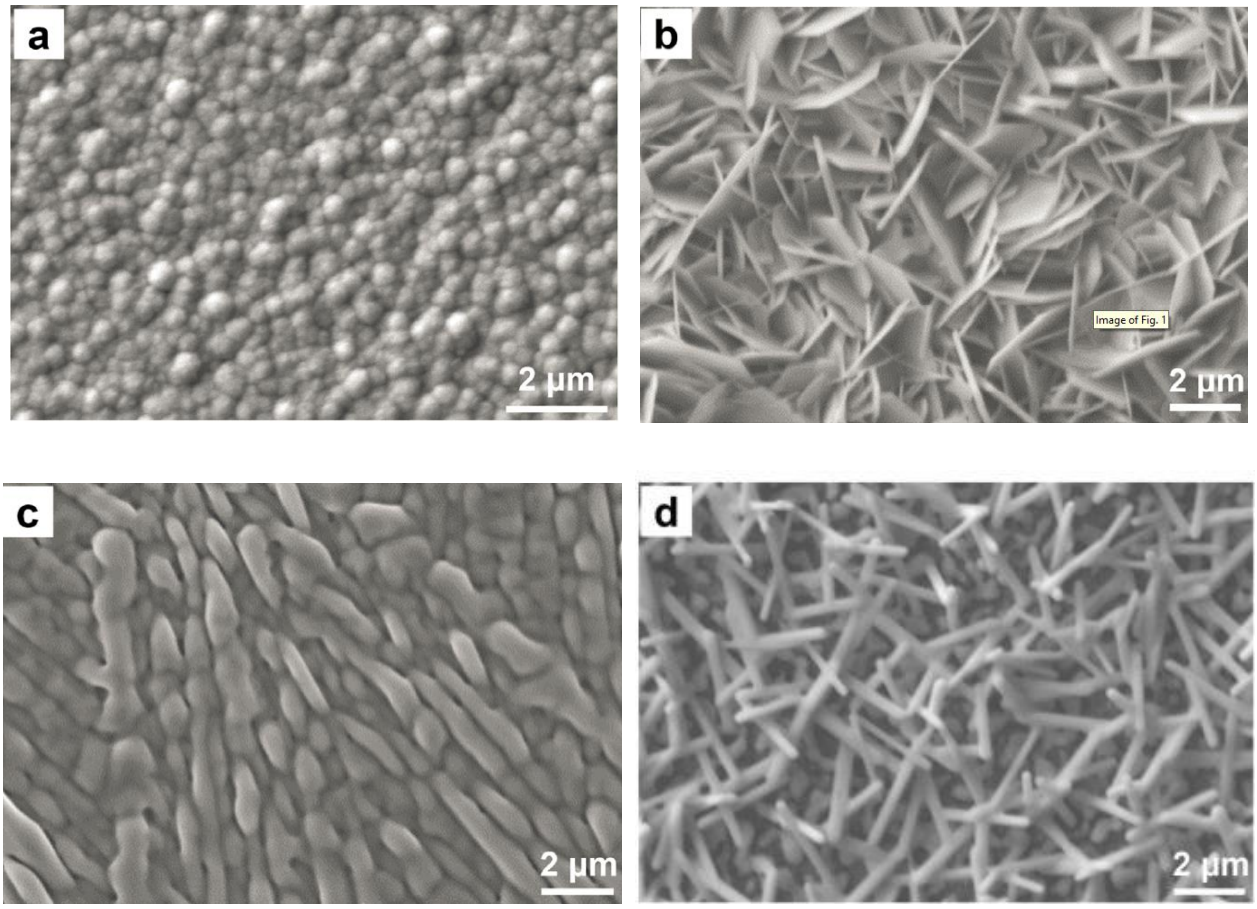

Figure 3.1 SEM images of (a) electrodeposited PbO_2 and chemically converted lead halide films (b) PbI_2, (c) $PbBr_2$ and (d) $PbCl_2$ on a FTO substrate.

The second chemical conversion step was carried out in methanol containing 20 mM CsX (X represents the halide) for 60 min to form the corresponding lead halide perovskite $CsPbX_3$. The concentration of CsX used during the second chemical conversion step was 20 mM due to its limited solubility in methanol. Following chemical conversion, the substrates were annealed at 100 ◦C for 10 min. A needle-like structure is observed for $CsPbI_3$ (Fig. 3.2a) due to the formation of one-dimensional chains of Pb-I octahedra, which is characteristic of the non-perovskite δ-$CsPbI_3$ [134]. In this work, it was not possible to obtain the γ-$CsPbI_3$ perovskite, which exhibits ideal physical properties for photovoltaic applications. Instead, the non-perovskite δ-$CsPbI_3$, which is thermodynamically stable at room temperature, was formed. Both $CsPbBr_3$ (Fig. 3.2b) and $CsPbCl_3$ (Fig. 3.2c) showed a cubic morphology consistent with the perovskite structure of these materials. The crystal structure of each film was acquired by X-ray diffraction (XRD) following each chemical conversion step. Fig. 3.3 shows the XRD patterns for each lead halide film along with the powder diffraction file (PDF) for PbI_2 (PDF No.: 00-073-1752), $PbBr_2$ (PDF No.:

01-085-1089) and $PbCl_2$ (PDF No.: 01-074-1803). The crystal structures of the lead halide films were indexed to the hexagonal polymorph for PbI_2 and orthorhombic polymorph for $PbBr_2$ and $PbCl_2$. Also presented in Fig. 3.3 are the XRD patterns for each $CsPbX_3$ film, which are indexed to the orthorhombic polymorph for $CsPbI_3$ (PDF No.: 00-074-1970) and $CsPbBr_3$ (PDF No.: 01-072-7929), and cubic polymorph for $CsPbCl_3$ (PDF No.: 00-018-0366).

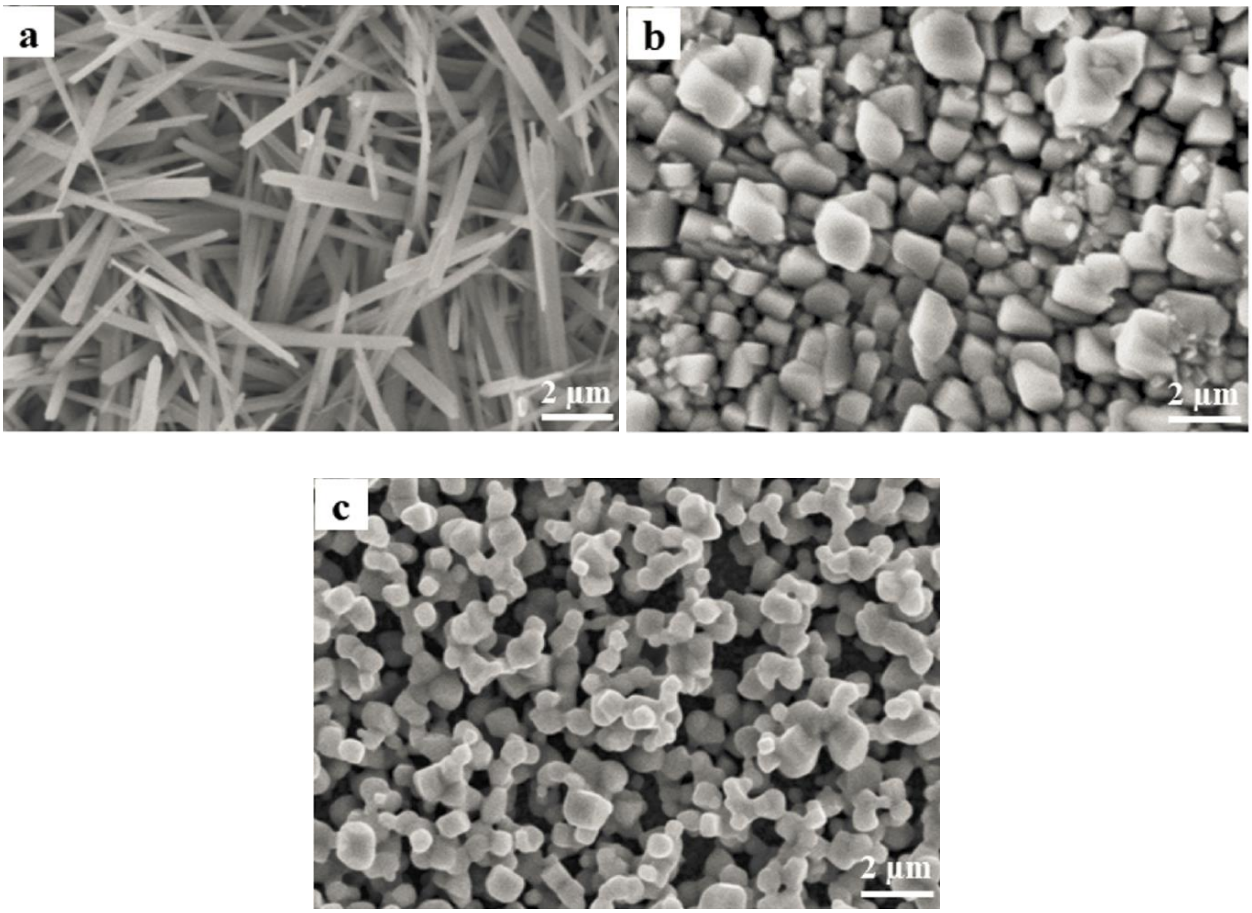

Figure 3.2 SEM images of (a) $CsPbI_3$, (b) $CsPbBr_3$ and (c) $CsPbCl_3$ thin films following chemical conversion of the corresponding lead halide on a FTO substrate.

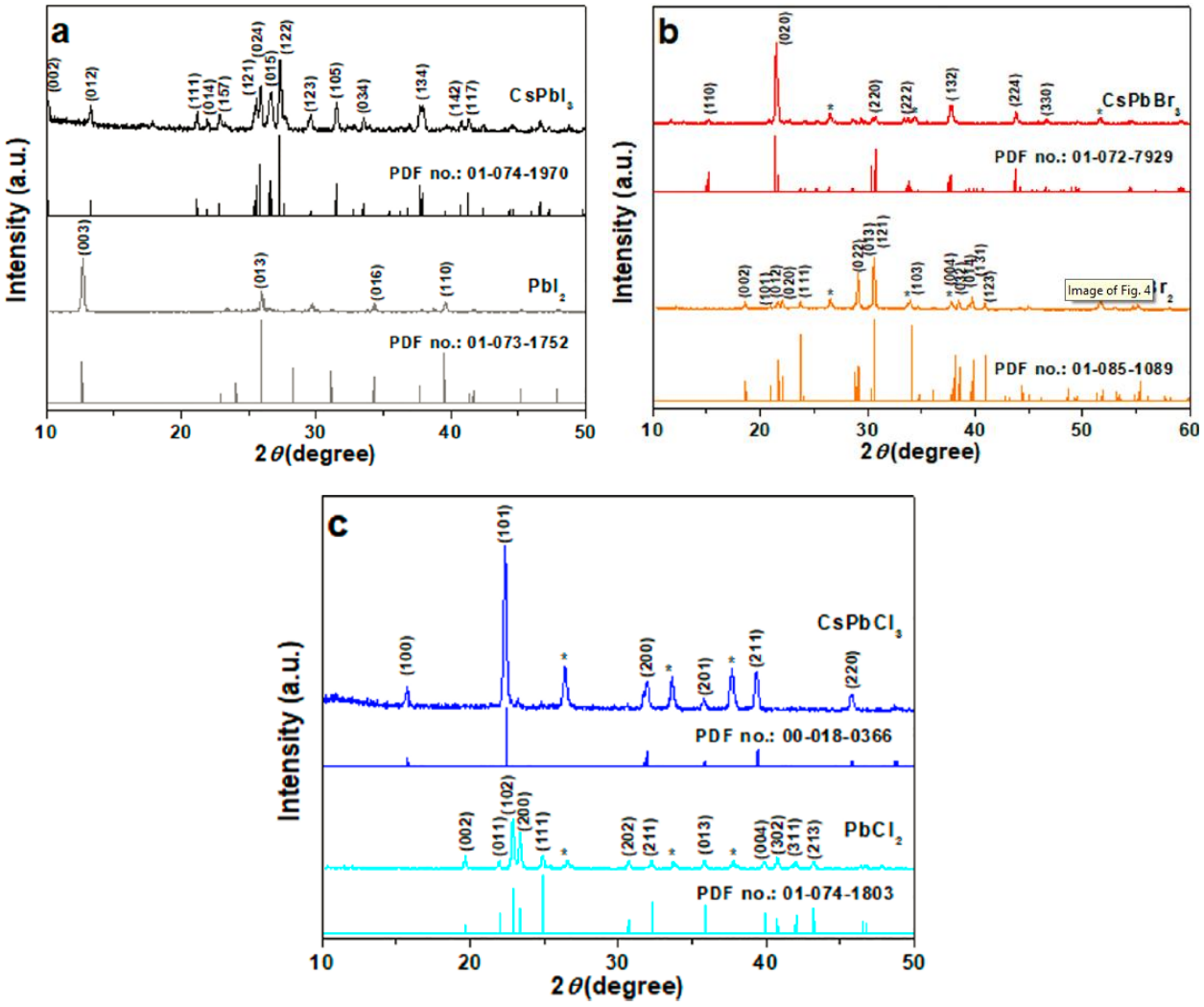

Figure 3.3 XRD patterns of (a) PbI_2 and $CsPbI_3$, (b) $PbBr_2$ and $CsPbBr_3$ and (c) $PbCl_2$ and $CsPbCl_3$ films. Asterisks represent the FTO substrate.

A combination of absorbance and voltammetric measurements were used to determine the optical bandgap and electrochemical stability window of the electrodeposited perovskites. Substitution of Br with Cl leads to an increase in the optical bandgap of the cesium lead halide perovskites [135]. The optical bandgap (E_g) of $CsPbBr_3$ (2.30 eV) and $CsPbCl_3$ (2.93 eV) was determined from a Tauc plot of the absorbance data (Fig. 3.4a) and the measured values are consistent with reported values for $CsPbX_3$ perovskites prepared via other methods [136-139]. Recently, linear sweep voltammetry (LSV) has been used to estimate the frontier energy levels as well as the onset of perovskite corrosion [74, 140]. Linear sweep voltammetry was carried out in dichloromethane (100 mM $TBAPF_6$) under an Ar atmosphere. Fig. 3.4b and 3.4c present LSVs of $CsPbBr_3$ and $CsPbCl_3$ films scanned in an anodic or a cathodic direction starting from the open-

circuit potential. A new film was used for the anodic and cathodic scan as the anodic and cathodic currents are attributed to irreversible oxidation and reduction processes, respectively. For the anodic scan of $CsPbBr_3$, two oxidation waves were observed, beginning at 0.50 V (vs. Ag-wire quasi-reference electrode) and at 1.10 V (vs. Ag wire quasi-reference electrode). For $CsPbBr_3$ films scanned in the cathodic direction, a single reduction wave was observed, beginning at -1.20 V (vs. Ag wire quasi-reference electrode). The electrochemical window of approximately 1.70 V is smaller than the optical bandgap of 2.30 eV, indicating that corrosion processes are likely occurring. Samu et al. [74] have recently carried out a detailed analysis of the surface chemistry of $CsPbBr_3$ under electrochemical control in dichloromethane and have proposed that the anodic and cathodic currents are due to the electrochemical corrosion of $CsPbBr_3$ through the following electrochemical reactions:

$$\text{Oxidation: } CsPbBr_3 \rightarrow PbBr_2 + Cs+ + 1/2Br_2 + e^- \quad (3.1)$$

$$PbBr_2 \rightarrow Pb^{2+} + Br_2 + 2e^- \quad (3.2)$$

$$\text{Reduction: } CsPbBr_3 + 2e^- \rightarrow Pb + Cs^+ + 3Br^- \quad (3.3)$$

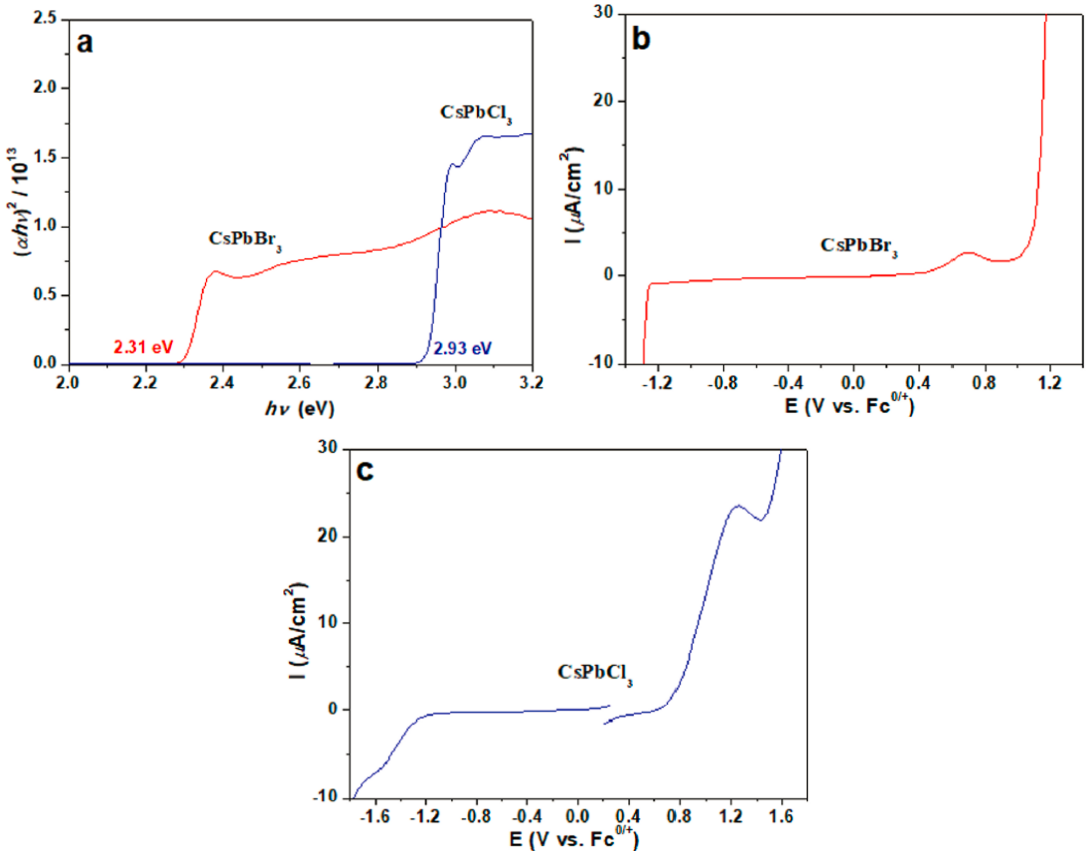

Figure 3. 4 (a) Tauc plot of $CsPbBr_3$ and $CsPbCl_3$. Linear sweep voltammograms of (b) $CsPbBr_3$ and (c) $CsPbCl_3$ in 0.1 M $TBAPF_6$ using a Pt counter electrode and Ag wire quasi-reference electrode. The scan rate was 20 mV s^{-1}.

The anodic LSV of $CsPbCl_3$ (Fig. 3.4c) also showed two oxidation waves, beginning at 0.75 V (vs. Ag wire quasi-reference electrode), which were anodically shifted relative to $CsPbBr_3$, while the onset for the reduction wave was the same at -1.20 V (vs. Ag wire quasi-reference electrode). The electrochemical window for $CsPbCl_3$ was 1.95 V and is smaller than the optical bandgap of 2.93 eV, which suggests that the anodic and cathodic currents are also related to corrosion processes. The widening of the electrochemical window of $CsPbCl_3$ by 0.25 V relative to $CsPbBr_3$ demonstrates an improvement in the corrosion resistance of chloride-based perovskites, which could assist in improving the long-term stability of lead halide perovskite materials and devices.

3.4. Conclusions

In this work, it was demonstrated, for the first time, that electrodeposited PbO_2 could be chemically converted to $PbBr_2$ and $PbCl_2$ to enable the fabrication of the all-inorganic perovskites $CsPbBr_3$ and $CsPbCl_3$. The perovskite thin films are grown directly on a conducting FTO substrate which can enable the preparation of large area thin-film devices for a variety of applications. For example, through optimization of the current density and electrochemical cell bath geometry, electrodeposited PbO_2 was recently used to create $MAPbI_3$ perovskite thin films with a surface area of 10 cm^2 [77]. In addition to the enhanced thermal and moisture stability of cesium lead halide perovskites, it was demonstrated here that the wide bandgap $CsPbCl_3$ perovskite exhibited a larger corrosion resistance than $CsPbBr_3$. This may explain, in part, the role of chloride in enhancing the stability of perovskite solar cells as was recently observed for an electrodeposited hybrid-organic $MAPbBr_3$ solar cell containing chloride [141]. It should also be noted that the two-step methodology presented here could also be used for the fabrication of hybrid-organic lead halide perovskite materials, where either $PbBr_2$ or $PbCl_2$ are required for their fabrication. Beyond photovoltaic devices, wide bandgap cesium lead halide perovskites are finding increasing applications as photoelectrodes, light emitting diodes and photodetectors where electrodeposition can be a valuable approach for their fabrication.

CHAPTER 4

Comparison of Two-Step and One-Step Chemical Conversion for the Electrodeposition of Hybrid Organic-Inorganic Lead Halide Perovskites

Abstract

The rise of perovskites has ignited a wave of excitement in materials physics and chemistry due to their prominent photovoltaic properties and easy synthesis. The commonly used spin-coating and vacuum/vapor-assisted deposition techniques produce perovskite devices with high efficiency exceeding 20% in the laboratory but suffer from their suitability for large-scale photovoltaic applications at low cost. We address this limitation by employing an electrochemical/chemical route applicable to large substrate areas in ambient atmosphere. Up to now, no comparative study between two-step and one-step chemical conversion has been carried out. Here we studied the crystal structure and film morphology of $MAPbX_3$ perovskite obtained using electrodeposition combined with one-step or two-step chemical conversion. In this work, lead dioxide (PbO_2) was electrodeposited and subsequently converted *in situ* to the organic-inorganic hybrid perovskites, methylammonium lead halide ($MAPbX_3$, X=Cl, Br, I), by using a solution-based two-step chemical conversion. The as-prepared $MAPbX_3$ films showed a stable output of cathodic photocurrent in a liquid junction electrochemical cell using benzoquinone (BQ/BQ^-) as a redox mediator. In addition, the direct *in situ* conversion of PbO_2 to $MAPbX_3$ using a solution-based one-step chemical conversion was also achieved, and the as-formed $MAPbX_3$ film exhibited larger grain size and photocurrent. As inherently scalable and low-cost techniques, electrodeposition combined with chemical conversion provides a general route toward hybrid perovskites, enabling the tunability of optoelectronic structure and film morphology of $MAPbX_3$ through managing chemical composition and conversion process. This work demonstrates a competitive solution fabrication process for the commercialization of perovskites, which is expected to be a template method for the fabrication of perovskites to expand their optoelectronic applications such as in photovoltaics and photoelectrocatalysis.

Keywords**:** perovskites, electrodepositon, chemical conversion, solar cells, photovoltaics, photoelectrocatalysis.

4.1 Introduction

Within the last 65 years, solar cells (SCs) have emerged to provide large amounts of clean and renewable energy, and currently contribute more than 1% to worldwide electricity generation [142]. It is estimated that photovoltaics could provide over 20% of the world's energy needs by 2050 [143]. Although silicon solar cells (SSCs) with a maximum efficiency of 27% in laboratory account for *ca.* 90% of the photovoltaic market share, the disadvantage of silicon is high cost because crystalline silicon has to be very pure to make efficient solar cells [142]. Among the cheap alternatives to crystalline silicon, perovskites are a rising star due to their easy processing, broad absorption spectrum and exceptional efficiency exceeding 23% in the laboratory [144-147]. Different from silicon process requiring extraordinary purity and high temperature, perovskites are easy to prepare using wet chemistry involving facile solvent and vapor deposition. Another interesting feature of perovskites is their tunable chemical composition and crystal structure, offering a wide variety of choices in terms of perovskite design and fabrication. Such versatility allows easy tailoring of optoelectronic structure of perovskites for numerous applications in photovoltaics, LEDs, photodetectors, and more [11, 148, 149].

Perovskites are a wide-ranging family of materials sharing a crystal structure of ABX_3. In this structure, monovalent cation A and bivalent metal cation B coordinate with 12 and 6 X anions to construct cuboctahedral and octahedral geometries, respectively (Figure 4.1). The most successful perovskites are variations on methylammonium lead halide perovskite (LHP), $MAPbX_3$ ($A = MA^+$, $B = Pb^{2+}$, $X = Cl^-$, Br^-, I^-). As a photovoltaic material LHP exhibit several key properties for optimal solar energy conversion such as small bandgap (E_g), strong absorption in the visible region, large photoexcited charge carrier diffusion lengths and long excited state lifetimes [150-153]. However, the majority of reported efficiencies are based on small active-area perovskites (~0.1 cm^2) [154]. Another challenge is the aspect of stability of perovskites [155, 156], which limits their widescale use. Therefore, the development of protocols to improve the scalability and stability of perovskites is of paramount importance.

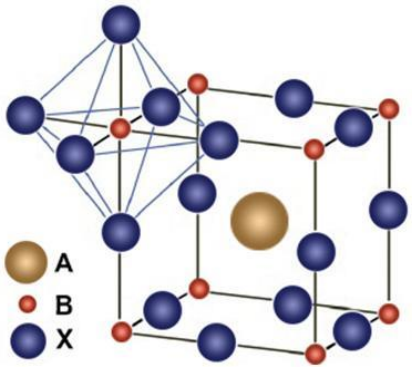

Figure 4.1 Schematic ABX_3 perovskite structure (adapted from Fabio G-S., 2017).

Spin-coating is the most commonly used solution method in the preparation of perovskite thin films due to its operational simplicity and high efficiency output, but it usually needs to be carried out in a N_2-filled glove-box and wastes a lot of perovskite material. Vacuum/vapor-assisted deposition are other methods which could lead to high-efficiency perovskite thin films, however it can also increase the total cost due to the high complexity of this method [157]. Recently Yang *et al.* reported for the first time a solution process based on PbO_2 electrodeposition and sequential two-step chemical conversion process to prepare $MAPbI_3$ perovskite thin film scaling up to 4 cm^2, which demonstrated a high PCE exceeding 10% [47]. Soon after, Switzer *et al.* converted electrodeposited PbO_2 to $MAPbI_3$ on an Au substrate using one-step chemical conversion [126]. However, the authors did not report on any photovoltaic applications of the as-prepared materials. A handful of other reports on the electrodeposition of LHP have appeared, all of which have focused on the preparation of the iodide-based organic-inorganic hybrid perovskite $MAPbI_3$. Another interesting application of LHPs are as a light absorber for photoelectrocatalytic applications, either coupled with an electrolyzer or in a liquid junction cell [158]. However, intrinsic limitations of $MAPbI_3$ perovskites such as instability in an ambient environment, non-optimal band edge potentials and a small E_g of 1.53 eV limit its photoelectrocatalytic applications for important reactions such as CO_2 reduction reaction. It is known that a given chemical reaction has a specific photoreduction or photooxidation potential, thus both band-edge-potentials and the E_g of the photoelectrocatalysts must satisfy specific thermodynamic conditions in order to be considered in photoelectrocatalytic applications. For CO_2 reduction to hydrocarbons at neutral pH and room temperature, the required maximum photoreduction potential is -0.67 V, which is smaller than the conduction-band-edge potential (E_{CB} = -0.52 V) of $MAPbI_3$ (Figure 4.2) [159]. Thus, perovskites with a lower E_{CB} are needed such as $MAPbBr_3$ (E_{CB} = -1.0 V, E_g = 2.22 eV) [160]. As well, a broad E_g of 1.75 eV is considered as the optimum value for perovskite/silicon tandem solar cells, which can be achieved by varying both cation and halides composition in LHP [161]. Therefore, there is an emerging interest in tuning the electronic structure (valence and conduction bands, E_g) as well as the stability of perovskites. Indeed, electrodeposition combined with chemical conversion is a scalable deposition method with low cost and high compatibility with complex shaped substrates [162-164]. Moreover, all solutions employed can be reused to reduce the pollution to the environment.

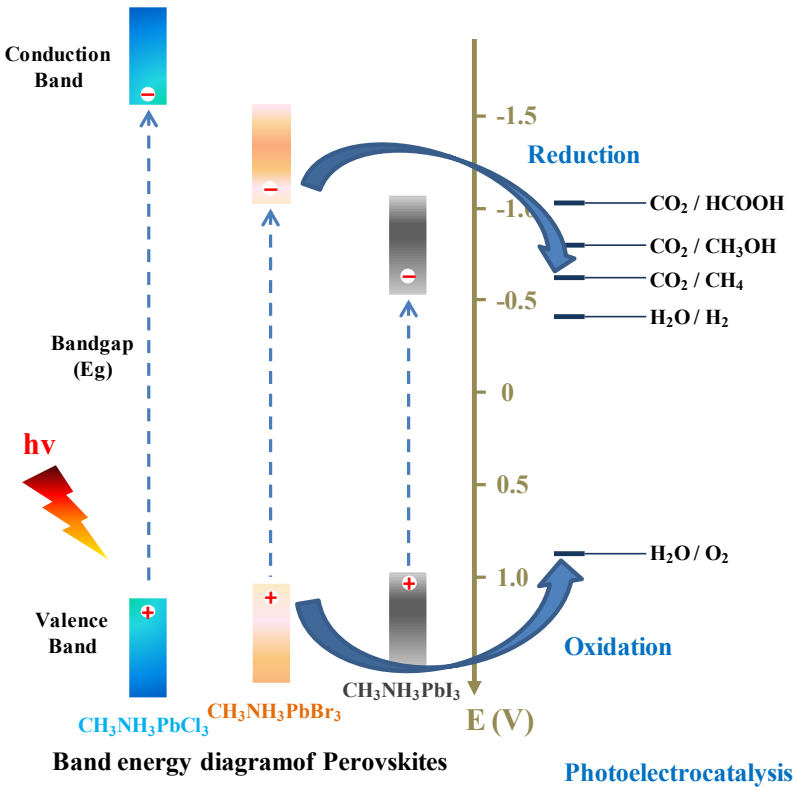

Figure 4.2 Bandgap of $MAPbX_3$ and energy levels of selected electrocatalytic reactions.

Herein, inspired by electrodeposition of the organic-inorganic hybrid $MAPbI_3$ perovskite, we combine electrodeposition with chemical conversion toward the preparation of the organic-inorganic hybrid $MAPbX_3$ family (X = I, Br, Cl). A comparative study of electrodeposition combined with two-step and one-step chemical conversion for the synthesis of a family of $MAPbX_3$ perovskite is reported, and their film morphology and photoresponse are evaluated. The present work demonstrates that electrodeposition combined with chemical conversion can be used as a general route for the preparation of a wide variety of organic-inorganic hybrid perovskites.

4.2 Materials and methods:

4.2.1 Materials:

Methanol, ethanol, isopropanol, acetone, hydrochloric acid, hydrobromic acid, hydriodic acid, methylammonium chloride, methylammonium bromide, methylammonium iodide, sodium acetate trihydrate and lead acetate trihydrate were purchased from Sigma-Aldrich. All chemicals were used as received without further purification. Fluorine-doped tin dioxide-coated glass

substrate (FTO) was purchased from Sigma-Aldrich. The water used through all experiments was purified through a Millipore system (18.2 MΩ).

4.2.2 Substrate preparation:

FTO slides were cut into small pieces, the edges were etched using zinc powder and 2 M hydrochloric acid. After that FTO was cleaned in acetone, methanol and water by ultrasonic washing with each for 20 min, followed by drying with compressed air.

4.2.3 PbO_2 Electrodeposition:

An aqueous solution containing 1.0 M sodium acetate and 0.1 M lead (II) acetate adjusted to pH 5.5 with concentrated acetic acid served as the electrodeposition bath. Electrodeposition was performed in a three-electrode cell using a multipotentiostat (Solartron 1470) under ambient atmosphere. A FTO slide acted as working electrode, platinum and Ag wire were used as counter electrode and reference electrode, respectively. Electrodeposition was carried out at a constant current density of 0.25 mA/cm^2 for a duration of 900 s.

4.2.4 Two-step chemical conversion from PbO_2 to $MAPbX_3$:

Conversion of the as-deposited PbO_2 to PbX_2 was conducted in a solution containing 0.05 M HX in ethanol, and the conversion time varied according to the hydrogen halide, as shown in Table 4.1. The subsequent conversion of PbX_2 to $MAPbX_3$ was carried out in a solution containing 0.05 M MAX in isopropanol. Finally, the as-prepared $MAPbX_3$ was annealed at 100 ^oC for 10 min.

Table 4.1 Conversion time for the chemical conversion of PbO_2 to PbX_2 and $MAPbX_3$

Conversion	**Conversion time**	**Color variation**
PbO_2 to $PbCl_2$	40 min	red to white
$PbCl_2$ to $MAPbCl_3$	5 days	white to white
PbO_2 to $PbBr_2$	4 hours	red to white
$PbBr_2$ to $MAPbBr_3$	2 hours	white to orange
PbO_2 to PbI_2	6 minutes	red to yellow
PbI_2 to $MAPbI_3$	3 minutes	yellow to black

4.2.5 One-step chemical conversion from PbO_2 to $MAPbX_3$:

Conversion of as-deposited PbO_2 to $MAPbX_3$ was conducted in a solution containing 0.05 M MAX in isopropanol, and the conversion time varied according to the methylammonium halide, as shown in Table 4.2. Finally, the as-prepared $MAPbX_3$ was annealed at 100 ^oC for 10 min.

Table 4.2 Conversion time for the chemical conversion of PbO_2 to $MAPbX_3$

Conversion	**Conversion time**	**Color variation**
PbO_2 to $MAPbCl_3$	7 days	red to white
PbO_2 to $MAPbBr_3$	15 hours	red to orange
PbO_2 to $MAPbI_3$	1 hour	red to black

4.2.6 Characterization:

The morphology of the perovskite films was studied by SEM using a Hitachi S-4700 SEM instrument. The UV-Vis absorption spectra were measured with a UV-VIS-NIR spectrophotometer (Lambda 750, Perkin-Elmer). The crystalline phase was identified by X-ray diffraction (XRD) using Bruker D8-Advance diffractometer with a Cu-K_α radiation.

4.2.7 Photoelectrochemical characterization:

Electrochemical measurements were carried out in an electrochemical cell using a potentiostat (BioLogic SP-300). Perovskite films on a FTO substrate functioned as the working electrode exposed to electrolyte, a Pt wire as the counter electrode, and an Ag wire as the quasi-reference electrode. A white light LED was used to provide an irradiance of 10 mW/cm^2 at the surface of the perovskite films. The supporting electrolyte was 0.05 M $TBAPF_6$ in CH_2Cl_2, and 2 mM *p*-benzoquinone (BQ/BQ^-) redox couple was used as the redox mediator. The scan rate was 10 mV/s, and the solution was degassed by argon bubbling during the measurement.

4.3 Results and discussion:

The mechanism of PbO_2 electrodeposition and chemical conversion to $MAPbX_3$ are presented in the following equations [47, 77, 126, 165, 166]:

PbO2 electrodeposition: $Pb^{2+} + 2H_2O \rightarrow PbO_2 + 4H^+ + 2e^-$ (4.1)

Two-step conversion: $PbO_2 + 4HX \rightarrow PbX_2 + X_2 + 2H_2O$ (4.2)

$PbX_2 + MAX \rightarrow MAPbX_3$ (4.3)

One-step conversion: $PbO_2 + 5MAX \rightarrow MAPbX_3 + 4MA + 2H_2O + X_2$ (4.4)

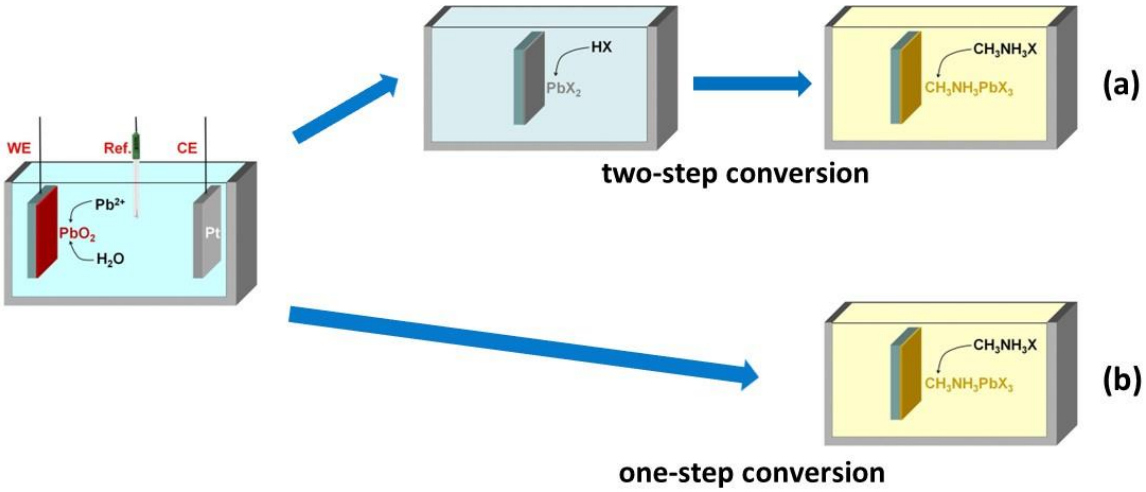

Figure 4.3 Schematic illustrating the solution processes of lead halide perovskites based on electrodeposition. PbO_2 film was electrodeposited followed by two-step chemical conversion to convert to $MAPbX_3$ (a), by one-step chemical conversion to convert to $MAPbX_3$ (b)

Figure 4.3a shows the solution process combining PbO_2 electrodeposition and sequential two-step conversion to $MAPbX_3$ in ambient atmosphere. PbO_2 was deposited galvanostatically on a FTO substrate, and the electrochemical oxidation of Pb^{2+} was controlled by an anodic current density of 0.25 mA/cm^2 using a three-electrode system (Equation 4.1). The low current density with a low growth rate led to a compact and uniform PbO_2 film with full coverage on a millimeter scale (Figure 4.4a), which is important to form uniform perovskite films through the next two-step chemical conversion. Figure 4.5a shows the XRD patterns of an as-deposited PbO_2 film, with the four diffraction peaks at 25.5°, 32.5°, 36.5° and 49.5° corresponding to (110), (101), (200) and (211) crystal planes of tetragonal *β*-PbO_2, respectively. The optical E_g of *β*-PbO_2 was determined to be 1.60 eV by UV-Vis absorption spectra followed by calculation using Tauc plot (Figure 4.6a, Figure 4.7a), which matches literature values [167]. The PbO_2 film was converted *in situ* to PbX_2 by chemical conversion in a HX ethanol solution. During the conversion, the reaction advanced from the edges and top of PbO_2 film toward the center and bottom, which involves PbO_2 reduction by the halide (Eq.4.2). The time period for chemical conversion of PbO_2 was

determined by the complete color change of the red PbO_2 films (Table.4.1). After the conversion, PbI_2 film displays a strong yellow coloration and an optical E_g of 2.4 eV, as the absorption onset blue shifts to 575 nm (Figure 4.6, Figure 4.7b). $PbCl_2$ and $PbBr_2$ films are white, and they barely have absorption in the visible region (Figure 4.6). XRD patterns of the converted PbX_2 films lack PbO_2 reflection peaks, and the new diffraction peaks are readily detected, which match well with that of PbX_2 (Figure 4.5a). The volume of PbO_2 grains may expand upon chemical conversion as PbX_2 is less dense than PbO_2 (Figure 4.4b-d) [77], e.g., 6.16 g/cm^3 for PbI_2 vs. 9.38 g/cm^3 for PbO_2. The as-prepared PbX_2 was converted to $MAPbX_3$ by interdiffusion reaction with MAX, followed by the thermal annealing at 100 ^oC for 10 min to improve the perovskite crystallization. After conversion to $MAPbX_3$, color evolution occurs depending on the original PbX_2 films, and the absorption spectrum of $MAPbX_3$ is in the visible region with the optical E_g shifting from 2.99 eV to 2.37 eV and 1.57 eV going from Cl to Br and I, respectively (Figure 4.6, Figure 4.7c-e). It is noted that it took 5 days to completely convert $PbCl_2$ to $MAPbCl_3$ without color variation (see Table 4.1), and the conversion process was monitored by XRD. Figure 4.5b shows the XRD patterns of the $MAPbX_3$ films, where a new set of diffraction peaks appear, with no lead halide detected. The characteristic diffraction peaks at 14.5^o, 24.8^o, 32.3^o are ascribed to the (110), (220), (114) crystal planes of tetragonal $MAPbI_3$, 15.4^o, 21.7^o, 30.7^o, 34.3^o are ascribed to the (100), (110) (200), (210) crystal planes of cubic $MAPbBr_3$, and 16.0^o, 22.5^o, 31.9^o, 35.7^o are ascribed to the (100), (110) (200), (210) crystal planes of cubic $MAPbCl_3$, respectively [168, 169]. $MAPbI_3$ exhibits a compact and uniform morphology with crystal grains ranging from 0.5 to 1 μm (Figure 4.4g). $MAPbBr_3$ presents a compact morphology with large grain size distribution ranging from sub-micrometer to several micrometers. $MAPbCl_3$ shows a compact morphology with irregular shaped grains of sub-micrometer size.

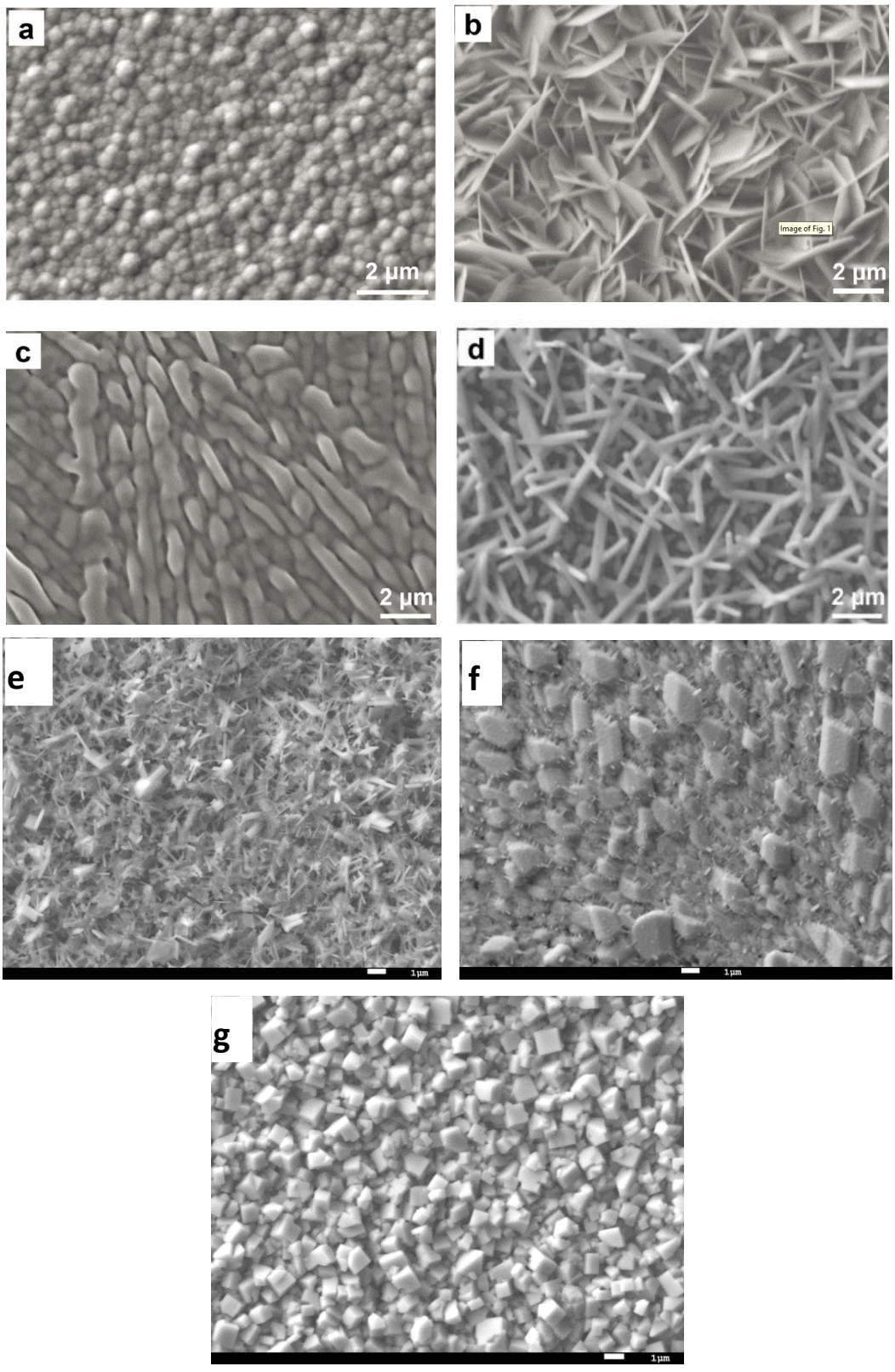

Figure 4.4 Top-view SEM images of PbO_2, PbX_2 and $MAPbX_3$ films. (a) PbO_2, (b) PbI_2, (c) $PbBr_2$, (d) $PbCl_2$, (e) $MAPbCl_3$, (f) $MAPbBr_3$, (g) $MAPbI_3$.

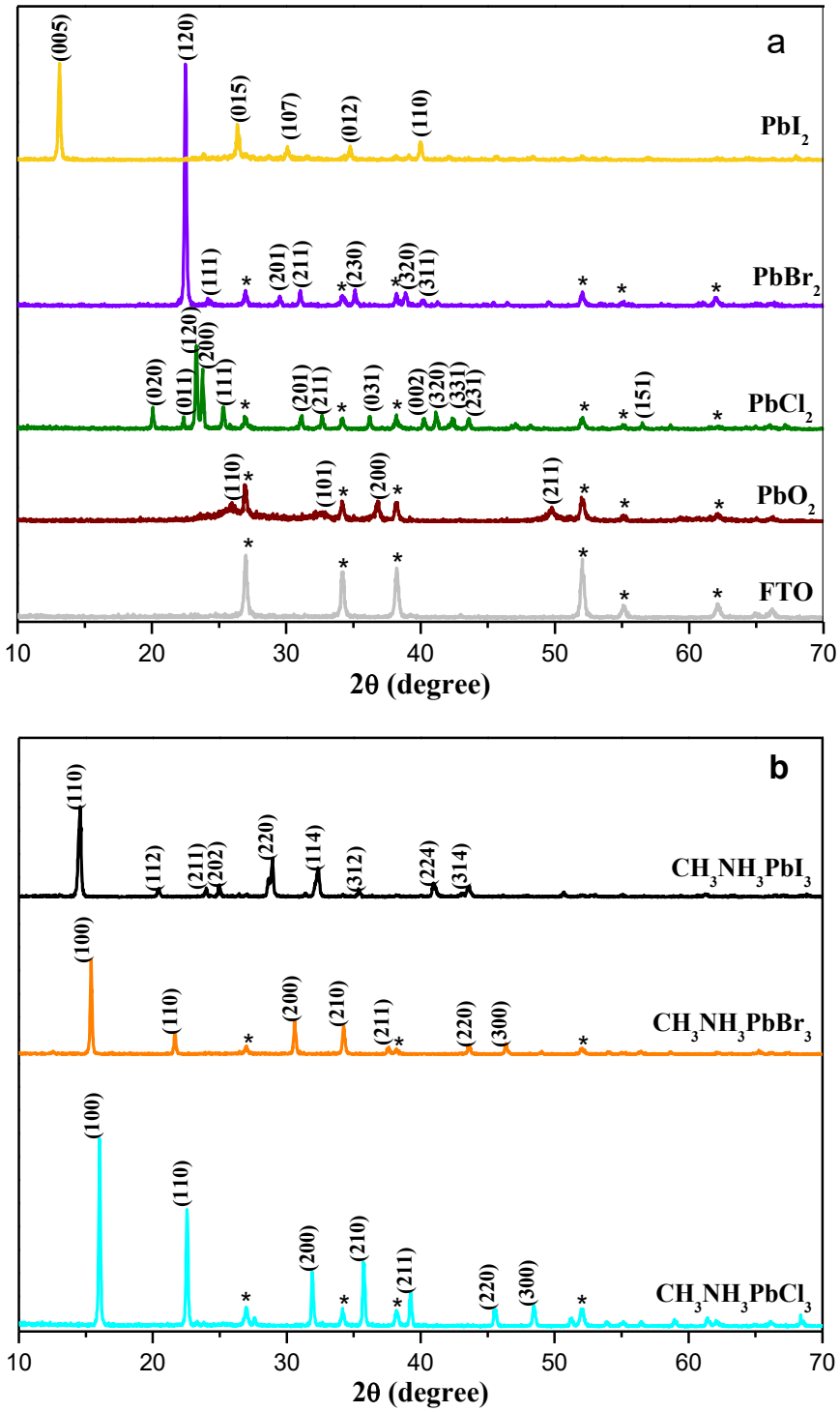

Figure 4.5 XRD patterns of PbO_2, PbX_2 (a) and $MAPbX_3$ (b), asterisks represent the FTO substrate.

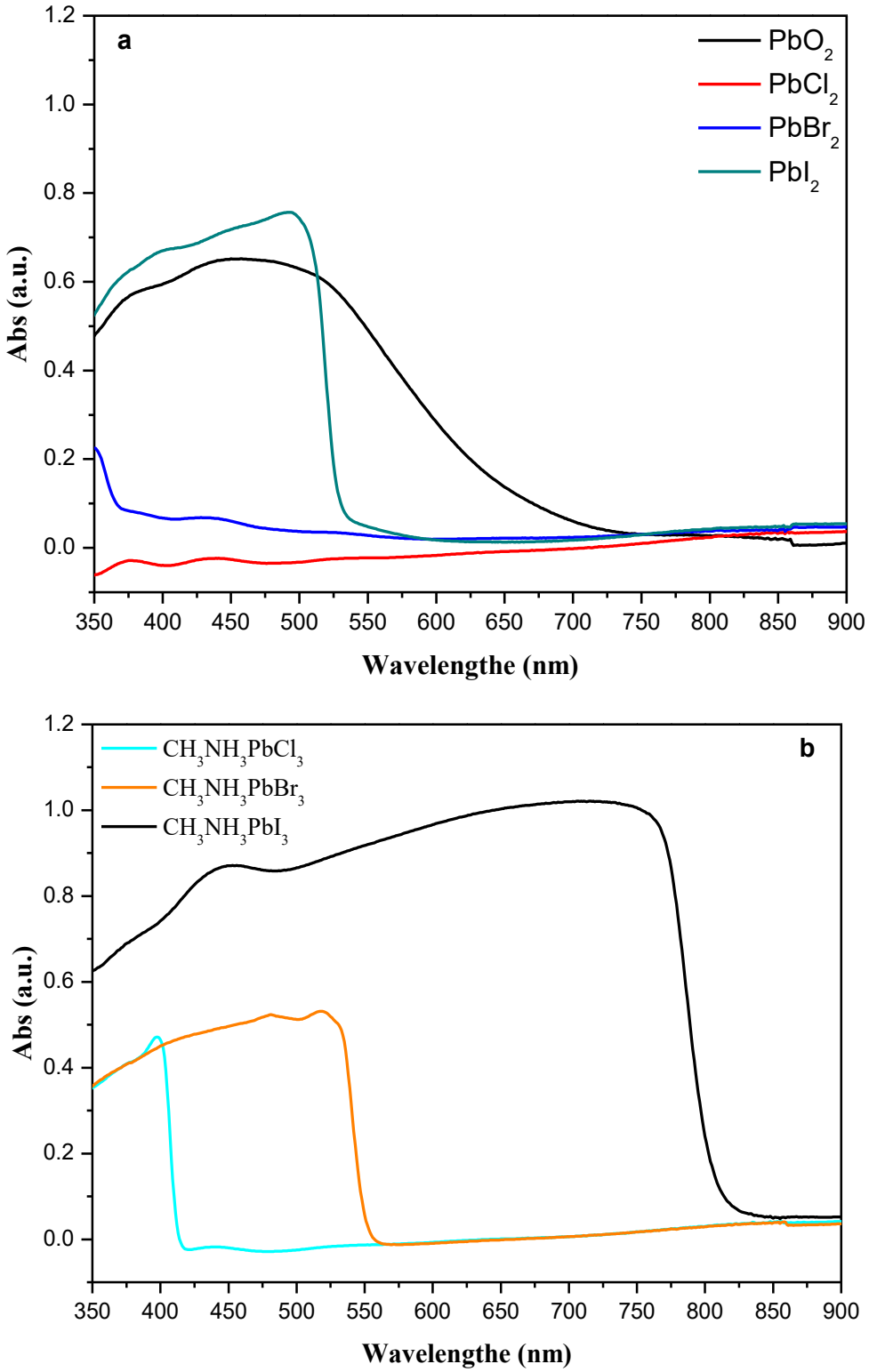

Figure 4.6 UV-Vis absorption spectra of PbO_2, PbX_2 (a) and $MAPbX_3$ (b) films.

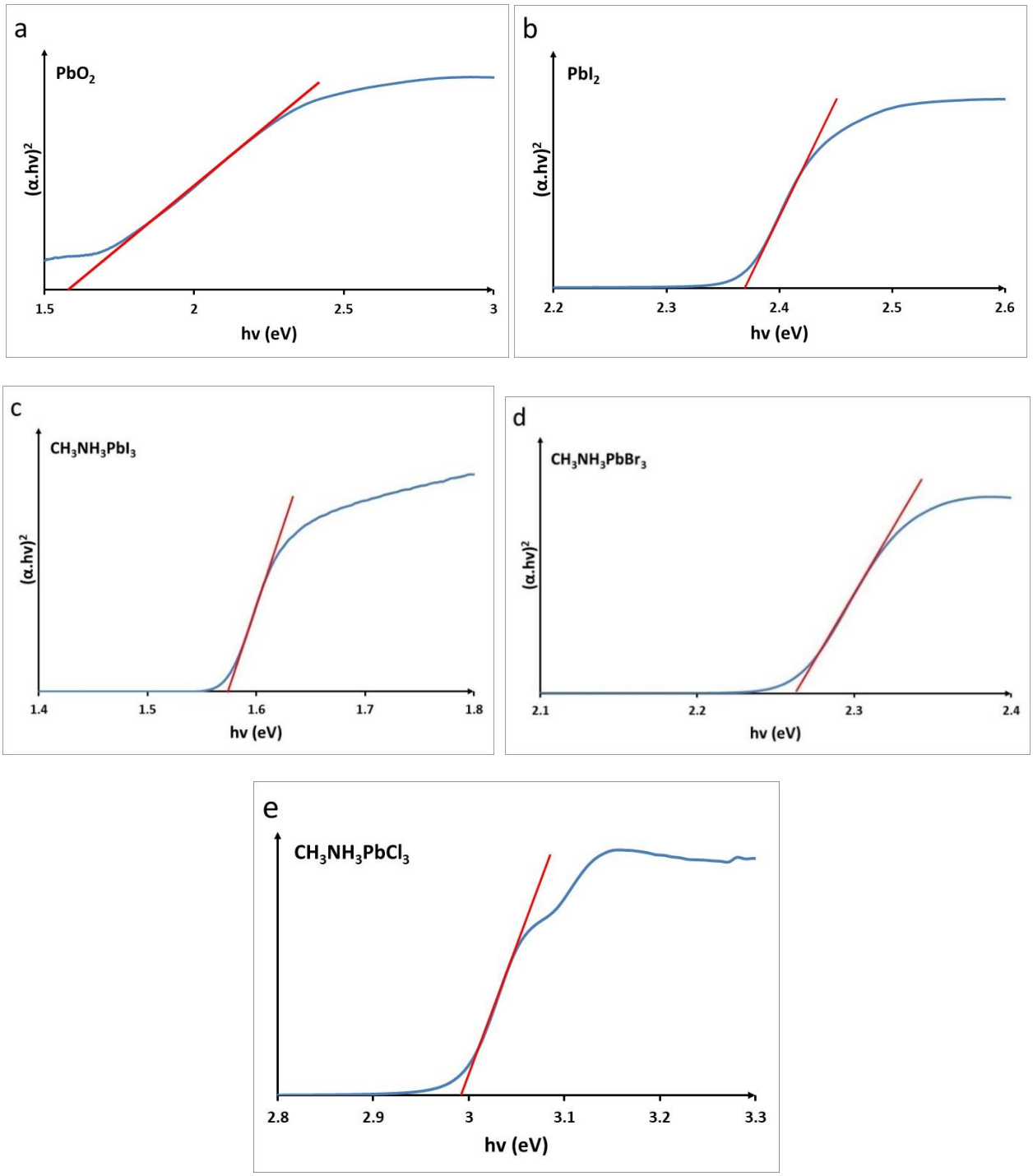

Figure 4.7 Tauc plot for the calculation of E_g of PbO_2(a), PbI_2(b), $MAPbX_3$ (c-e) films.

Depending on the solution techniques and chemical composition employed during the perovskite preparation, the morphology of the resulting perovskite films may vary significantly, which subsequently affect the efficiency and stability of perovskite devices. The direct *in situ*

conversion of PbO_2 to $MAPbX_3$ was also achieved by using one-step chemical conversion, as shown in Figure 3b. Both XRD patterns and optical E_g of $MAPbX_3$ are in good agreement with that obtained using two-step chemical conversion (Figure 4.8, Figure 4.9). Meanwhile, SEM images show improved morphology with a larger grain size (ca. 1 μm or larger) for one-step chemical conversion (Figure 4.10). Grain size is one of the key factors to optimize the performance of perovskite devices, and large grain size has contributed to high stability and efficiency perovskites due to the reduced charge recombination sites in perovskite film. This suggests that electrodeposition combined with one-step chemical conversion may lead to high-quality hybrid organic-inorganic perovskite film.

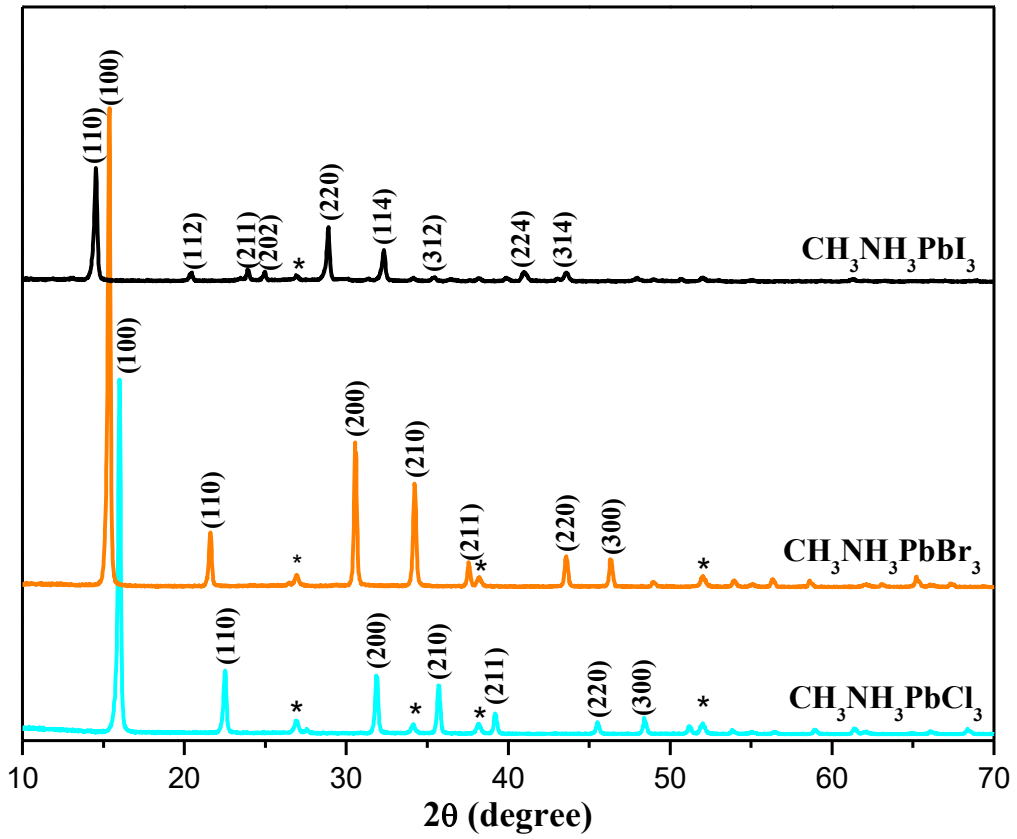

Figure 4.8 XRD patterns of $MAPbX_3$ obtained by PbO_2 electrodeposition combined with one-step chemical conversion, asterisks represent the FTO substrate.

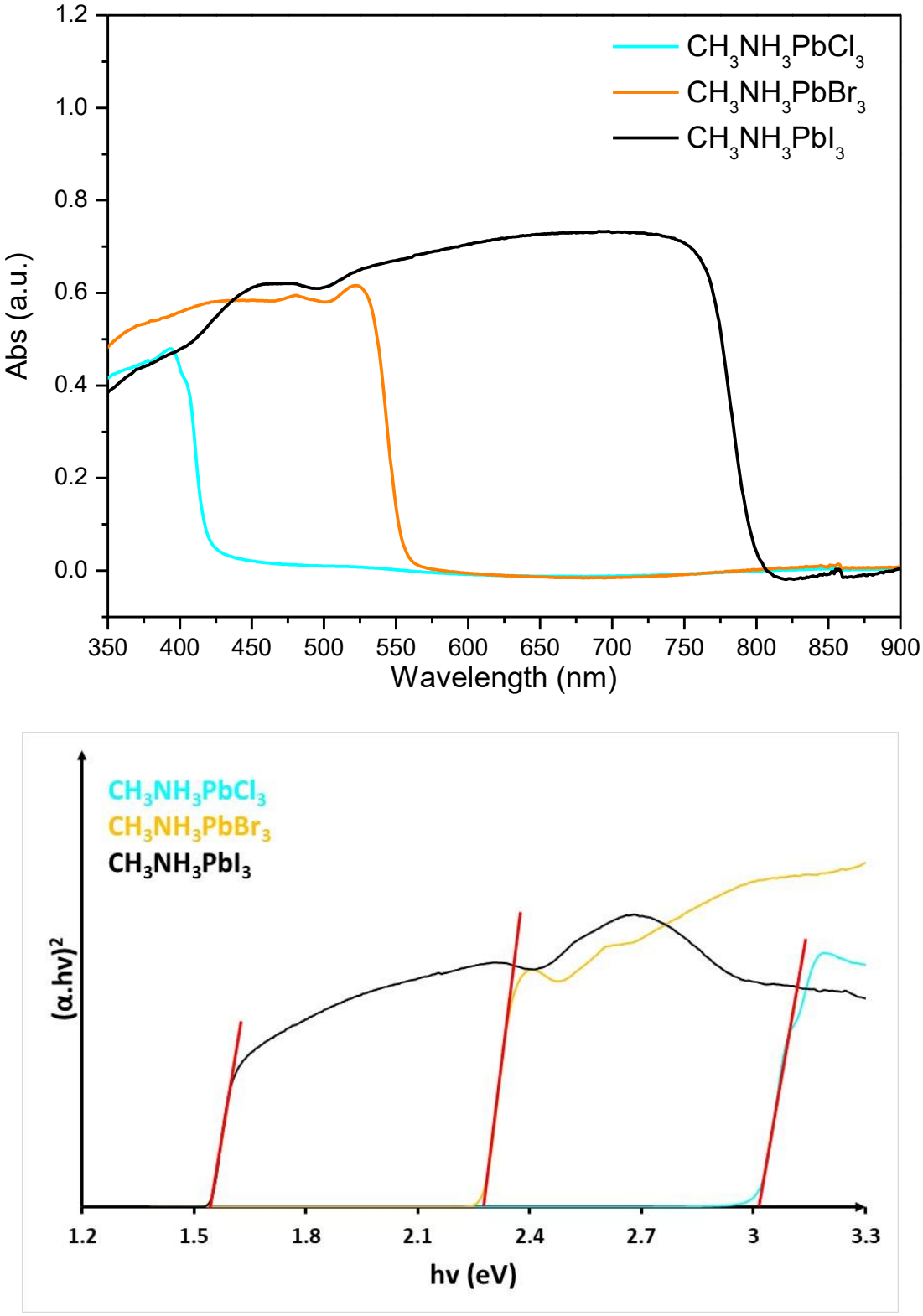

Figure 4.9 UV-Vis absorption (top) and Tauc plot (bottom) of $MAPbX_3$ films obtained by one-step chemical conversion.

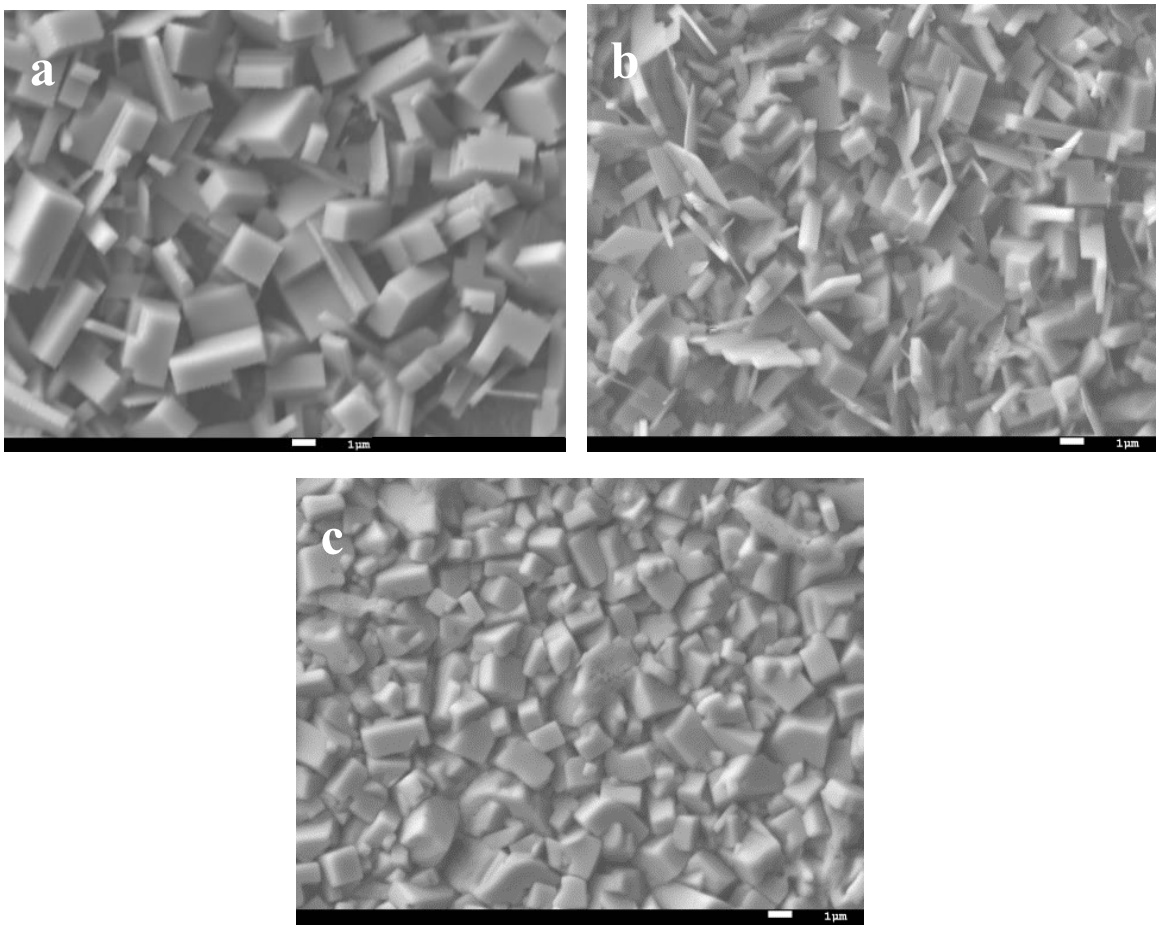

Figure 4.10 Top-view SEM images of $MAPbX_3$ film obtained by PbO_2 electrodeposition combined with one-step chemical conversion. a: $MAPbCl_3$, b: $MAPbBr_3$, c: $MAPbI_3$.

Even though one-step conversion showed advantages on the grain size and film uniformity, the conversion from PbO_2 to $MAPbX_3$ take much more time than that to PbX_2 then to $MAPbX_3$, as shown in Table 4.1 – 4.2. For example, it takes 1 h to convert PbO_2 to $MAPbI_3$, and the activation energy for this conversion was determined to be 38.3 KJ/mol [126]. On the other hand, the activation energy from PbO_2 to PbI_2 in acidic solution is 18.4 KJ/mol [170], which leads to a fast conversion in 6 minutes. For the second conversion from PbX_2 to $MAPbX_3$, the activation energy for vacancy-mediated ion migration increases from X = I to Br and to Cl due to the presence of water in the conversion bath [171], which results in a fast conversion from PbI_2 to $MAPbI_3$ in 3 minutes, and slower conversion from $PbCl_2$ to $MAPbCl_3$ in 5 days. Figure 4.11 shows the XRD pattern of $MAPbI_3$ films obtained through one-step and two-step conversion. $MAPbI_3$ showed a strong preferential orientation along the (110) plane, $MAPbCl_3$ and $MAPbBr_3$ had a strong preferential orientation along the (100) plane. Meanwhile, two-step $MAPbI_3$ showed orientation along the (112) plane similar to the one-step $MAPbI_3$. Two-step $MAPbCl_3$ and $MAPbBr_3$ had

preferred orientation along (110) plane over their one-step counterparts, as shown in Table 4.3. It has been reported that the crystallographic orientation does not govern the optoelectronic quality of $MAPbI_3$ thin films [172], which may also have an insignificant effect on $MAPbCl_3$ and $MAPbBr_3$ films for their optoelectronic applications.

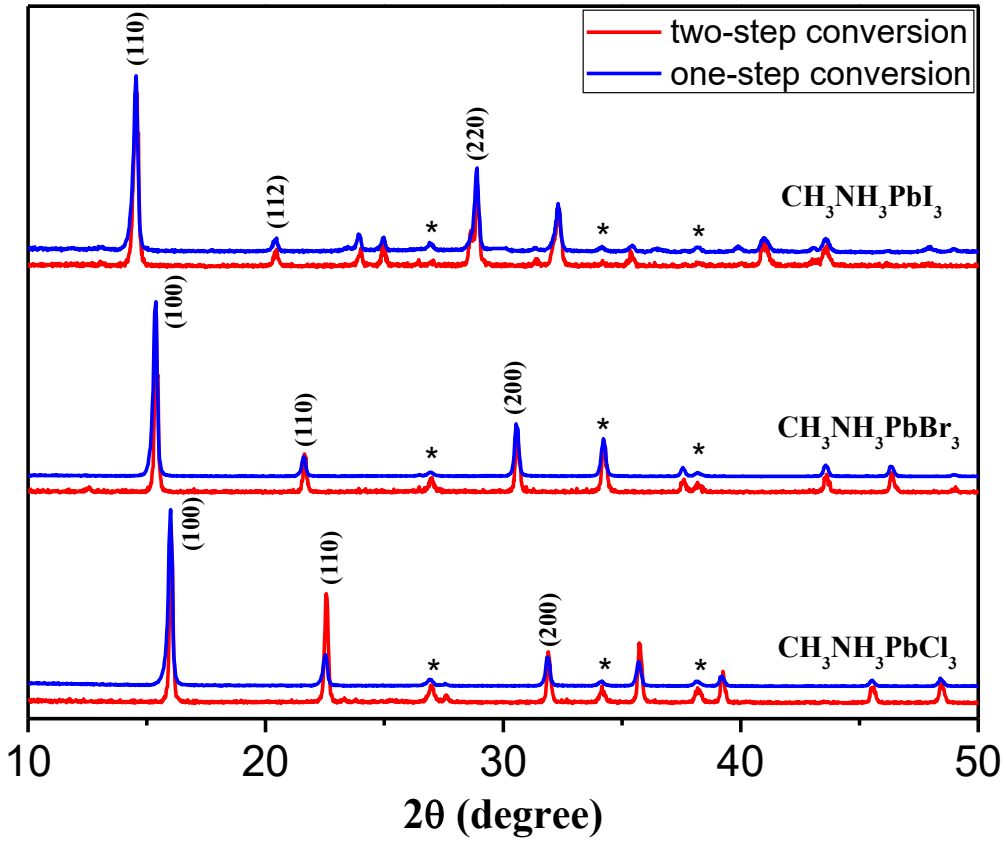

Figure 4.11 Normalized XRD patterns of $MAPbX_3$ films obtained through one-step and two-step conversion, asterisks represent the FTO substrate.

As shown in Table 4.3, the FWHM of 3 main diffraction peaks showed a bigger average crystal size for $MAPbCl_3$ film obtained through one-step conversion than that of two-step conversion, which was consistent with SEM. It has been demonstrated that perovskite films with larger crystal grain sizes (e.g., micron-size) are favorable for charge carrier transport [173].

Table 4.3 Normalized Intensity and full-width at half maximum (FWHM) of the densest diffraction peaks for $MAPbX_3$ films

$MAPbI_3$	two-step		one-step	
plane	intensity	FWHM	intensity	FWHM
(110)	100	0.24	100	0.21
(112)	20	0.17	6.5	0.16
(220)	43	0.18	47	0.2

$MAPbBr_3$	two-step		one-step	
plane	intensity	FWHM	intensity	FWHM
(100)	100	0.16	100	0.19
(110)	22.3	0.15	11	0.18
(200)	35	0.18	30	0.19

$MAPbCl_3$	two-step		one-step	
plane	intensity	FWHM	intensity	FWHM
(100)	100	0.15	100	0.19
(110)	62	0.18	17	0.2
(200)	28	0.16	15	0.2

In polycrystalline perovskite films, defects and impurities were found at GB and film surfaces. Non-radiative recombination at GBs and film surface severely limit perovskite device performance. It has been reported that large grains can efficiently reduce the influence of defective GBs by decreasing defects associated with the GB, leading to a significantly improved performance together with longer charge-carrier lifetimes [174]. In this study, the photoresponse of two-step and one-step $MAPbI_3$ perovskite films with different grain size was investigated in a photoelectrochemical cell, using linear sweep voltammetry (LSV) and BQ/BQ^- as redox mediator. To find the electrochemical satiability window for $MAPbI_3$, LSV measurements were measured for potentials between + 0.40 V and − 0.20 V vs. Ag/Ag^+ at a scan rate of 10 mV/s. Figure 4.12 shows voltammograms recorded for two-step $MAPbI_3$. The cathodic current in dark and under illumination increased with the applied potential sweeping toward − 0.20 V, without

showing oxidation or reduction peaks. The photocurrent under illumination was larger than the dark one, and was ca. 4 times higher at 0.0 V as compared in the dark. This enhancement in the current can be correlated with the energy levels of the WE, $MAPbI_3$/FTO, at the electrolyte interface, as shown in Figure 4.13. In the dark condition, electrons were injected into the WE when the potential was swept more negative, which were transferred to the electrode/electrolyte interface to reduce BQ in electrolyte resulting in the increase of the cathodic current. While under light illumination, e^- was excited from VB to CB of $MAPbI_3$, and holes (h^+) were generated at the low energy VB. On applying a bias potential to $MAPbI_3$/FTO electrode, both h^+ and e^- moved in opposite directions and electrons were transferred to the $MAPbI_3$/electrolyte interface to reduce BQ to generate a cathodic photocurrent, which increased with the applied potential being swept toward more negative values.

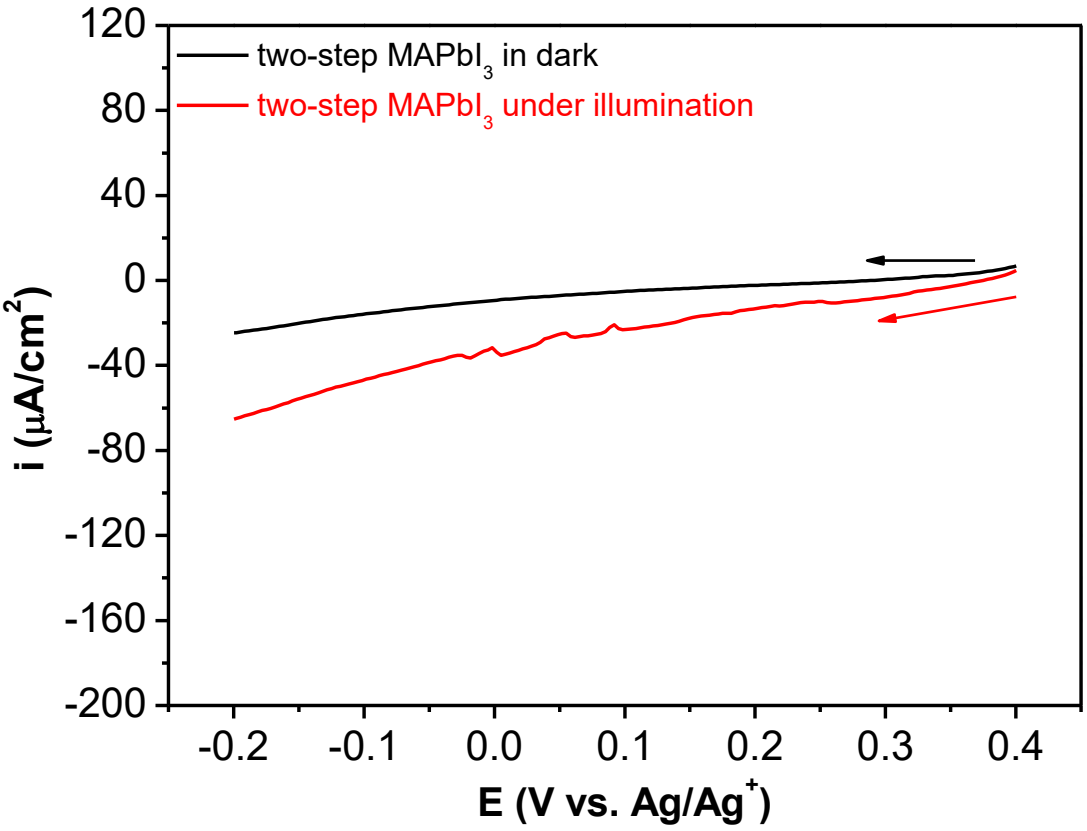

Figure 4.12 Photocurrent-potential curves of 2-step prepared $MAPbI_3$ in 0.05 M $TBAPF_6$ electrolyte at the scan rate of 10 mV/s.

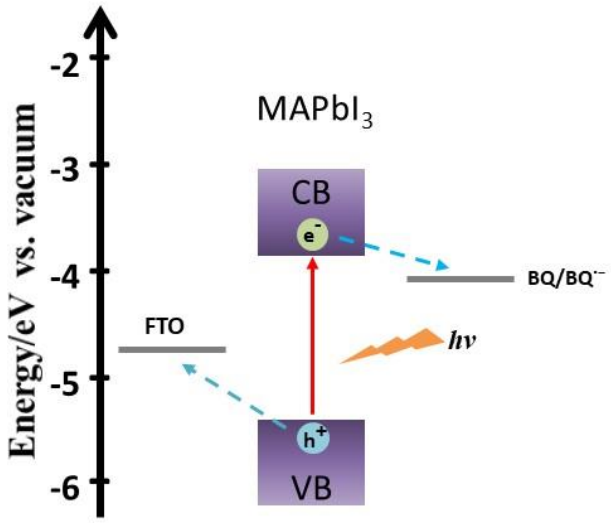

.

Figure 4.13 Schematic diagram of the energy levels at $MAPbI_3$/electrolyte interface. CB and VB denote the conduction band and valence band of $MAPbI_3$.

Compared with two-step $MAPbI_3$, one-step $MAPbI_3$, showed a large dark current and photocurrent as shown in Figure 4.14. The photocurrent under illumination gradually increased and was ca. 3 times higher at 0.0 V as compared in the dark. As mentioned above, the one-step conversion directly from PbO_2 to $MAPbI_3$ resulted in a film morphology with large grains, which can significantly improve the photovoltaic performance of perovskite device [174]. Meanwhile, one-step $MAPbI_3$ had a dominate (110)-preferred orientation (ca. 65%), higher than that for its two-step counterpart (ca. 61%). The (110) orientation has been reported to contribute to the superior PCE and stability for $MAPbI_3$ device [175]. To summarize, one-step $MAPbI_3$ showed larger grain size and photocurrent, which provides a useful method to obtain highly-oriented and efficient perovskites.

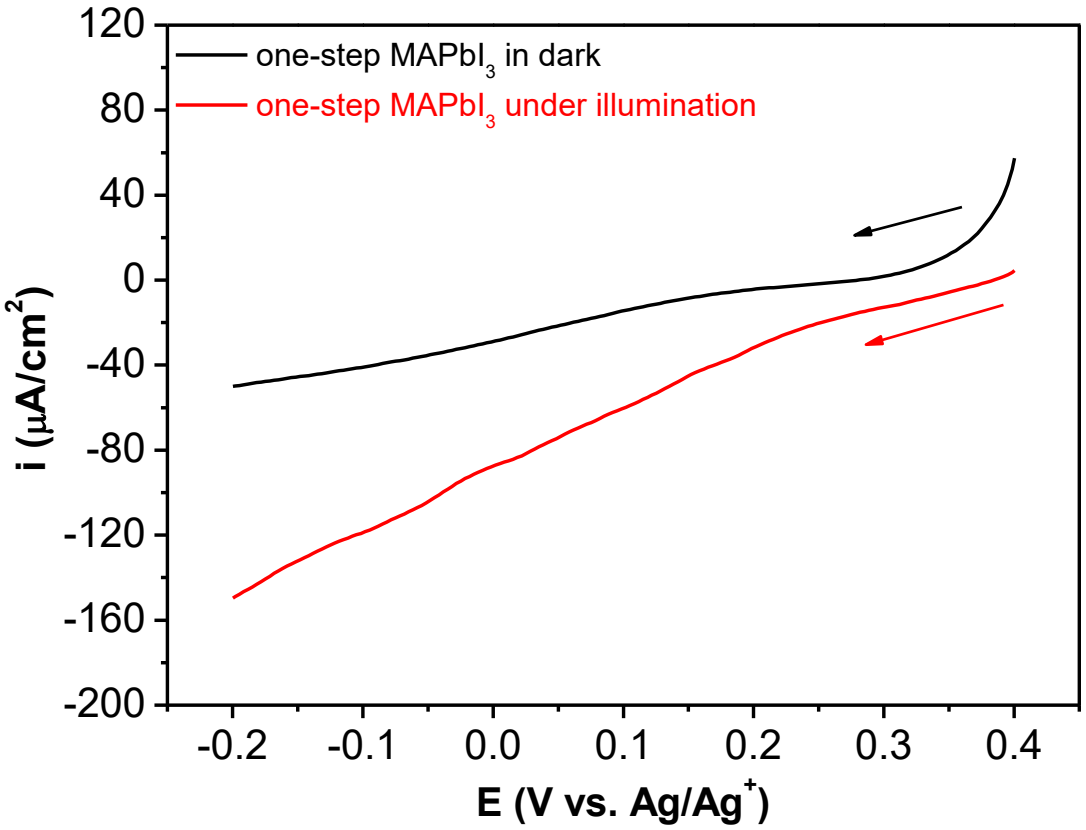

Figure 4.14 Photocurrent-potential curves of 1-step prepared $MAPbI_3$ in 0.05 M $TBAPF_6$ electrolyte at the scan rate of 10 mV/s.

Figure 4.15 shows LSV curves measured under light on/off cycles, for both two-step and one-step $MAPbI_3$ films with the onset at about 0.40 V vs. Ag/Ag^+. The photocurrent increased and decreased rapidly when the light was switched on and off, and there was no significant transient decay. A decay of photocurrent suggests a recombination of the photogenerated carriers and indicates that not all photogenerated e^- are transported to reduce BQ. We can conclude that the two-step and one-step $MAPbI_3$ prepared by ED were high-quality perovskites with minor defects at GB and film surfaces.

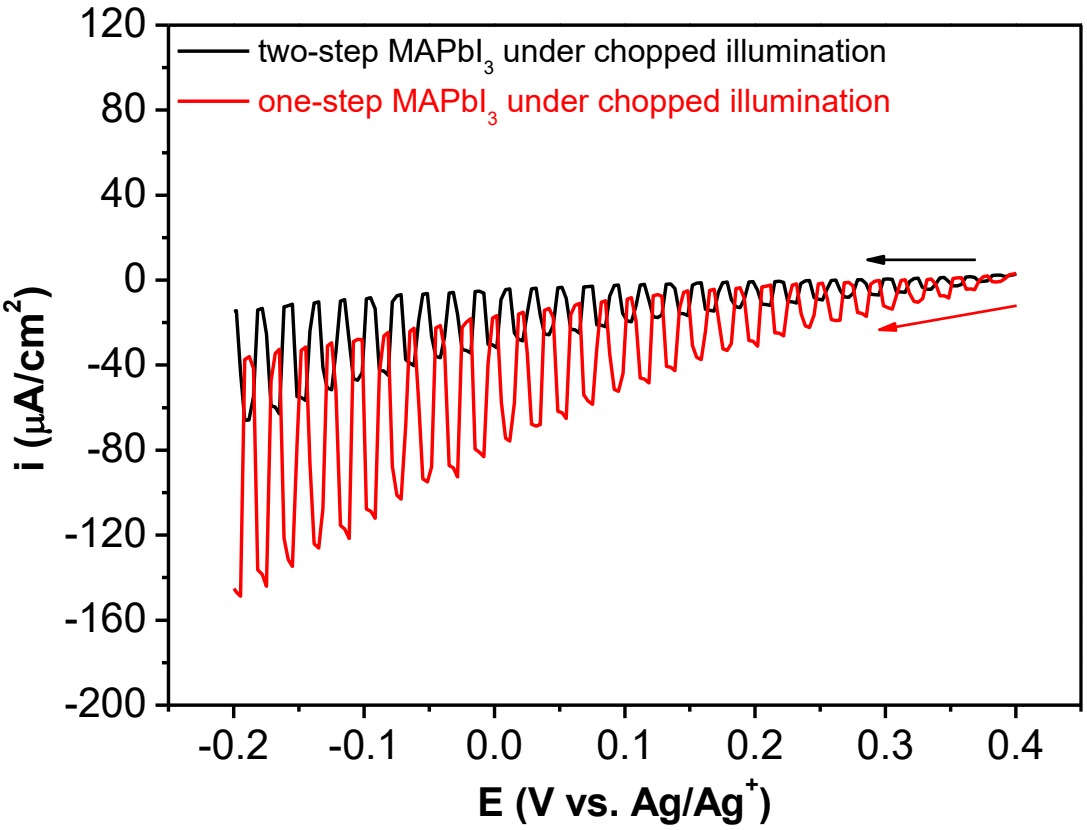

Figure 4. 15 Photocurrent-potential curves of $MAPbI_3$ in 0.05 M TBAPF6 electrolyte at the scan rate of 10 mV/s.

4.4. Conclusion

Herein, we reported PbO_2 electrodeposition combined with one-step and two-step chemical conversion as a general route toward hybrid $MAPbX_3$ perovskites in ambient atmosphere, and their crystal structure, film morphology and photoresponse were evaluated. $MAPbI_3$ perovskites prepared by electrodeposition combined with one-step chemical conversion shows larger grain sizes and photocurrents, which could be a more economical and effective route toward high-quality $MAPbX_3$ perovskite films. This scalable solution process provides a facile method to tune the optoelectronic properties of perovskites by managing the chemical composition and conversion process. All these works are expected to provide a strategy for the improvement of the optoelectronic properties of perovskites as a function of chemical, structural and morphological variations.

Chapter 5

Electrodeposition of inorganic cesium lead mixed-halide perovskites

Abstract

Inorganic cesium lead mixed-halide ($CsPb(XY)_3$, X, Y = I, Br, Cl) perovskites have recently attracted enormous interest for stable and efficient optoelectronic applications. While several techniques have been developed for the preparation of $CsPb(XY)_3$, there is still a need for a facile and scalable method to synthesize $CsPb(XY)_3$. Herein, starting from electrodeposited PbO_2, we developed a two-step solution deposition to synthesize a series of $CsPb(XY)_3$ films. Their crystal structure was determined by XRD to identify the perovskite structure of $CsPb(ICl)_3$, $CsPb(IBr)_3$ and $CsPb(ClBr)_3$. Further study indicates that $CsPb(ICl)_3$ and $CsPb(ClBr)_3$ adopted a cubic phase with an E_g of 2.92 eV and 2.39 eV, respectively, and $CsPb(IBr)_3$ an orthorhombic phase with E_g of 2.23 eV. Photoluminescence (PL) mapping showed a red-shift at grain boundaries (GB) due to phase segregation for $CsPb(IBr)_3$, but no emission shift was observed for $CsPb(ICl)_3$ or $CsPb(ClBr)_3$. Their photocurrent (Iph) response was also studied to evaluate the performance of the perovskite films in a liquid junction photoelectrochemical (PEC) cell. This work provides a facile and scalable approach towards the preparation of inorganic $CsPb(XY)_3$ mixed halide perovskites, and reveals their potential for optoelectronic applications using large area coating methods.

Keywords

Cesium lead mixed-halide, Electrodeposited PbO_2, Two-step solution deposition, Photoluminescence mapping, Grain boundaries, Inorganic perovskites.

5.1 Introduction

Organic-inorganic hybrid lead halide perovskites have experienced extraordinary progress in photovoltaic applications due to their unique optoelectronic properties, such as strong optical absorption, small exciton binding energy, and large diffusion length. However, the volatile and thermally unstable nature of the organic components (e.*g.,* $CH_3NH_3^+$, $CH_3(NH_2)_2^+$) has been a challenge for their large-scale applications [176-179]. Alternatively, inorganic cesium lead halide perovskites ($CsPbX_3$), with high stability against thermal stress, light soaking and moisture, have received considerable attention [180]. Various deposition techniques have been developed to synthesize $CsPbX_3$, such as spin-coating, vapor deposition and spray-assisted deposition [181-185]. Recently, we reported a facile and scalable technique using electrodeposition followed by a two-step solution conversion to synthesize $CsPbX_3$ films on a FTO/glass substrate [186]. Inspired by this work, we extended this technique to the synthesis of inorganic mixed-halide $CsPb(XY)_3$ films in the present study. Compared with $CsPbX_3$, mixed-halide perovskites provide a tunable E_g which makes them one of the most promising materials for optoelectronic devices [187]. One of the most studied $CsPb(XY)_3$ is $CsPbI_2Br$ perovskite with a small E_g of 1.90 eV, which has been synthesized by spin-coating and showed a device efficiency of 16.58% recently [180, 183, 188-190]. Moreover, with increasing I content, a smaller E_g of 1.70 eV was reached for $CsPbI_{2.85}Br_{0.15}$, which exhibited excellent thermal and compositional stability, and a high device efficiency of 17.17% due to Br induced suppression of bulk trap-assisted nonradiative recombination and lattice strain relaxation [179]. In addition to mixing Br and I, $CsPbCl_{3-x}Br_x$ was also synthesized using a chemical vapor anion exchange method, and the light emission was controlled in the 421 - 504 nm spectral range by the reaction of the solid $CsPbBr_3$ with HCl vapor. In spite of the tunable E_g and high efficiency, $CsPb(XY)_3$ conveniently suffer from illumination or bias-induced phase segregation when mixing halides in the perovskite structure. Phase segregation was first reported for $MAPb(BrI)_3$ perovskites, then a similar observation was found in $CsPb(BrI)_3$ perovskites . During phase segregation, the excited charge carriers drive the separation of halide species to form heterogeneous regions, with the formation of I-rich regions located along the GB, which results in low- E_g domains causing a red-shift emission [111, 191]. It was believed that the segregated I-rich phases had a funneling effect leading to a loss in open-circuit voltage [192]. However, a recent study revealed that the I-rich phase supported ionic migration, which was beneficial for the performance of perovskite devices [110]. Herein, we evaluated the phase segregation of as-prepared perovskites using PL mapping. $CsPb(ICl)_3$ showed a homogenous PL spectrum at GI and GB. $CsPb(IBr)_3$ and $CsPb(ClBr)_3$ exhibited a red-shift emission at GB, probably due to the absence the segregated I-rich and Br-rich phases, respectively. We also studied the photoactivity of $CsPb(ICl)_3$, $CsPb(IBr)_3$ and $CsPb(ClBr)_3$ films in a liquid PEC cell to evaluate their performance, and all of them showed a stable Iph response under chipped illumination. Compared with $CsPb(IBr)_3$ and $CsPb(ClBr)_3$, $CsPb(ICl)_3$ exhibited a Iph

of ~ 16 μA/cm^2 at OCP. In this work, we established a facile and scalable method to synthesize $CsPb(XY)_3$ family, and studied their crystal structure and optoelectronic properties, providing a prospect on the development and commercialization of $CsPb(XY)_3$ perovskites.

5.2 Materials and methods

5.2.1 Chemicals and materials

Methanol (HPLC, ≥ 99.9%), ethanol (anhydrous, ≥ 99.5%), acetone (ACS reagent, ≥ 99.8%), acetic acid (ACS reagent, ≥ 99.7%), hydrochloric acid (ACS reagent, 37%), hydrobromic acid (ACS reagent, 48%), hydroiodic acid (ACS reagent, 55%), sodium acetate trihydrate (ACS reagent, ≥ 99%), lead acetate trihydrate (ACS reagent, ≥ 99%), tetrabutylammonium hexafluorophosphate (TBAPF6), dichloromethane, benzoquinone (BQ), cesium chloride (99.9%), cesium bromide (99.9%) and cesium iodide (99.9%) were purchased from Sigma-Aldrich. All chemicals were used as received without further purification. Fluorine-doped tin oxide coated glass substrates (FTO, 6–9 Ω/square) were purchased from Delta Technologies, Inc. Water was purified using a Millipore system (18.2 MΩ cm).

5.2.2 Electrodeposition

FTO slides (0.5 cm × 2.5 cm) were cleaned successively for 20 min in acetone, methanol and water followed by drying with compressed air. The electrodeposition bath was an aqueous solution (pH 5.5) containing 1.0 M sodium acetate and 0.1 M lead (II) acetate. Concentrated acetic acid was used to adjust the pH. Electrodeposition was carried out according to the method of Popov et al. [8] using a current density of 0.25 mA cm^{-2} for 900 s using a potentiostat (Solartron 1470) under ambient conditions in a three-electrode cell using a FTO slide as working electrode (area = 1 cm^2), a platinum gauze counter electrode and an Ag wire quasi-reference electrode. The resulting PbO_2 film on FTO was rinsed with water and annealed at 100 °C in air for 10 min.

5.2.3 Two-step chemical conversion of PbO_2 to $CsPb(XY)_3$

Conversion of the as-deposited PbO_2 to PbX_2 was carried out in ethanol containing 50 mM of the corresponding hydrohalic acid, using a conversion time of 6 min for PbI_2, 4 h for $PbBr_2$ and 40 min for $PbCl_2$ at room temperature. The subsequent conversion of PbX_2 to $CsPb(XY)_3$ was achieved by immersing the PbX_2 films in methanol containing 20 mM CsY for 35 min for $CsPb(ICl)_3$ and $CsPb(ClBr)_3$, and $CsPb(IBr)_3$ for 65 min at room temperature, followed by thermal

annealing at 400 ◦C for 30 min.

5.2.4 Characterization

UV–Vis absorption spectra were obtained with a UV–VIS-NIR spectrophotometer (Lambda 750, Perkin-Elmer). X-ray diffraction patterns were obtained using a Bruker D8 Advance diffractometer with a Cu-Kα radiation source. Images of the surface morphology of the perovskite films were obtained using a scanning electron microscope (SEM) (JEOL JSM7600F). Photoluminescence (PL) mapping was measured using a hyperspectral microscope (Photon etc). The laser excitation at 405nm with intensity comparable with 100 sun flux was used.

5.2.5 Electrochemical measurements

The photoactivity of perovskite films was measured in a photolelctrochemical cell using a Potentiostat (BioLogic SP-300). $CsPb(XY)_3$ films with ~0.07 cm^2 area exposed to the electrolyte functioned as the working electrode, a Pt wire as the counter electrode, and an Ag wire as a quasi-reference electrode. The supporting electrolyte was 0.1 M $TBAPF_6$ in dichloromethane, and 2 mM BQ was used as the redox mediator. The solution was purged by argon bubbling for 10 min before measurement. The light source was a blue LED with an illumination intensity of 50 mW/m^2 at 405 nm.

5.3 Results and discussion

$CsPb(XY)_3$ films were prepared by electrodeposition of PbO_2 followed by a two-step chemical conversion process under open-air conditions [47, 186]. The first conversion of the electrodeposited PbO_2 on FTO to PbX_2 was carried out in ethanol containing 50 mM of HX. The second conversion was carried out in methanol containing 20 mM CsY to form the corresponding $CsPb(XY)_3$, as shown in equation 5.1 - 5.6. Following chemical conversion, $CsPb(XY)_3$ films were annealed at 400 ◦C for 30 min, and their crystal structures were determined by XRD, as shown in Fig. 5.1. Fig. 5.1(a) represents the conversion of PbI_2 film to $CsPb(ICl)_3$ after dipping in a CsCl solution for 35 minutes, which was indexed to the cubic phase of $CsPbCl_3$ (PDF No.: 00-018-0366). However, the dipping of the $PbCl_2$ film in CsI solution gave a non-perovskite structure, as shown in Fig. 5.1(b). The dipping of a PbI_2 film in CsBr solution for 65 minutes yielded the orthorhombic phase of $CsPbBr_3$ (PDF No.: 00-018-0364), and the dipping of $PbBr_2$ film in a CsI solution gave a non-perovskite structure, as shown in Fig. 5.1(c, d). The dipping of a $PbCl_2$ film in CsBr solution yielded a cubic phase of $CsPbCl_3$ doped with Br^-, which

shows a Br-shift of about 2^{o}, and the dipping of a $PbBr_2$ film in a CsCl solution gave a non-perovskite structure, as shown in Fig. 5.1(e, f). It is noted that even $CsPb(ICl)_3$ and $CsPb(IBr)_3$ didn't show any I-shift in their XRD diffractogram, it is still possible that both are still I-doped [193, 194]. These results indicate that the conversion sequence plays an important role in the formation of the final perovskite crystal structure for $CsPb(XY)_3$. We are more interested in $CsPb(ICl)_3$, $CsPb(IBr)_3$, $CsPb(ClBr)_3$, and the following discussion will focus on these 3 perovskite structures.

$$PbI_2\ (s) + CsCl\ (aqueous) \rightarrow CsPb(ICl)_3\ (s) \qquad (5.1)$$

$$PbI_2\ (s) + CsBr\ (aqueous) \rightarrow CsPb(IBr)_3\ (s) \qquad (5.2)$$

$$PbCl_2\ (s) + CsBr\ (aqueous) \rightarrow CsPb(ClBr)_3\ (s) \qquad (5.3)$$

$$PbCl_2\ (s) + CsI\ (aqueous) \rightarrow CsPb(ClI)_3\ (s) \qquad (5.4)$$

$$PbBr_2\ (s) + CsI\ (aqueous) \rightarrow CsPb(BrI)_3\ (s) \qquad (5.5)$$

$$PbBr_2\ (s) + CsCl\ (aqueous) \rightarrow CsPb(BrCl)_3\ (s) \qquad (5.6)$$

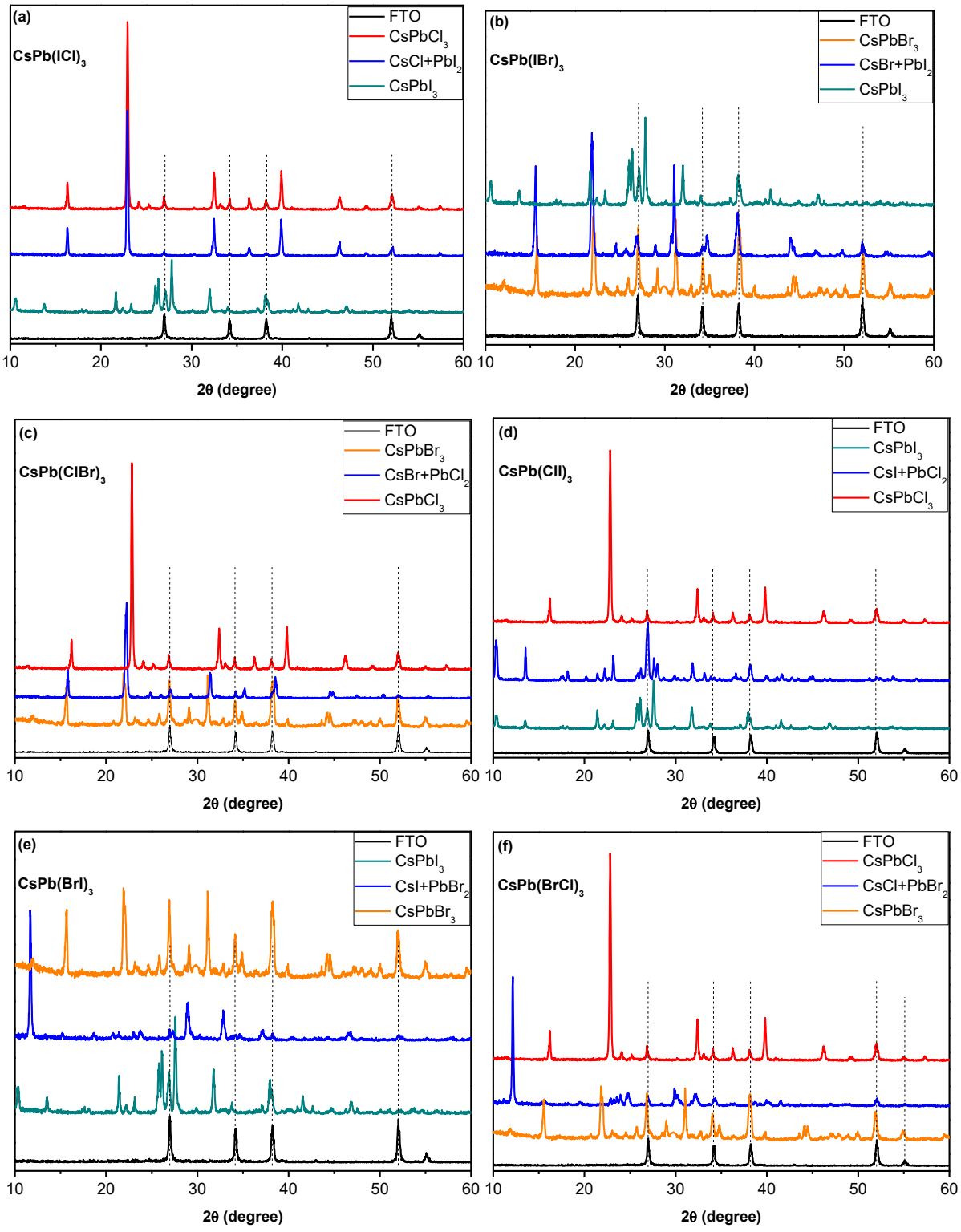

Figure 5.1 Screening of $CsPb(XY)_3$ perovskite structure by XRD. (a) $CsPb(ICl)_3$, (b) $CsPb(IBr)_3$, (c) $CsPb(ClBr)_3$, (d) $CsPb(ClI)_3$, (e) $CsPb(BrI)_3$, (f) $CsPb(BrCl)_3$.

To further understand the transition dynamics of PbX_2 films to $CsPb(XY)_3$, the conversion process was monitored by XRD and SEM as shown in Fig. 5.2. Fig. 5.2(a) shows the crystal structure transition of a PbI_2 film dipped in a CsCl solution for 1, 4, 7, and 35 minutes without annealing, and then annealed at 350 ^oC for 30 min. The conversion began in less than 1 minute, as shown by indexing at 16^o for 100 peak of cubic $CsPbCl_3$. The corresponding SEM image shows that the film morphology changes from need-shaped to cubic with increasing conversion time (Fig. 5.2(a-d)). Up to 35 min, the crystal structure completely transfers to cubic $CsPbCl_3$, as well as the film morphology changes to cubic (Fig. 5.2(e-f)). Annealing improved the crystal quality by removing solvent in the final film, and led to film coalescence. For the crystal structure transition of a PbI_2 film dipped in CsBr solution, XRD indicates that there is no structure change even after 65min-conversion (Fig. 5.3(a)), as well as the needle-shape film morphology doesn't show any change (Fig. 5.3(b-e). However, annealing led to the transition to orthorhombic $CsPbBr_3$ with a cubic film morphology (Fig. 5.3(f)). These results indicate that CsCl in solution drives the transition of the PbI_2 film to cubic $CsPbCl_3$ without annealing in a short time. However, CsBr in solution requires the annealing to achieve the transition of PbI_2 to the orthorhombic $CsPbBr_3$ perovskite.

The conversion of a $PbCl_2$ film dipped in a CsBr solution shows an instant crystal structure transition in 1 min as indicated by XRD (Fig. 5.4(a)). SEM images also show a constant cubic film morphology from 1 to 35 min (Fig. 5.4(b-f)). Compared with $CsPb(ICl)_3$ and $CsPb(IBr)_3$, Br- can easily prompt the transition from $PbCl_2$ to $CsPb(ClBr)_3$ with a 2^o Br-shift from cubic $CsPbCl_3$.

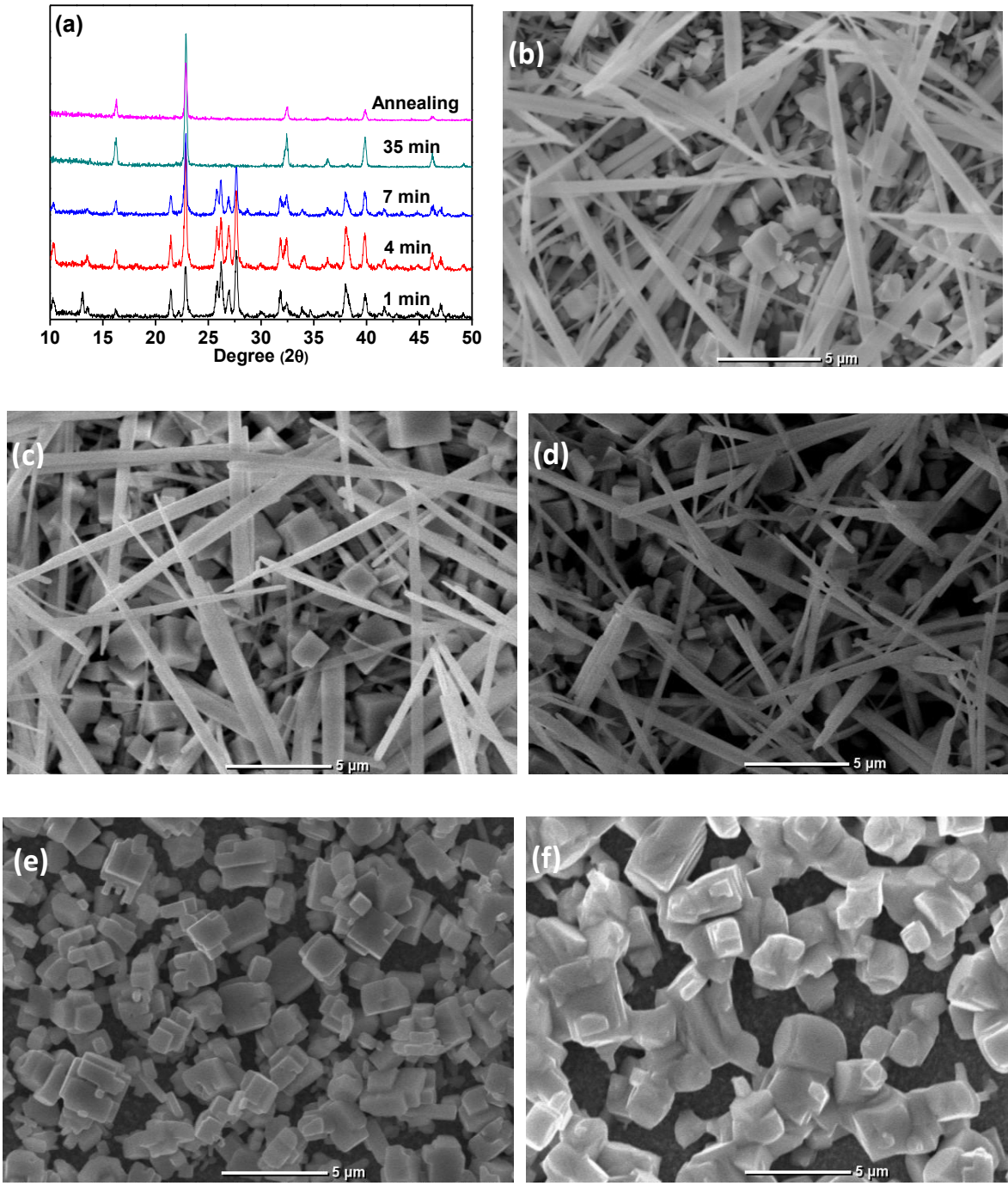

Figure 5.2 Monitoring of the conversion to $CsPb(ICl)_3$ by XRD and SEM in function of dipping time. (a) Crystal structure, (b) dipping for 1 min, (c) dipping for 4 min, (d) dipping for 7 min, (e) dipping for 35 min, (f) annealing after dipping for 35 min.

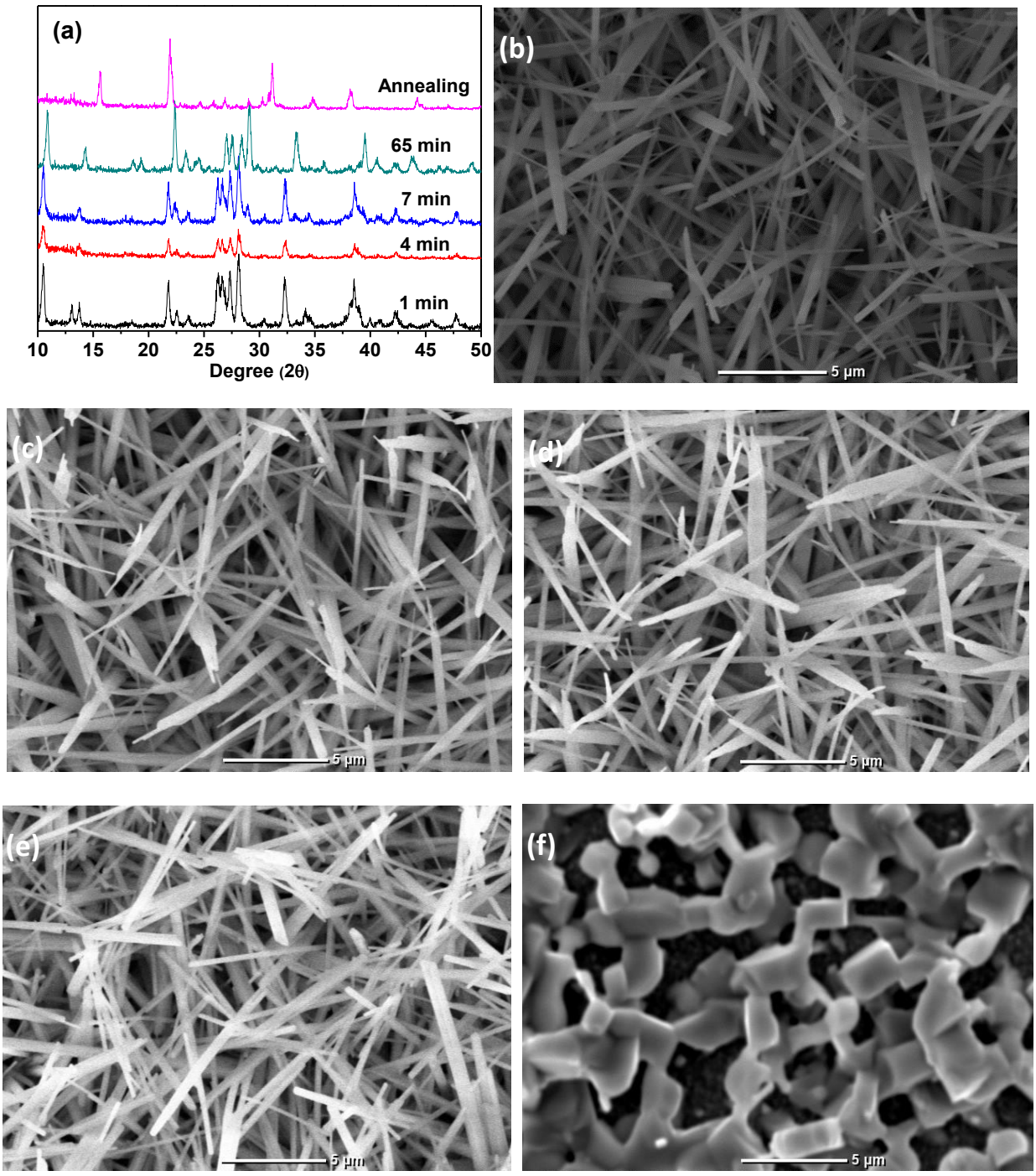

Figure 5.3 Monitoring of the conversion to $CsPb(IBr)_3$ by XRD and SEM in function of dipping time. (a) Crystal structure, (b) dipping for 1 min, (c) dipping for 4 min, (d) dipping for 7 min, (e) dipping for 65 min, (f) annealing after dipping for 65 min.

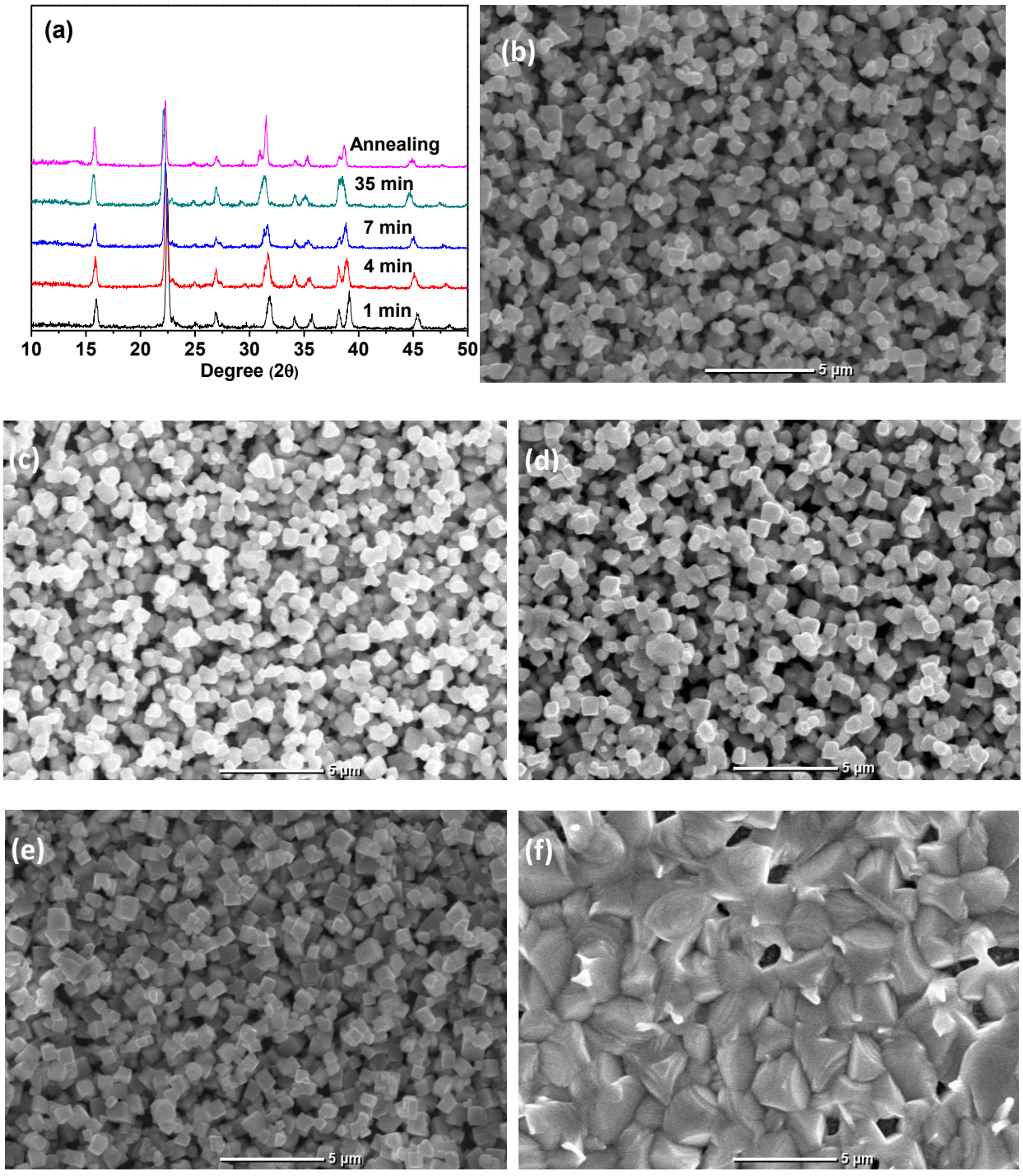

Figure 5.4 Monitoring of the conversion to $CsPb(ClBr)_3$ by XRD and SEM in function of dipping time. (a) Crystal structure, (b) dipping for 1 min, (c) dipping for 4 min, (d) dipping for 7 min, (e) dipping for 35 min, (f) annealing after dipping for 35 min.

The UV-Vis absorbance of $CsPb(XY)_3$ films on FTO/glass substrates are reported in Fig. 5.5.

$CsPb(ICl)_3$ and $CsPb(ClBr)_3$, which adopt a cubic phase, show an absorption onset at 425 nm (2.92 eV) and 520nm (2.39 eV), respectively. $CsPb(ICl)_3$ is determined to be an almost pure cubic $CsPbCl_3$ perovskite (Fig. 5.1(a)), and $CsPb(ClBr)_3$ is a Br^--doped cubic $CsPbCl_3$ perovskite (Fig. 5.1(c)). As expected, Br^- doping significantly decreases the E_g of the $CsPbCl_3$ perovskite. $CsPb(IBr)_3$ adopts an almost pure orthorhombic $CsPbBr_3$ perovskite, which shows an absorption onset at 558 nm, corresponding to an optical E_g of 2.23 eV.

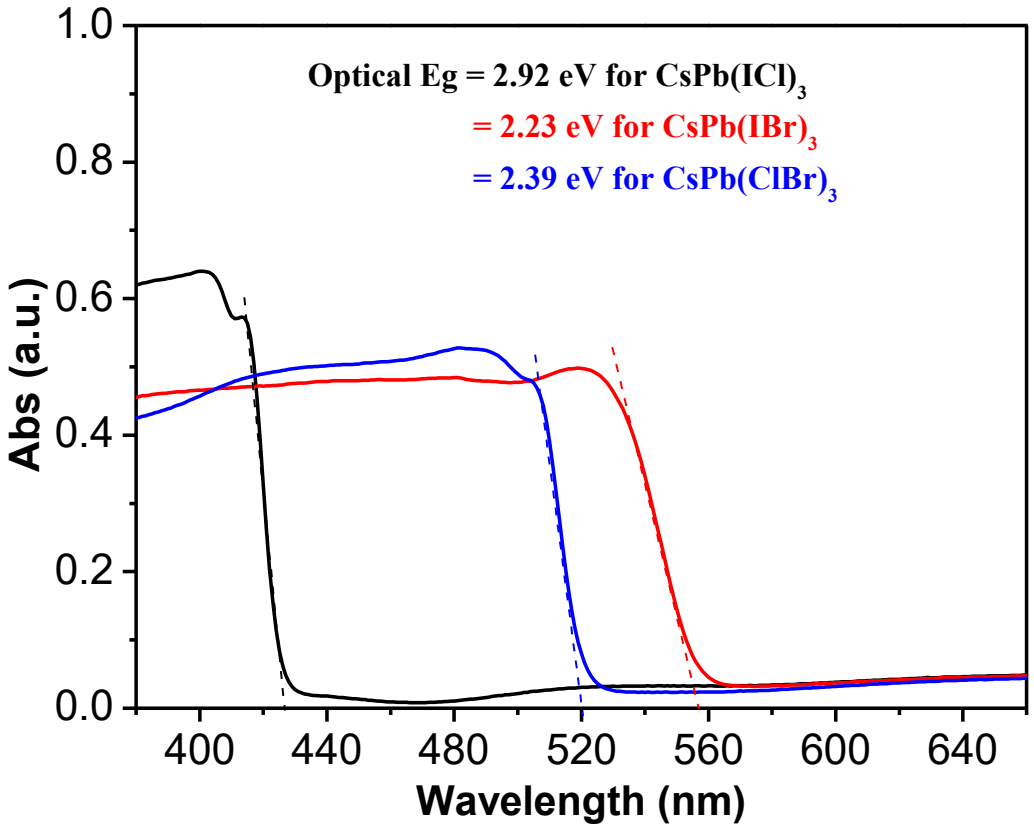

Figure 5. 5 UV-Vis absorption spectra of $CsPb(ICl)_3$, $CsPb(IBr)_3$, $CsPb(ClBr)_3$ films.

The photoluminescence (PL) of perovskite originates from the radiative recombination of photoexcited electrons (e^-) and holes (h^+), which is useful to evaluate the optoelectronic properties such as the band structure, as well as the presence of defects and impurities [195]. Hoke et al. first reported the reversible photoinduced halide segregation through the PL spectra of $MAPb(BrI)_3$ thin films [117]. It was found that the initial perovskite phase with homogeneous halide composition could transfer to I/Br-rich heterogeneous phases after a certain dosage of light soaking, and there was a halide-remixing process once the light excitation was removed. The photogenerated I/Br-rich domains could attract photoexcited carriers from adjacent phases due to energetic confinement, and then dominate the (non-)radiative recombination. Fig. 5.6

shows the PL mapping of $CsPb(ICl)_3$ that was performed with a 405nm-laser excitation at 100 sun illumination. Both the grain interior (GI) and grain boundary (GB) show a PL peak at ~ 421nm (2.95 eV), in good agreement with the optical E_g determined from UV-vis absorption spectra, which indicates the chemical homogeneity between GB and GI for I/Cl-mixed cesium lead perovskite under high light intensity. Different from $CsPb(ICl)_3$, $CsPb(IBr)_3$ shows a red-shift from 543nm (2.29 eV) for the GI to 550nm (2.26 eV) for the GB due to the formation of I^- rich domains for the I/Br-mixed cesium lead perovskite (see Fig. 5.7). The halide segregation at GBs leads to a PL and E_g shift. Similar with $CsPb(ICl)_3$, $CsPb(ClBr)_3$ shows the same PL peak at 500nm (2.48eV) for the GI and the GB (see Fig. 5.8), which proves the chemical homogeneity at high light intensity between GB and GI for Br/Cl-mixed cesium lead perovskites. We can see, I/Cl and Cl/Br-mixed cesium lead perovskites have a highly stable chemical composition, and halide segregation happens for I/Br-mixed cesium lead perovskites under light which results in the heterogeneous halide rich regions and lower Eg. On the other hand, the formation of this local heterostructure may enhance defect tolerance for the final perovskites [196, 197].

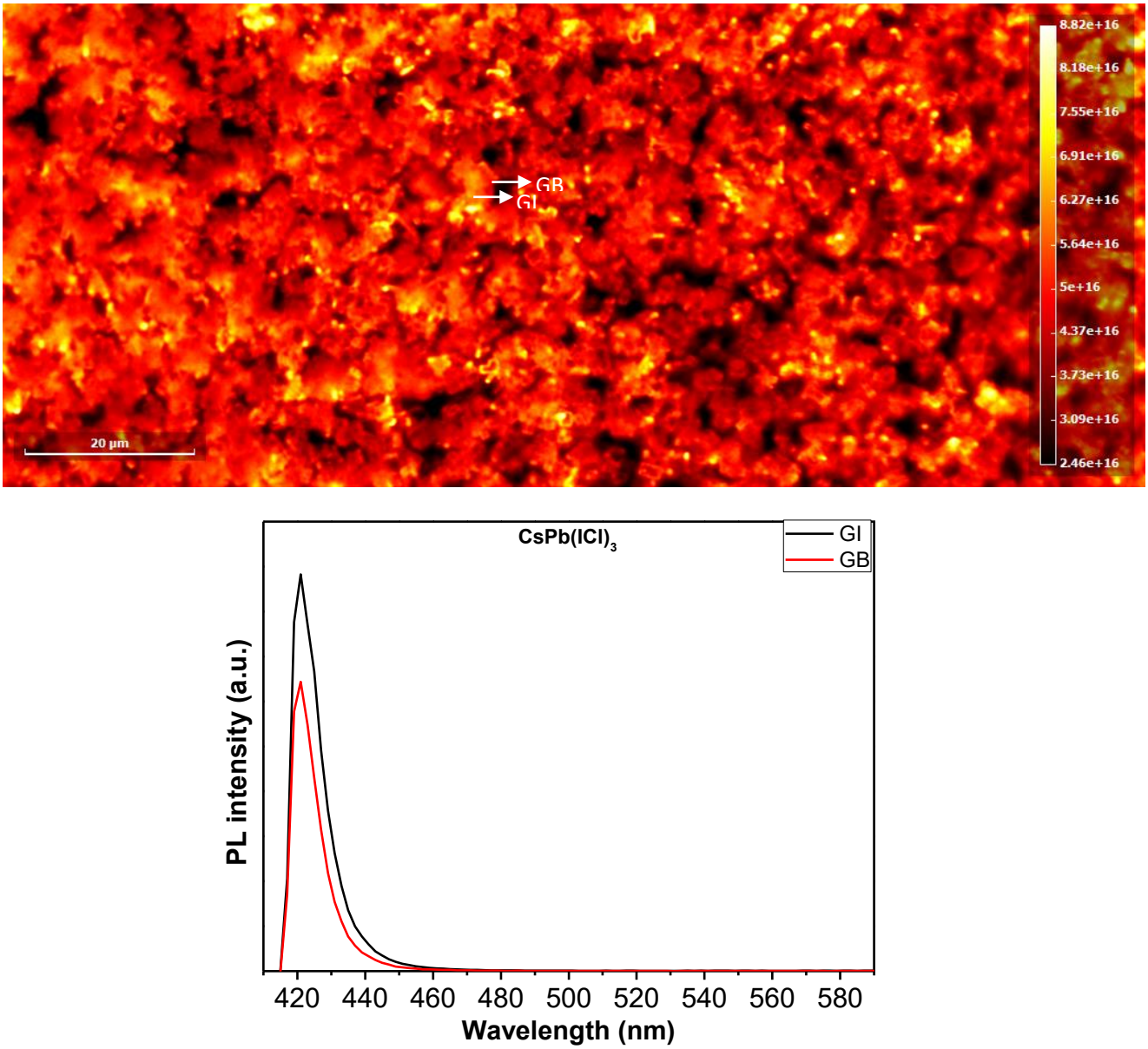

Figure 5.6 (Top) hyperspectral PL mapping of $CsPb(ICl)_3$ film at emission of 421nm, map was taken with 405 nm laser excitation with 100 sun intensity. (Bottom) PL extracted for GI and GB.

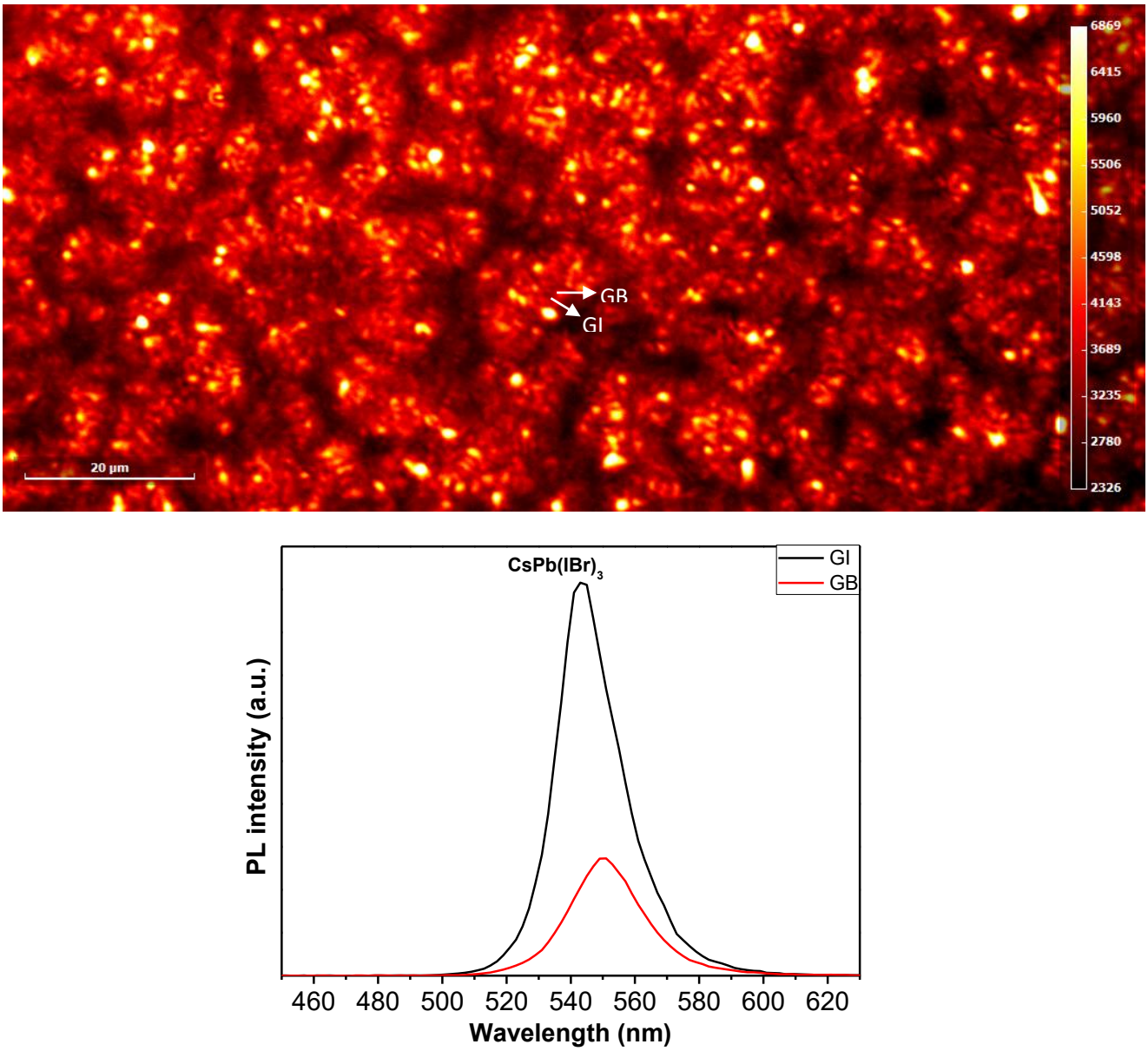

Figure 5.7 (Top) hyperspectral PL mapping of $CsPb(IBr)_3$ film at emission of 553nm, map was taken with 405 nm laser excitation with 100 sun intensity. (Bottom) PL extracted for GI and GB.

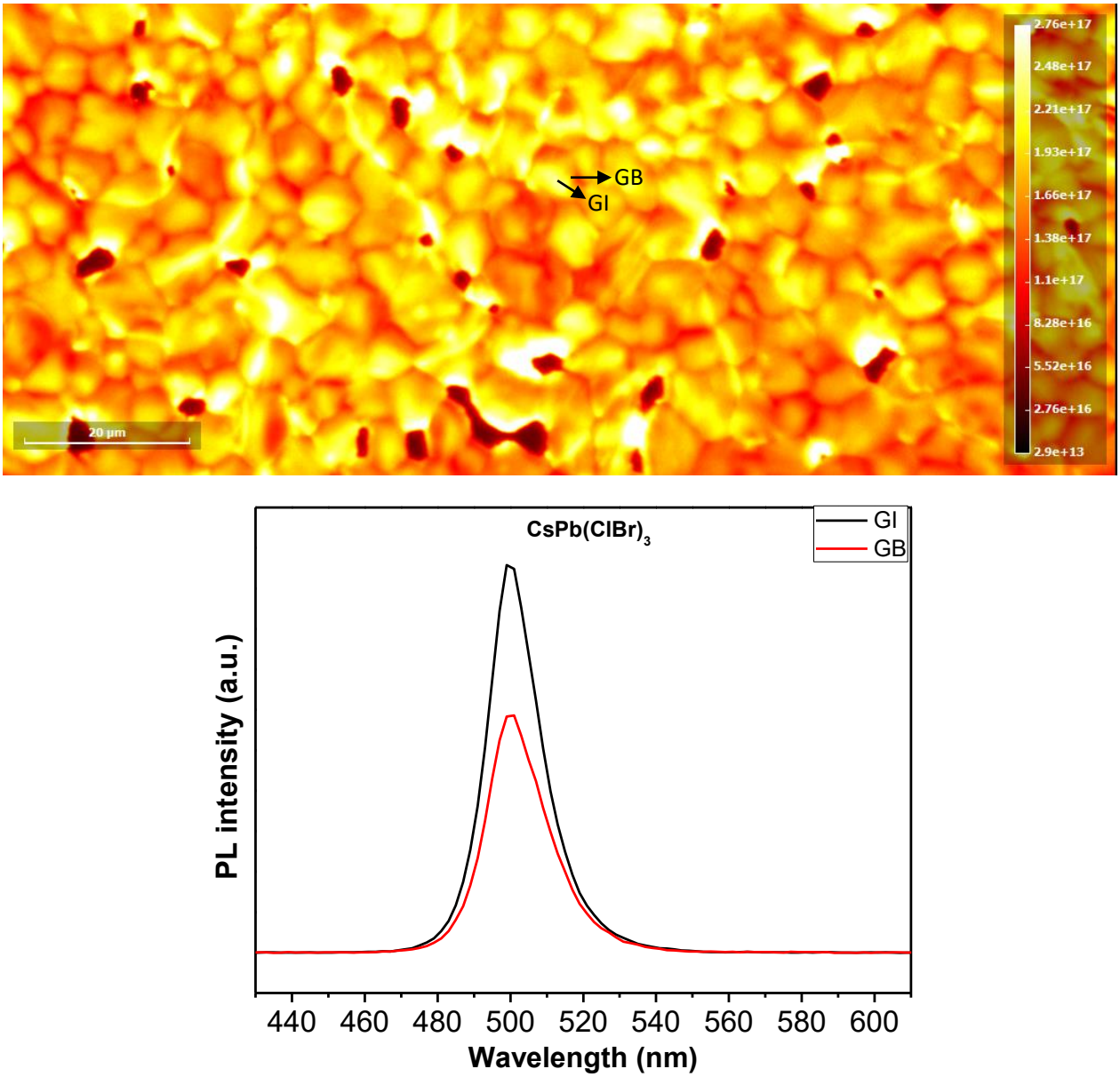

Figure 5.8 (Top) hyperspectral PL mapping of $CsPb(ClBr)_3$ film at emission of 501nm, map was taken with 405 nm laser excitation with 100 sun intensity. (Bottom) PL extracted for GI and GB.

Fig. 5.9 shows the normalized PL intensity for GI and GB of $CsPb(ICl)_3$, $CsPb(ClBr)_3$, $CsPb(IBr)_3$ films. As discussed previously, $CsPb(ICl)_3$ adopts an almost pure cubic phase of $CsPbCl_3$, and $CsPb(ClBr)_3$ adopts in Br/Cl-mixed cubic phase, which lead to a PL red-shift and lower E_g in comparison with cubic $CsPb(ICl)_3$. $CsPb(IBr)_3$ adopts an almost pure orthorhombic phase of $CsPbBr_3$ with a PL red-shift and lower E_g compared with $CsPb(ClBr)_3$. Meanwhile, the relative intensity of the GB to the GI is lower for $CsPb(IBr)_3$ than that of $CsPb(ICl)_3$ and $CsPb(ClBr)_3$ which indicates a stronger non-radiative recombination of charge carriers at I^- rich domains. I-rich

segregated domains act as recombination centers for photogenerated charge carriers by trapping of carriers and hindering e^- extraction, and finally impact negatively on the performance of mixed halide perovskites [198, 199].

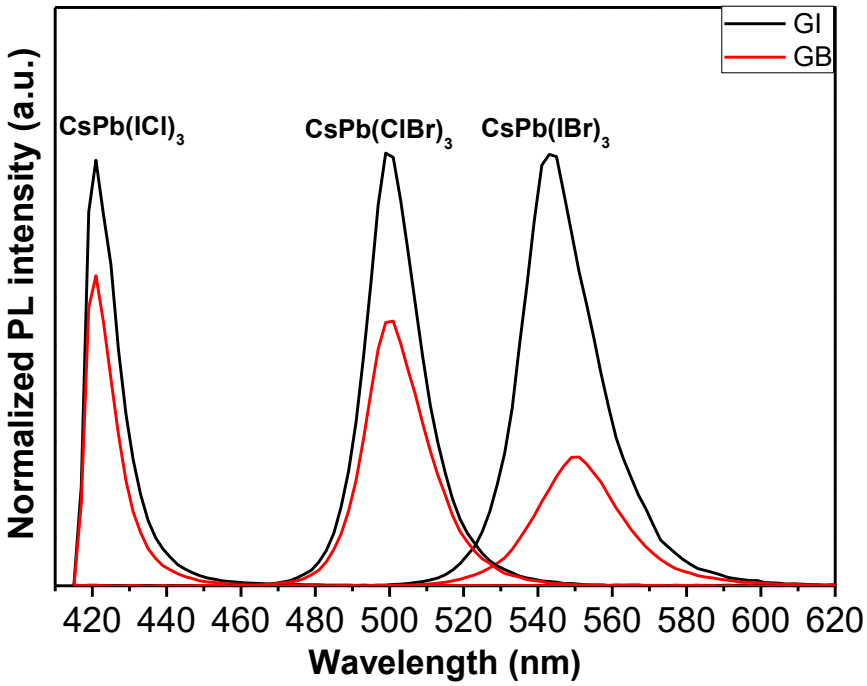

Figure 5.9 Normalized PL intensity for GI and GB of $CsPb(ICl)_3$ $CsPb(ClBr)_3$ $CsPb(IBr)_3$ films.

To further investigate the as-prepared perovskite films, the I_{ph} was measured in a liquid junction photoelectrochemical solar cell using BQ as redox mediator. As shown in Fig. 5.10, $CsPb(XY)_3$ films at open circuit potential (OCP) show a sharp increase of the cathodic current when the light is turned on due to the fast light-induced generation of e^--h^+ pair, followed by a slow current decay. This decay may be attributed to the trap-assisted recombination at GB or interface of perovskite films. The negative I_{ph} indicates the transfer of e^- from FTO/perovskite film to electrolyte for the reduction of BQ. $CsPb(ICl)_3$ displays the largest I_{ph} of ~ 16 µA/cm^2 followed by $CsPb(ClBr)_3$ of ~ 6 µA/cm^2 and $CsPb(IBr)_3$ of ~ 4 µA/cm^2. When the light is turned off, the current comes back to its dark level at ~ 0 µA/cm^2. Meanwhile, the I_{ph} at - 0.10 V *vs.* OCP was measured for $CsPb(XY)_3$ films, which shows an increase of 25% of its initial Iph for $CsPb(ICl)_3$, 17% for $CsPb(ClBr)_3$ and 200% for $CsPb(IBr)_3$. Furthermore, the perovskite films exhibit stable photocurrent response under chopped illumination.

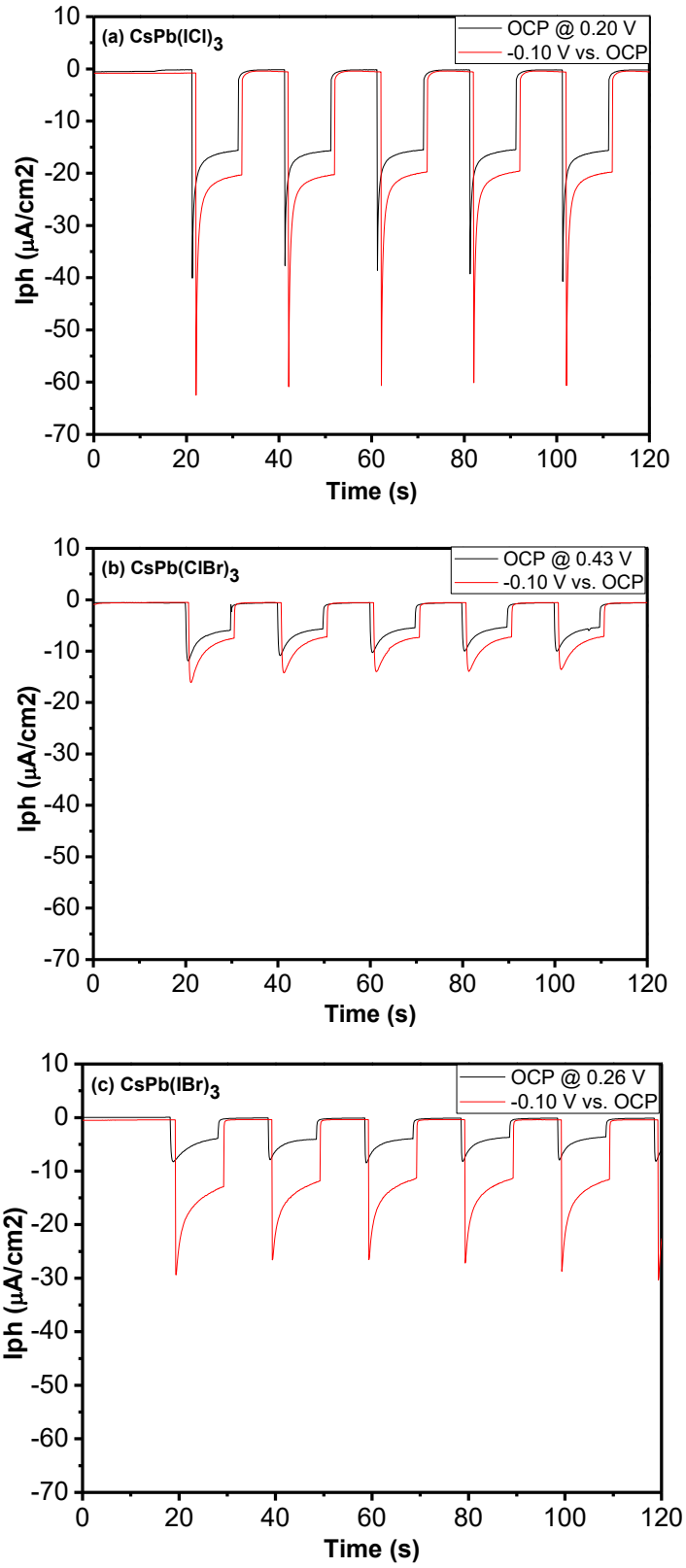

Figure 5.10 Iph response of $CsPb(XY)_3$ films in 0.05M $TBAPF_6$ in DCM with 2mM BQ.

5.4. Conclusions

In summary, we demonstrated a facile and scalable deposition technique for the synthesis of a series of $CsPb(XY)_3$ films on a FTO/glass substrate. Their crystal structure was screened by XRD to identify three perovskites $CsPb(ICl)_3$, $CsPb(IBr)_3$, and $CsPb(ClBr)_3$. $CsPb(IBr)_3$ showed a red-shift PL at GB probably due to phase segregation. However, $CsPb(ICl)_3$ and $CsPb(ClBr)_3$ didn't show PL shift which conform the compositional homogeneity between GB and GI. All of the obtained mixed-halide perovskites exhibited a stable photoresponse under chopped illumination in a liquid PEC cell, and $CsPb(ICl)_3$ had the largest I_{ph} of ~ 16 $\mu A/cm^2$. These results pave the way for the development of efficient and scaling-up mixed-halide perovskites.

CONCLUSION AND PERSPECTIVES

In this work, we demonstrated the electrodeposition of PbO_2 onto an FTO substrate followed by either a two-step or one-step chemical conversion used to synthesize $MAPbX_3$ films in an ambient atmosphere. Their crystal structure, film morphology, electronic structure and photoresponse were studied. The $MAPbX_3$ films obtained by one-step conversion showed a large grain size and an improved photocurrent compared with that synthesized by two-step conversion, which enables the one-step conversion a more economical and effective route toward high-quality $MAPbX_3$ perovskite films. These results show that ED represents one of the most versatile techniques for the deposition of LHP films with the desirable characteristics.

Meanwhile, the organic component in hybrid $MAPbX_3$ perovskites, MA^+, was replaced by Cs^+ to form the more thermal stable inorganic $CsPbX_3$ perovskites using PbO_2 electrodeposition followed by the two-step conversion. This is the first example of growing $CsPbX_3$ perovskite films in a solution from the electrodeposited PbO_2 in an ambient atmosphere. The wide bandgap $CsPbCl_3$ perovskite exhibited a larger corrosion resistance than $CsPbBr_3$ due to the role of chloride in enhancing the stability of LHP. Furthermore, wide bandgap $CsPbX_3$ perovskites are finding increasing applications in photoelectrodes, LED and photodetectors where electrodeposition can be a valuable approach for their fabrication. Finally, a series of mixed-halide $CsPb(XY)_3$ films were prepared by modifying the chemical composition of the conversion bath during the two-step conversion. Their crystal structures were screened by XRD to identify three perovskites, $CsPb(ICl)_3$, $CsPb(IBr)_3$ and $CsPb(ClBr)_3$, which exhibited stable photoresponse under chopped illumination in a liquid PEC cell. $CsPb(IBr)_3$ showed a red-shift PL at GB probably due to phase segregation. However, $CsPb(ICl)_3$ and $CsPb(ClBr)_3$ didn't show PL shift which can confirm the compositional homogeneity between GB and GI. The pathway from $CsPbX_3$ to $CsPb(XY)_3$ perovskites provides a facile strategy to adjust the optoelectronic properties (crystal structure, E_g, stability, photoactivity, etc.) of inorganic perovskites. These results may pave the way for the development of efficient and scaling-up mixed-halide perovskites.

In summary, we represented a facile and scalable solution deposition technique for the synthesis of hybrid $MAPbX_3$ perovskite films and inorganic $CsPbX_3$, $CsPb(XY)_3$ perovskite films. Their crystal structure, film morphology, electronic structure and photoactivity are studied to understand their optoelectronic properties towards highly efficient and stable perovskites.

One of the key factors deciding LHP devices is their architecture, which can be optimized by electrodepositing transport layers (ETL, HTL) to avoid short circuits in the devices. TiO_2 and poly(3,4-ethylenedioxythiophene) (PEDOT) have been successfully electrodeposited to form ETL and HTL to prepare a $FTO/TiO_2/MAPbI_3/PEDOT$ solar cell, which opens a new opportunity to employ electrochemistry to assemble complex architectures of perovskite devices. Several

materials could be electrodeposited, such as SnO_2, CuSCN, poly[bis(4-phenyl)(2,4,6-trimethylphenyl)amine] (PTAA) and poly(3-hexylthiophene-2,5-diyl) (P3HT), rather than using spin-coated which is non-applicable on a large surface. The main challenge is to find an applicable non-aqueous solution to electrodeposit LHP. Meanwhile, the E_g engineering of $CsPbX_3$ through mixing halide offers great versatility in promoting the photoelectronic and photocatalytic performance of inorganic perovskites, which is useful in CO_2 reduction and H_2 generation.

BIBLIOGRAPHIE

1. Kojima, A., et al., *Organometal Halide Perovskites as Visible-Light Sensitizers for Photovoltaic Cells.* Journal of the American Chemical Society, 2009. **131**(17): p. 6050-6051.
2. Pham, H.D., et al., *Development of Dopant-Free Organic Hole Transporting Materials for Perovskite Solar Cells.* Advanced Energy Materials, 2020. **10**(13): p. 1903326.
3. Rhee, S., K. An, and K.-T. Kang, *Recent Advances and Challenges in Halide Perovskite Crystals in Optoelectronic Devices from Solar Cells to Other Applications.* Crystals, 2021. **11**(1): p. 39.
4. Rezaee, E., et al., *A route towards the fabrication of large-scale and high-quality perovskite films for optoelectronic devices.* Scientific Reports, 2022. **12**(1): p. 7411.
5. Schmidt, L.C., et al., *Nontemplate Synthesis of CH3NH3PbBr3 Perovskite Nanoparticles.* Journal of the American Chemical Society, 2014. **136**(3): p. 850-853.
6. Horváth, E., et al., *Nanowires of Methylammonium Lead Iodide (CH3NH3PbI3) Prepared by Low Temperature Solution-Mediated Crystallization.* Nano Letters, 2014. **14**(12): p. 6761-6766.
7. Li, P., et al., *Two-Dimensional CH3NH3PbI3 Perovskite Nanosheets for Ultrafast Pulsed Fiber Lasers.* ACS Applied Materials & Interfaces, 2017. **9**(14): p. 12759-12765.
8. Yusheng Lei, Y.C., Sheng Xu, *Single-crystal halide perovskites: Opportunities and challenges.* Matter, 2021. **4**(7): p. 42.
9. Sharenko, A. and M.F. Toney, *Relationships between Lead Halide Perovskite Thin-Film Fabrication, Morphology, and Performance in Solar Cells.* Journal of the American Chemical Society, 2016. **138**(2): p. 463-470.
10. Harikesh, P.C., et al., *Hybrid organic–inorganic halide perovskites for scaled-in neuromorphic devices.* MRS Bulletin, 2020. **45**(8): p. 641-648.
11. Chen, Q., et al., *Under the spotlight: The organic–inorganic hybrid halide perovskite for optoelectronic applications.* Nano Today, 2015. **10**(3): p. 355-396.
12. Chen, Y., X. Liu, and Y. Zhao, *Organic Matrix Assisted Low-temperature Crystallization of Black Phase Inorganic Perovskites.* Angewandte Chemie International Edition, 2022. **61**(1): p. e202110603.
13. Quan, L.N., et al., *Perovskites for Next-Generation Optical Sources.* Chemical Reviews, 2019. **119**(12): p. 7444-7477.
14. Kang, J. and J.H. Cho, *Organic–inorganic hybrid perovskite electronics.* Physical Chemistry Chemical Physics, 2020. **22**(24): p. 13347-13357.
15. Ünlü, F., et al., *Understanding the interplay of stability and efficiency in A-site engineered lead halide perovskites.* APL Materials, 2020. **8**(7): p. 070901.
16. Li, Z., et al., *Scalable fabrication of perovskite solar cells.* Nature Reviews Materials, 2018. **3**(4): p. 18017.
17. Wang, S., et al., *Perovskite Nanocrystals: Synthesis, Stability, and Optoelectronic Applications.* Small Structures, 2021. **2**(3): p. 2000124.
18. Hao, J. and X. Xiao, *Recent Development of Optoelectronic Application Based on Metal Halide Perovskite Nanocrystals.* Frontiers in Chemistry, 2022. **9**.

19. Oku, T., *Crystal Structures of CH3NH3PbI3 and Related Perovskite Compounds Used for Solar Cells*. 2015, sine loco: IntechOpen.
20. Marronnier, A., et al., *Anharmonicity and Disorder in the Black Phases of Cesium Lead Iodide Used for Stable Inorganic Perovskite Solar Cells.* ACS Nano, 2018. **12**(4): p. 3477-3486.
21. Haeger, T., et al., *Thermal properties of CsPbCl3 thin films across phase transitions.* Journal of Physics: Materials, 2020. **3**(2): p. 024004.
22. Lee, J.-W., et al., *Dynamic structural property of organic-inorganic metal halide perovskite.* iScience, 2021. **24**(1): p. 101959.
23. Yu, C.-J., *Advances in modelling and simulation of halide perovskites for solar cell applications.* Journal of Physics: Energy, 2019. **1**(2): p. 022001.
24. Tao, S.X., X. Cao, and P.A. Bobbert, *Accurate and efficient band gap predictions of metal halide perovskites using the DFT-1/2 method: GW accuracy with DFT expense.* Scientific Reports, 2017. **7**(1): p. 14386.
25. Castelli, I.E., et al., *Bandgap calculations and trends of organometal halide perovskites.* APL Materials, 2014. **2**(8): p. 081514.
26. Giorgi, G., et al., *Cation Role in Structural and Electronic Properties of 3D Organic–Inorganic Halide Perovskites: A DFT Analysis.* The Journal of Physical Chemistry C, 2014. **118**(23): p. 12176-12183.
27. Quarti, C., C. Katan, and J. Even, *Physical properties of bulk, defective, 2D and 0D metal halide perovskite semiconductors from a symmetry perspective.* Journal of Physics: Materials, 2020. **3**(4): p. 042001.
28. Selig, O., et al., *Organic Cation Rotation and Immobilization in Pure and Mixed Methylammonium Lead-Halide Perovskites.* Journal of the American Chemical Society, 2017. **139**(11): p. 4068-4074.
29. Li, Z., et al., *Stabilizing Perovskite Structures by Tuning Tolerance Factor: Formation of Formamidinium and Cesium Lead Iodide Solid-State Alloys.* Chemistry of Materials, 2016. **28**(1): p. 284-292.
30. Wang, Z., et al., *Stability of Perovskite Solar Cells: A Prospective on the Substitution of the A Cation and X Anion.* Angewandte Chemie International Edition, 2017. **56**(5): p. 1190-1212.
31. Deretzis, I., et al., *Stability and Degradation in Hybrid Perovskites: Is the Glass Half-Empty or Half-Full?* The Journal of Physical Chemistry Letters, 2018. **9**(11): p. 3000-3007.
32. Senocrate, A., et al., *Thermochemical Stability of Hybrid Halide Perovskites.* ACS Energy Letters, 2019. **4**(12): p. 2859-2870.
33. Conings, B., et al., *Intrinsic Thermal Instability of Methylammonium Lead Trihalide Perovskite.* Advanced Energy Materials, 2015. **5**(15): p. 1500477.
34. Liu, D., et al., *Structural Properties and Stability of Inorganic CsPbI3 Perovskites.* Small Structures, 2021. **2**(3): p. 2000089.
35. Yao, Z., W. Zhao, and S. Liu, *Stability of the CsPbI3 perovskite: from fundamentals to improvements.* Journal of Materials Chemistry A, 2021. **9**(18): p. 11124-11144.
36. Wei, D., et al., *Photo-induced degradation of lead halide perovskite solar cells caused by the hole transport layer/metal electrode interface.* Journal of Materials Chemistry A, 2016. **4**(5): p. 1991-1998.

37. Zhang, D., et al., *Degradation pathways in perovskite solar cells and how to meet international standards.* Communications Materials, 2022. **3**(1): p. 58.
38. Hoye, R.L.Z., et al., *The Role of Dimensionality on the Optoelectronic Properties of Oxide and Halide Perovskites, and their Halide Derivatives.* Advanced Energy Materials, 2022. **12**(4): p. 2100499.
39. Zhou, H., Q. Chen, and Y. Yang, *Vapor-assisted solution process for perovskite materials and solar cells.* MRS Bulletin, 2015. **40**(8): p. 667-673.
40. Chen, Q., et al., *Planar Heterojunction Perovskite Solar Cells via Vapor-Assisted Solution Process.* Journal of the American Chemical Society, 2014. **136**(2): p. 622-625.
41. Tafazoli, S., et al., *The role of a vapor-assisted solution process on tailoring the chemical composition and morphology of mixed-halide perovskite solar cells.* CrystEngComm, 2018. **20**(31): p. 4428-4435.
42. Tonui, P., et al., *Perovskites photovoltaic solar cells: An overview of current status.* Renewable and Sustainable Energy Reviews, 2018. **91**: p. 1025-1044.
43. Jiang, Y., et al., *Post-annealing of MAPbI3 perovskite films with methylamine for efficient perovskite solar cells.* Materials Horizons, 2016. **3**(6): p. 548-555.
44. Zhou, Z., et al., *Methylamine-Gas-Induced Defect-Healing Behavior of CH3NH3PbI3 Thin Films for Perovskite Solar Cells.* Angewandte Chemie International Edition, 2015. **54**(33): p. 9705-9709.
45. Zhang, T., et al., *A controllable fabrication of grain boundary PbI2 nanoplates passivated lead halide perovskites for high performance solar cells.* Nano Energy, 2016. **26**: p. 50-56.
46. Hamukwaya, S.L., et al., *A Review of Recent Developments in Preparation Methods for Large-Area Perovskite Solar Cells.* Coatings, 2022. **12**(2): p. 252.
47. Chen, H., et al., *A scalable electrodeposition route to the low-cost, versatile and controllable fabrication of perovskite solar cells.* Nano Energy, 2015. **15**: p. 216-226.
48. Liu, M., M.B. Johnston, and H.J. Snaith, *Efficient planar heterojunction perovskite solar cells by vapour deposition.* Nature, 2013. **501**(7467): p. 395-398.
49. Li, H., et al., *Sequential vacuum-evaporated perovskite solar cells with more than 24% efficiency.* Science Advances, 2022. **8**(28): p. eabo7422.
50. Hao, F., et al., *Controllable Perovskite Crystallization at a Gas–Solid Interface for Hole Conductor-Free Solar Cells with Steady Power Conversion Efficiency over 10%.* Journal of the American Chemical Society, 2014. **136**(46): p. 16411-16419.
51. Chen, Z., et al., *Processing and Preparation Method for High-Quality Opto-Electronic Perovskite Film.* Frontiers in Materials, 2021. **8**.
52. Yang, Z., et al., *Flexible MAPbI3 perovskite solar cells with the high efficiency of 16.11% by low-temperature synthesis of compact anatase TiO2 film.* Journal of Alloys and Compounds, 2021. **854**: p. 155488.
53. Wang, Y., et al., *Compositional Engineering of Mixed-Cation Lead Mixed-Halide Perovskites for High-Performance Photodetectors.* ACS Applied Materials & Interfaces, 2019. **11**(31): p. 28005-28012.
54. Weller, M.T., et al., *Cubic Perovskite Structure of Black Formamidinium Lead Iodide, α-[HC(NH2)2]PbI3, at 298 K.* The Journal of Physical Chemistry Letters, 2015. **6**(16): p. 3209-3212.

55. Jeong, J., et al., *Pseudo-halide anion engineering for α-FAPbI(3) perovskite solar cells.* Nature, 2021. **592**(7854): p. 381-385.
56. Jeon, N.J., et al., *Compositional engineering of perovskite materials for high-performance solar cells.* Nature, 2015. **517**(7535): p. 476-480.
57. Yoo, J.J., et al., *Efficient perovskite solar cells via improved carrier management.* Nature, 2021. **590**(7847): p. 587-593.
58. Šimėnas, M., et al., *Phase Diagram and Cation Dynamics of Mixed MA1–xFAxPbBr3 Hybrid Perovskites.* Chemistry of Materials, 2021. **33**(15): p. 5926-5934.
59. Yoon, S.M., et al., *Surface Engineering of Ambient-Air-Processed Cesium Lead Triiodide Layers for Efficient Solar Cells.* Joule, 2021. **5**(1): p. 183-196.
60. Tan, S., et al., *Temperature-Reliable Low-Dimensional Perovskites Passivated Black-Phase CsPbI3 toward Stable and Efficient Photovoltaics.* Angewandte Chemie International Edition, 2022. **61**(23): p. e202201300.
61. Wang, -.H., et al., - *Compositional engineering for lead halide perovskite solar cells.* - Journal of Semiconductors, 2022. **- 43**(- 8): p. - 080202-1.
62. Eperon, G.E., et al., *Inorganic caesium lead iodide perovskite solar cells.* Journal of Materials Chemistry A, 2015. **3**(39): p. 19688-19695.
63. Yao, H., et al., *Research and progress of black metastable phase CsPbI3 solar cells.* Materials Chemistry Frontiers, 2021. **5**(3): p. 1221-1235.
64. Wang, K., et al., *All-inorganic cesium lead iodide perovskite solar cells with stabilized efficiency beyond 15%.* Nature Communications, 2018. **9**(1): p. 4544.
65. Wang, Y., et al., *Thermodynamically stabilized β-CsPbI₃–based perovskite solar cells with efficiencies >18%.* Science, 2019. **365**(6453): p. 591-595.
66. Luo, G., et al. *Current Transition of Nucleation and Growth under Diffusion-Controlled Electrocrystallization: A Brief Review*. Coatings, 2022. **12**, DOI: 10.3390/coatings12081195.
67. Yundan Yu, L.S., Hongliang Ge, Guoying Wei, Li Jiang, *Study on Electrochemistry and Nucleation Process of Nickel*

Electrodeposition. Int. J. Electrochem. Sci., 2017(12): p. 11.
68. Li, X., D. Pletcher, and F.C. Walsh, *Electrodeposited lead dioxide coatings.* Chemical Society Reviews, 2011. **40**(7): p. 3879-3894.
69. Hazza, A., D. Pletcher, and R. Wills, *A novel flow battery: A lead acid battery based on an electrolyte with soluble lead(ii) Part I. Preliminary studies.* Physical Chemistry Chemical Physics, 2004. **6**(8): p. 1773-1778.
70. Wang, J.-F., et al., *Surface engineering of perovskite films for efficient solar cells.* Scientific Reports, 2017. **7**(1): p. 14478.
71. Ge, Q.-Q., et al., *Promoting crystalline grain growth and healing pinholes by water vapor modulated post-annealing for enhancing the efficiency of planar perovskite solar cells.* Journal of Materials Chemistry A, 2016. **4**(35): p. 13458-13467.
72. Gedamu, D., et al., *Solvent-Antisolvent Ambient Processed Large Grain Size Perovskite Thin Films for High-Performance Solar Cells.* Sci Rep, 2018. **8**(1): p. 12885.

73. Bi, C., et al., *Non-wetting surface-driven high-aspect-ratio crystalline grain growth for efficient hybrid perovskite solar cells.* Nature Communications, 2015. **6**(1): p. 7747.
74. Samu, G.F., et al., *Electrochemistry and Spectroelectrochemistry of Lead Halide Perovskite Films: Materials Science Aspects and Boundary Conditions.* Chemistry of Materials, 2018. **30**(3): p. 561-569.
75. Di Girolamo, D. and D. Dini, *Electrodeposition as a Versatile Preparative Tool for Perovskite Photovoltaics: Aspects of Metallization and Selective Contacts/Active Layer Formation.* Solar RRL, 2022. **6**(6): p. 2100993.
76. Al-Katrib, M., et al., *Electrodeposition in Perovskite Solar Cells: A Critical Review, New Insights, and Promising Paths to Future Industrial Applications.* Advanced Materials Technologies. **n/a**(n/a): p. 2300964.
77. Popov, G., et al., *Scalable Route to the Fabrication of CH3NH3PbI3 Perovskite Thin Films by Electrodeposition and Vapor Conversion.* ACS Omega, 2016. **1**(6): p. 1296-1306.
78. Yadav, J., Q. Liang, and S. Pan, *Electrochemical Deposition of Organometallic Halide Perovskite Single-Crystal Particles with Density Gradients and Their Stability, Fluorescence, and Photoelectrochemical Properties.* The Journal of Physical Chemistry C, 2020. **124**(19): p. 10659-10668.
79. Zhitomirsky, I., et al., *Electrochemical preparation of PbO films.* Journal of Materials Science Letters, 1995. **14**(11): p. 807-810.
80. Gozalzadeh, S., F. Nasirpouri, and S.I. Seok, *Dimethylformamide-free synthesis and fabrication of lead halide perovskite solar cells from electrodeposited PbS precursor films.* Chemical Engineering Journal, 2021. **411**: p. 128460.
81. Li, W., et al., *Electrochemical deposition of PbI2 for perovskite solar cells.* Solar Energy, 2018. **159**: p. 300-305.
82. Wang, X., et al., *Electrochemical Deposition of CsPbBr3 Perovskite for Photovoltaic Devices with Robust Ambient Stability.* ACS Applied Materials & Interfaces, 2020. **12**(45): p. 50455-50463.
83. Liu, D., et al., *Improving PSCs' Short-circuit Current by Adding NaErF4:0.5%Tm@NaLuF4 Up-conversion Nanoparticles Insertion Layer.* Chemical Research in Chinese Universities, 2023. **39**(6): p. 1070-1076.
84. Heydari, Z., et al., *Effect of CH3NH3I/CH3NH3Br precursors on the structural and surface morphology properties of the electrodeposited methylammonium lead–mixed halide perovskite films.* Journal of Solid State Electrochemistry, 2021. **25**(2): p. 583-590.
85. Heydari, Z., et al., *A comparative study of mixed halide perovskite thin film preparation by three- and two-step electrodeposition techniques.* Optical Materials, 2022. **123**: p. 111909.
86. Li, Q., et al., *Electrodeposition of lead dioxide induces the fabrication of perovskite FAPbI3 film and electron-transport-layer-free solar cells.* Solar Energy, 2022. **233**: p. 515-522.
87. Pistor, P., et al., *Monitoring the Phase Formation of Coevaporated Lead Halide Perovskite Thin Films by in Situ X-ray Diffraction.* The Journal of Physical Chemistry Letters, 2014. **5**(19): p. 3308-3312.
88. Hidalgo, J., A.-F. Castro-Méndez, and J.-P. Correa-Baena, *Imaging and Mapping Characterization Tools for Perovskite Solar Cells.* Advanced Energy Materials, 2019. **9**(30): p. 1900444.

89. Huang, F., et al., *Gas-assisted preparation of lead iodide perovskite films consisting of a monolayer of single crystalline grains for high efficiency planar solar cells.* Nano Energy, 2014. **10**: p. 10-18.
90. Chen, L.-C., et al., *Effect of Different CH3NH3PbI3 Morphologies on Photovoltaic Properties of Perovskite Solar Cells.* Nanoscale Research Letters, 2018. **13**(1): p. 140.
91. You, P., et al., *2D materials for conducting holes from grain boundaries in perovskite solar cells.* Light: Science & Applications, 2021. **10**(1): p. 68.
92. Elgrishi, N., et al., *A Practical Beginner's Guide to Cyclic Voltammetry.* Journal of Chemical Education, 2018. **95**(2): p. 197-206.
93. Kyriacou, P., K. Budidha, and T.Y. Abay, *Optical Techniques for Blood and Tissue Oxygenation*, in *Encyclopedia of Biomedical Engineering*, R. Narayan, Editor. 2019, Elsevier: Oxford. p. 461-472.
94. Souissi, H., et al., *Exploring the structural and optical properties of lithium-chromium phosphate Li(3)Cr(2)(PO(3))(4).* Heliyon, 2024. **10**(16): p. e36188.
95. Chen, S., et al., *Characterization of Perovskite Obtained from Two-Step Deposition on Mesoporous Titania.* ACS Applied Materials & Interfaces, 2015. **7**(46): p. 25770-25776.
96. Ahmed, D.S., B.K. Mohammed, and M.K.A. Mohammed, *Long-term stable and hysteresis-free planar perovskite solar cells using green antisolvent strategy.* Journal of Materials Science, 2021. **56**(27): p. 15205-15214.
97. Kuan, C.-H., H.-H. Shen, and C.-F. Lin, *Low photoactive phase temperature all-inorganic, tin–lead mixed perovskite solar cell.* RSC Advances, 2021. **11**(6): p. 3264-3271.
98. Mitrić, J., *2 - Properties and characterization of rare-earth-activated phosphors*, in *Rare-Earth-Activated Phosphors*, V. Dubey, et al., Editors. 2022, Elsevier. p. 43-58.
99. Dar, M.I., et al., *Origin of unusual bandgap shift and dual emission in organic-inorganic lead halide perovskites.* Science Advances, 2016. **2**(10): p. e1601156.
100. Nguyen, H.T., et al. *Extracting optical bandgaps from luminescence images of perovskite solar cells*. in *2019 IEEE 46th Photovoltaic Specialists Conference (PVSC)*. 2019.
101. Tong, J., et al., *Wide-Bandgap Metal Halide Perovskites for Tandem Solar Cells.* ACS Energy Letters, 2021. **6**(1): p. 232-248.
102. Kanemitsu, Y. and Y. Yamada, *Band-Edge Luminescence from Oxide and Halide Perovskite Semiconductors.* Chemistry – An Asian Journal, 2020. **15**(6): p. 709-717.
103. Wehrenfennig, C., et al., *High Charge Carrier Mobilities and Lifetimes in Organolead Trihalide Perovskites.* Advanced Materials, 2014. **26**(10): p. 1584-1589.
104. Herz, L.M., *Charge-Carrier Mobilities in Metal Halide Perovskites: Fundamental Mechanisms and Limits.* ACS Energy Letters, 2017. **2**(7): p. 1539-1548.
105. Tamarat, P., et al., *Universal scaling laws for charge-carrier interactions with quantum confinement in lead-halide perovskites.* Nature Communications, 2023. **14**(1): p. 229.
106. Xu, W., et al., *Asymmetric charge carrier transfer and transport in planar lead halide perovskite solar cells.* Cell Reports Physical Science, 2022. **3**(5): p. 100890.
107. Mamun, A.A., et al., *A deconvoluted PL approach to probe the charge carrier dynamics of the grain interior and grain boundary of a perovskite film for perovskite solar cell applications.* Physical Chemistry Chemical Physics, 2017. **19**(13): p. 9143-9148.

108. Yang, Z., et al., *Enhancing electron diffusion length in narrow-bandgap perovskites for efficient monolithic perovskite tandem solar cells.* Nature Communications, 2019. **10**(1): p. 4498.
109. Stoddard, R.J., et al., *Correlation between Photoluminescence and Carrier Transport and a Simple In Situ Passivation Method for High-Bandgap Hybrid Perovskites.* The Journal of Physical Chemistry Letters, 2017. **8**(14): p. 3289-3298.
110. Motti, S.G., et al., *Phase segregation in mixed-halide perovskites affects charge-carrier dynamics while preserving mobility.* Nature Communications, 2021. **12**(1): p. 6955.
111. Zhang, H., et al., *Phase segregation due to ion migration in all-inorganic mixed-halide perovskite nanocrystals.* Nature Communications, 2019. **10**(1): p. 1088.
112. Erbe, A., et al., *How to Probe Structure, Kinetics, and Dynamics at Complex Interfaces In Situ and Operando by Optical Spectroscopy*, in *Encyclopedia of Interfacial Chemistry*, K. Wandelt, Editor. 2018, Elsevier: Oxford. p. 199-219.
113. Gfroerer, T.H., *Photoluminescence in Analysis of Surfaces and Interfaces*, in *Encyclopedia of Analytical Chemistry*.
114. Brennan, M.C., et al., *Light-Induced Anion Phase Segregation in Mixed Halide Perovskites.* ACS Energy Letters, 2018. **3**(1): p. 204-213.
115. Abdi-Jalebi, M., et al., *Chapter 3 - Optical absorption and photoluminescence spectroscopy*, in *Characterization Techniques for Perovskite Solar Cell Materials*, M. Pazoki, A. Hagfeldt, and T. Edvinsson, Editors. 2020, Elsevier. p. 49-79.
116. Slotcavage, D.J., H.I. Karunadasa, and M.D. McGehee, *Light-Induced Phase Segregation in Halide-Perovskite Absorbers.* ACS Energy Letters, 2016. **1**(6): p. 1199-1205.
117. Hoke, E.T., et al., *Reversible photo-induced trap formation in mixed-halide hybrid perovskites for photovoltaics.* Chemical Science, 2015. **6**(1): p. 613-617.
118. deQuilettes, D.W., et al., *Photo-induced halide redistribution in organic–inorganic perovskite films.* Nature Communications, 2016. **7**(1): p. 11683.
119. Andaji-Garmaroudi, Z., et al., *A Highly Emissive Surface Layer in Mixed-Halide Multication Perovskites.* Advanced Materials, 2019. **31**(42): p. 1902374.
120. Kim, H.-S., et al., *Lead Iodide Perovskite Sensitized All-Solid-State Submicron Thin Film Mesoscopic Solar Cell with Efficiency Exceeding 9%.* Scientific Reports, 2012. **2**(1): p. 591.
121. Lee, M.M., et al., *Efficient Hybrid Solar Cells Based on Meso-Superstructured Organometal Halide Perovskites.* Science, 2012. **338**(6107): p. 643-647.
122. Jeong, J., et al., *Pseudo-halide anion engineering for α-FAPbI3 perovskite solar cells.* Nature, 2021. **592**(7854): p. 381-385.
123. Jena, A.K., A. Kulkarni, and T. Miyasaka, *Halide Perovskite Photovoltaics: Background, Status, and Future Prospects.* Chemical Reviews, 2019. **119**(5): p. 3036-3103.
124. Bella, F., et al., *Caesium for Perovskite Solar Cells: An Overview.* Chemistry – A European Journal, 2018. **24**(47): p. 12183-12205.
125. Rong, Y., et al., *Toward Industrial-Scale Production of Perovskite Solar Cells: Screen Printing, Slot-Die Coating, and Emerging Techniques.* The Journal of Physical Chemistry Letters, 2018. **9**(10): p. 2707-2713.

126. Koza, J.A., et al., *Epitaxial Electrodeposition of Methylammonium Lead Iodide Perovskites.* Chemistry of Materials, 2016. **28**(1): p. 399-405.
127. Hill, J.C., J.A. Koza, and J.A. Switzer, *Electrodeposition of Epitaxial Lead Iodide and Conversion to Textured Methylammonium Lead Iodide Perovskite.* ACS Applied Materials & Interfaces, 2015. **7**(47): p. 26012-26016.
128. Kosta, I., H. Grande, and R. Tena-Zaera, *Dimethylformamide-free processing of halide perovskite solar cells from electrodeposited PbI2 precursor films.* Electrochimica Acta, 2017. **246**: p. 1193-1199.
129. Leal, W.D., et al., *Conversion of Electrochemically Deposited Aragonite Crystallites to Perovskite through Ion Exchange.* Crystal Growth & Design, 2022. **22**(4): p. 2364-2371.
130. Ding, C., et al., *Electrochemical synthesis of annealing-free and highly stable black-phase CsPbI3 perovskite.* Chemical Communications, 2021. **57**(71): p. 8981-8984.
131. Lv, P., et al., *The preparation of all-inorganic CsPbI2−xBr1+x perovskite solar cells based on electrodeposited PbO2 film.* Solar Energy, 2020. **207**: p. 618-625.
132. Hong, D., et al., *Inhibition of Phase Segregation in Cesium Lead Mixed-Halide Perovskites by B-Site Doping.* iScience, 2020. **23**(8): p. 101415.
133. Abdulkhadar, M. and M.A. Ittyachan, *Growth of Large Needles and Single Crystals of PbCl2 and PbBr2 in Silica Gel. An Improvement of the New Gel Technique.* Crystal Research and Technology, 1982. **17**(1): p. 33-38.
134. Straus, D.B., S. Guo, and R.J. Cava, *Kinetically Stable Single Crystals of Perovskite-Phase CsPbI3.* Journal of the American Chemical Society, 2019. **141**(29): p. 11435-11439.
135. Du, B., et al., *All-Inorganic Perovskite Nanocrystals-Based Light Emitting Diodes and Solar Cells.* ChemNanoMat, 2019. **5**(3): p. 266-277.
136. Chen, K., et al., *Short-Chain Ligand-Passivated Stable α-CsPbI3 Quantum Dot for All-Inorganic Perovskite Solar Cells.* Advanced Functional Materials, 2019. **29**(24): p. 1900991.
137. Kim, Y.G., et al., *Cesium lead iodide solar cells controlled by annealing temperature.* Physical Chemistry Chemical Physics, 2017. **19**(8): p. 6257-6263.
138. Ahmad, M., et al., *Structural, electronic and optical properties of CsPbX3 (X=Cl, Br, I) for energy storage and hybrid solar cell applications.* Journal of Alloys and Compounds, 2017. **705**: p. 828-839.
139. Liu, Z., et al., *Heavy metal ternary halides for room-temperature x-ray and gamma-ray detection*. SPIE Optical Engineering + Applications. Vol. 8852. 2013: SPIE.
140. Ravi, V.K., G.B. Markad, and A. Nag, *Band Edge Energies and Excitonic Transition Probabilities of Colloidal CsPbX3 (X = Cl, Br, I) Perovskite Nanocrystals.* ACS Energy Letters, 2016. **1**(4): p. 665-671.
141. Al Katrib, M., E. Planes, and L. Perrin, *Effect of Chlorine Addition on the Performance and Stability of Electrodeposited Mixed Perovskite Solar Cells.* Chemistry of Materials, 2022. **34**(5): p. 2218-2230.
142. Almosni, S., et al., *Material challenges for solar cells in the twenty-first century: directions in emerging technologies.* Science and Technology of Advanced Materials, 2018. **19**(1): p. 336-369.
143. Wilhelm, I., S. Teske, and G. Massonet. *Solar photovoltaic electricity empowering the world*. 2011.

144. Rong, Y., et al., *Challenges for commercializing perovskite solar cells.* Science, 2018. **361**(6408): p. eaat8235.
145. Snaith, H.J., *Present status and future prospects of perovskite photovoltaics.* Nature Materials, 2018. **17**(5): p. 372-376.
146. Arora, N., et al., *Perovskite solar cells with CuSCN hole extraction layers yield stabilized efficiencies greater than 20.* Science, 2017. **358**(6364): p. 768-771.
147. Yang, W.S., et al., *Iodide management in formamidinium-lead-halide-based perovskite layers for efficient solar cells.* Science, 2017. **356**(6345): p. 1376-1379.
148. Xiao, Z., et al., *Giant switchable photovoltaic effect in organometal trihalide perovskite devices.* Nature Materials, 2015. **14**(2): p. 193-198.
149. Stranks, S.D. and H.J. Snaith, *Metal-halide perovskites for photovoltaic and light-emitting devices.* Nature Nanotechnology, 2015. **10**(5): p. 391-402.
150. Yu, W., et al., *Single crystal hybrid perovskite field-effect transistors.* Nature Communications, 2018. **9**(1): p. 5354.
151. Shi, D., et al., *Low trap-state density and long carrier diffusion in organolead trihalide perovskite single crystals.* Science, 2015. **347**(6221): p. 519-522.
152. Zhang, L., et al., *CH3NH3PbX3 (X = I, Br) encapsulated in silicon carbide/carbon nanotube as advanced diodes.* Scientific Reports, 2018. **8**(1): p. 15187.
153. Cho, H., et al., *Overcoming the electroluminescence efficiency limitations of perovskite light-emitting diodes.* Science, 2015. **350**(6265): p. 1222-1225.
154. Qiu, L., L.K. Ono, and Y. Qi, *Advances and challenges to the commercialization of organic–inorganic halide perovskite solar cell technology.* Materials Today Energy, 2018. **7**: p. 169-189.
155. Salhi, B., et al., *Review of recent developments and persistent challenges in stability of perovskite solar cells.* Renewable and Sustainable Energy Reviews, 2018. **90**: p. 210-222.
156. Rong, Y., et al., *Beyond Efficiency: the Challenge of Stability in Mesoscopic Perovskite Solar Cells.* Advanced Energy Materials, 2015. **5**(20): p. 1501066.
157. Shi, Z. and A.H. Jayatissa, *Perovskites-Based Solar Cells: A Review of Recent Progress, Materials and Processing Methods.* Materials, 2018. **11**(5): p. 729.
158. Luo, J., et al., *Water photolysis at 12.3% efficiency via perovskite photovoltaics and Earth-abundant catalysts.* Science, 2014. **345**(6204): p. 1593-6.
159. Hamad, S., et al., *Electronic structure of porphyrin-based metal–organic frameworks and their suitability for solar fuel production photocatalysis.* Journal of Materials Chemistry A, 2015. **3**(46): p. 23458-23465.
160. Ye, M., et al., *Recent advances in interfacial engineering of perovskite solar cells.* Journal of Physics D: Applied Physics, 2017. **50**(37): p. 373002.
161. McMeekin, D.P., et al., *A mixed-cation lead mixed-halide perovskite absorber for tandem solar cells.* Science, 2016. **351**(6269): p. 151-155.
162. Søndergaard, R., et al., *Roll-to-roll fabrication of polymer solar cells.* Materials Today, 2012. **15**(1): p. 36-49.

163. Reinhard, P., et al. *Review of progress toward 20% efficiency flexible CIGS solar cells and manufacturing issues of solar modules*. in *2012 IEEE 38th Photovoltaic Specialists Conference (PVSC) PART 2*. 2012.
164. Kajal, P., K. Ghosh, and S. Powar, *Manufacturing Techniques of Perovskite Solar Cells*, in *Applications of Solar Energy*, H. Tyagi, et al., Editors. 2018, Springer Singapore: Singapore. p. 341-364.
165. Brenner, T.M., et al., *Conversion of Single Crystalline PbI2 to CH3NH3PbI3: Structural Relations and Transformation Dynamics.* Chemistry of Materials, 2016. **28**(18): p. 6501-6510.
166. Al-Katrib, M., et al., *Electrodeposition in Perovskite Solar Cells: A Critical Review, New Insights, and Promising Paths to Future Industrial Applications.* Advanced Materials Technologies, 2023. **8**(23): p. 2300964.
167. Jacquemin, J.L. and G. Bordure, *Electronic energy band calculation in β-PbO2 comparison with SnO2 and GeO2 energy band structures.* Solid State Communications, 1972. **11**(11): p. 1563-1567.
168. Cui, X.-P., et al., *Electrodeposition of PbO and its in situ conversion to CH3NH3PbI3 for mesoscopic perovskite solar cells.* Chemical Communications, 2015. **51**(8): p. 1457-1460.
169. Shamsi, J., et al., *N-Methylformamide as a Source of Methylammonium Ions in the Synthesis of Lead Halide Perovskite Nanocrystals and Bulk Crystals.* ACS Energy Letters, 2016. **1**(5): p. 1042-1048.
170. Liu, S., et al., *Oxidation of iodide by PbO2, the major lead pipe corrosion product: Kinetics, mechanism and formation of toxic iodinated disinfection by-products.* Chemical Engineering Journal, 2023. **451**: p. 139033.
171. Jong, U.-G., et al., *Influence of water intercalation and hydration on chemical decomposition and ion transport in methylammonium lead halide perovskites.* Journal of Materials Chemistry A, 2018. **6**(3): p. 1067-1074.
172. Muscarella, L.A., et al., *Crystal Orientation and Grain Size: Do They Determine Optoelectronic Properties of MAPbI3 Perovskite?* The Journal of Physical Chemistry Letters, 2019. **10**(20): p. 6010-6018.
173. Peng, H., et al., *High-Quality Perovskite CH3NH3PbI3 Thin Films for Solar Cells Prepared by Single-Source Thermal Evaporation Combined with Solvent Treatment.* Materials, 2019. **12**(8): p. 1237.
174. Chu, Z., et al., *Impact of grain boundaries on efficiency and stability of organic-inorganic trihalide perovskites.* Nature Communications, 2017. **8**(1): p. 2230.
175. Cao, J., et al., *Porous PbI2 films for the fabrication of efficient, stable perovskite solar cells via sequential deposition.* Journal of Materials Chemistry A, 2016. **4**(26): p. 10223-10230.
176. Jiang, J., et al., *ITIC surface modification to achieve synergistic electron transport layer enhancement for planar-type perovskite solar cells with efficiency exceeding 20%.* Journal of Materials Chemistry A, 2017. **5**(20): p. 9514-9522.
177. Jin, Z., et al., *Solution-processed transparent coordination polymer electrode for photovoltaic solar cells.* Nano Energy, 2017. **40**: p. 376-381.
178. Wang, Q., et al., *Energy-Down-Shift CsPbCl3:Mn Quantum Dots for Boosting the Efficiency and Stability of Perovskite Solar Cells.* ACS Energy Letters, 2017. **2**(7): p. 1479-1486.

179. Wang, H., et al., *Cesium Lead Mixed-Halide Perovskites for Low-Energy Loss Solar Cells with Efficiency Beyond 17%.* Chemistry of Materials, 2019. **31**(16): p. 6231-6238.
180. Zeng, Q., et al., *Polymer-Passivated Inorganic Cesium Lead Mixed-Halide Perovskites for Stable and Efficient Solar Cells with High Open-Circuit Voltage over 1.3 V.* Advanced Materials, 2018. **30**(9): p. 1705393.
181. Akkerman, Q.A., et al., *Strongly emissive perovskite nanocrystal inks for high-voltage solar cells.* Nature Energy, 2016. **2**(2): p. 16194.
182. Li, W., et al., *Phase Segregation Enhanced Ion Movement in Efficient Inorganic CsPbIBr2 Solar Cells.* Advanced Energy Materials, 2017. **7**(20): p. 1700946.
183. Lau, C.F.J., et al., *Strontium-Doped Low-Temperature-Processed CsPbI2Br Perovskite Solar Cells.* ACS Energy Letters, 2017. **2**(10): p. 2319-2325.
184. Chen, C.-Y., et al., *All-Vacuum-Deposited Stoichiometrically Balanced Inorganic Cesium Lead Halide Perovskite Solar Cells with Stabilized Efficiency Exceeding 11%.* Advanced Materials, 2017. **29**(12): p. 1605290.
185. Frolova, L.A., et al., *Highly Efficient All-Inorganic Planar Heterojunction Perovskite Solar Cells Produced by Thermal Coevaporation of CsI and PbI2.* The Journal of Physical Chemistry Letters, 2017. **8**(1): p. 67-72.
186. Liu, T., S. Salek, and J.C. Byers, *Chemical conversion of electrodeposited PbO2 to the all-inorganic cesium lead halide perovskites CsPbBr3 and CsPbCl3.* Electrochemistry Communications, 2022. **143**: p. 107381.
187. Eze, V.O., et al., *Inorganic cesium lead mixed halide based perovskite solar materials modified with functional silver iodide.* Scientific Reports, 2022. **12**(1): p. 7794.
188. Duan, C., et al., *Highly electroluminescent and stable inorganic CsPbI2Br perovskite solar cell enabled by balanced charge transfer.* Chemical Engineering Journal, 2021. **417**: p. 128053.
189. Gaonkar, H., et al. *Inorganic cesium-lead mixed halide perovskite p-i-n solar cells deposited using layer-by-layer vacuum deposition technique*. in *2019 IEEE 46th Photovoltaic Specialists Conference (PVSC)*. 2019.
190. Tai, M., et al., *Efficient Inorganic Cesium Lead Mixed-Halide Perovskite Solar Cells Prepared by Flash-Evaporation Printing.* Energy Technology, 2019. **7**(8): p. 1800986.
191. Knight, A.J., et al., *Halide Segregation in Mixed-Halide Perovskites: Influence of A-Site Cations.* ACS Energy Letters, 2021. **6**(2): p. 799-808.
192. Liu, L., et al., *A-site phase segregation in mixed cation perovskite.* Materials Reports: Energy, 2021. **1**(4): p. 100064.
193. Ngqoloda, S., et al., *Mixed-halide perovskites solar cells through PbICl and PbCl2 precursor films by sequential chemical vapor deposition.* Solar Energy, 2021. **215**: p. 179-188.
194. Howlader, A.H. and A. Uddin, *Progress and Challenges of Chloride–Iodide Perovskite Solar Cells: A Critical Review.* Nanomanufacturing, 2023. **3**(2): p. 177-216.
195. Basumatary, P., J. Kumari, and P. Agarwal, *Probing the defects states in MAPbI3 perovskite thin films through photoluminescence and photoluminescence excitation spectroscopy studies.* Optik, 2022. **266**: p. 169586.

196. Frohna, K., et al., *Nanoscale chemical heterogeneity dominates the optoelectronic response of alloyed perovskite solar cells.* Nature Nanotechnology, 2022. **17**(2): p. 190-196.
197. Adhyaksa, G.W.P., et al., *Understanding Detrimental and Beneficial Grain Boundary Effects in Halide Perovskites.* Advanced Materials, 2018. **30**(52): p. 1804792.
198. Gualdrón-Reyes, A.F., S.J. Yoon, and I. Mora-Seró, *Recent insights for achieving mixed halide perovskites without halide segregation.* Current Opinion in Electrochemistry, 2018. **11**: p. 84-90.
199. Gualdrón-Reyes, A.F., et al., *Controlling the Phase Segregation in Mixed Halide Perovskites through Nanocrystal Size.* ACS Energy Letters, 2019. **4**(1): p. 54-62.